Design, optimization and fabrication of bio-inspired sutures

By

Idris Adaviriku Malik

Department of Mechanical Engineering
McGill University

Montreal, Quebec, Canada

February 2018

A thesis submitted to McGill University in partial fulfillment of the requirements for a doctoral degree

Dedication

To God Almighty, to my parents and my family

Table of Contents

Contents

List of Figures

Abstract

Nature displays many examples of materials with exceptional mechanical properties. In particular, hard biological materials such as mollusk shells, bone, and tooth enamel boast remarkable combinations of stiffness, hardness and fracture toughness that stem from complex structures of organic (biological polymers) and inorganic (minerals). As a "universal rule" in these hard materials, minerals provide stiffness and hardness, while the organic polymer rich interfaces generate nonlinear deformations and channel cracks into powerful toughening configurations. This concept can also be extended to geometrically sutured interfaces, which are common in human skulls, cephalopods or turtle shell. These sutures can arrest cracks, absorb impact energy, and provide flexibility for respiration, locomotion or growth. This thesis explores the mechanical design, optimization, fabrication and testing of two dimensional sutures with complex interlocking geometries. The emphasis is on pullout response and the effect of interlocking, which was modelled based on non-Hertzian contact solutions and kinematics. Finite element models of these sutures were also developed, which produced results in close agreement with the analytical solutions. The accuracy of these models was verified using 3D printing and mechanical testing of jigsaw interlocking sutures. The models capture the effect of tuning geometrical and interfacial properties of suture interfaces to alter the mechanical response of the material. A limiting factor in the strength of the interlocking is the fracture of the solid parts of the suture, which must be avoided. The models show that the most severe stresses in the suture arise from frictional contact stresses. Therefore, the optimum design was achieved by using low friction coefficient and relatively high locking angle. The general problem of the design and optimization of complex interlocking sutures is also considered by capturing the geometry of sutured interfaces with "line descriptors", in which thousands of sutures with different geometric properties were systematically generated and explored using analytical and finite element solutions. The

results show that for all families of suture, optimum designs are achieved with low friction coefficient and relatively high locking angle, and also that sutures with multiple locking sites distributed along the pulling direction provide the best combination of material properties overall. Finally, a laser engraving method is proposed to create trenches with controlled suture patterns and depth in thin plates of aluminium oxide. These trenches guided cracks into these interfaces to implement toughening mechanisms and unusual deformation. Different kinds of interfaces were engraved: straight, transverse, sinusoidal, and jigsaw interlocking (characterized by interlocking angle) interfaces. The results show how the shape of suture interfaces can be used to tune the mechanical behavior of the material, and also show that the jigsaw interlocking interface dissipated the most energy and produced the highest toughness. The combination of models and experiments presented in this thesis provide a new framework for the geometrical design and optimization of sutured lines, for applications where the propagation of cracks and/or local compliance must be controlled.

Résumé

La nature présente de nombreux exemples de matériaux ayant d'exceptionnelles propriétés mécaniques. Plus particulièrement, les matériaux biologiques durs tels que les coquilles de mollusque, les os et l'émail dentaire qui sont composés de structures complexes de polymères organiques (biologiques) et inorganiques (minéraux), qui génèrent des combinaisons remarquables de rigidité, de dureté et de ténacité. La «règle universelle» pour ces matériaux durs est que les polymères doux représentent des interfaces faibles qui engendrent des déformations non linéaires et canalisent les fissures en de puissantes configurations de durcissement complexes. Ce concept puissant peut également être étendu aux interfaces suturées géométriquement que l'on retrouve dans le crâne humain, les céphalopodes ou la coquille de tortue. Ces sutures peuvent arrêter les fissures et fournir une flexibilité pour la respiration, la locomotion ou la croissance. La géométrie et la complexité des sutures varient selon les matériaux. Cependant dans une famille de matériaux, les sutures varient d'une espèce à l'autre et évoluent. Cette thèse explore la conception, la mécanique, l'optimisation et la fabrication de sutures bidimensionnelles complexes. La modélisation de la conduite des sutures de verrouillage entrecroisées lors de l'extraction est basée sur des modèles de contact non-hertziens ainsi que la cinématique. Des modèles d'éléments finis de ces sutures ont également été développés, ce qui a produits des résultats en concordances avec les solutions analytiques. L'exactitude de ces modèles a été vérifiée en utilisant l'impression 3D et des essais mécaniques de sutures de verrouillage entrecroisées. Les modèles reflètent l'effet de réglage des propriétés géométriques et interfaciales des interfaces de suture afin d'altérer la réponse mécanique du matériau. Les modèles utilisés et les expériences effectuées, démontrent que la conception optimale est obtenue en utilisant un faible coefficient de frottement et un angle d'entrecroisement relativement élevé. La problématique de la conception et de l'optimisation est donc considérée en décrivant la géométrie des interfaces

suturées avec des «descripteurs de ligne», dans lesquels des milliers de sutures aux propriétés géométriques distinctes ont systématiquement été générées et explorées. Les résultats montrent que pour toutes les familles de sutures, le résultat optimal est atteint avec un faible coefficient de frottement et un angle de verrouillage relativement élevé. De plus, la suture avec verrouillage multiple le long du sens de traction a la meilleure combinaison de propriétés du matériau. Enfin, une méthode de gravure au laser est proposée pour créer des tranchées avec des motifs de sutures contrôlées et une profondeur dans des plaques minces d'oxyde d'aluminium. Ces tranchées ont guidé les fissures dans ces interfaces pour mettre en œuvre des mécanismes de durcissements et des déformations inhabituelles. Différents types d'interfaces ont été gravés: les interfaces droites, transversales, sinusoïdales et entrecroisées (caractérisées par un angle d'interverrouillage). Les résultats illustrent comment la forme des interfaces de suture peut être utilisée pour affiner le comportement mécanique du matériau; ils démontrent également que l'interface de verrouillage entrecroisé dissipe le plus d'énergie et produit la plus grande ténacité. La combinaison des modèles et des expériences présentés dans cette thèse fournit un nouveau cadre pour la conception géométrique et l'optimisation de lignes suturées, dans des instances où la propagation des fissures et / ou la conformité locale doit être contrôlée.

Acknowledgement

The completion of this thesis is with the help, support, and encouragement from a group of people in McGill University, my family and my friends.

I would like specially appreciate my thesis supervisor Professor Francois Barthelat for his tremendous support, guidance, novel ideas and supervision throughout the course of this study.

He is and will always remain a great mentor and motivation for me his passion for science and engineering will be a great source of inspiration in my future professional career.

Special thanks to the Faculty of Engineering at McGill University, the Natural Sciences and Engineering Research Council of Canada, and National University commission for their collaborative financial support for this project.

I would like to express my greatest appreciation to the former and current members of the Advanced materials and bioinspiration Lab at McGill: Dr Mohammad Mirkhalaf, Dr Ahmad Khayer Dastjerdi, Dr Roberto Martini, Sacha Cavelier, Ahmed Dalaq, Najmul Abid, Zhen Yin, Ali Shafiel, Ludovic Prunier. They were my true friends and a source of inspiration during the past several years. I also would like to thank my other colleagues and friends: Afuwape Gbolahan, Toluwanimi Fagorusi, and Ademola Adekunle for their help and support.

Last but not least, I would like to say my deepest thanks to my loving parents, my sisters, and my brothers for their love, support and encouragement throughout my ongoing journey in education.

Contributions of the Author

This is a manuscript-based thesis consisting of three journal articles and an extra introductory chapter. The title of the articles, name of the authors, and their contributions are listed below:

1) Bio-inspired "Jigsaw"-like interlocking sutures: Modeling, optimization, 3D printing and testing

Idris Adaviriku Malik, Mohammad Mirkhalaf, and Francois Barthelat

Department of Mechanical Engineering, McGill University, 817 Sherbrooke Street West, Montreal, Quebec, Canada H3A 2K6

Journal of mechanics and physics of solids, Volume 102, May 2017, Pages 224-238

https://doi.org/10.1016/j.jmps.2017.03.003

***Author contributions**:*

IAM: Developed the analytical and finite element model, performed the data analysis, prepared figures, helped in the experiments, prepared manuscript

MM: Helped in troubleshooting the finite element model, helped in the experiments, helped preparing the manuscript.

FB: Supervised the research and review processes, gave technical and scientific advice, helped to develop the analytical model, and edited the figures and the text.

2) Bioinspired sutured materials for strength and toughness: Pullout mechanisms and geometric enrichments

Idris Adaviriku Malik, Francois Barthelat

Department of Mechanical Engineering, McGill University, 817 Sherbrooke Street West, Montreal, QC H3A 2K6, Canada

Submitted for publication to the International Journal of solids and structures, 2017.

***Author contributions**:*

IAM: Developed the finite element and analytical models, analysed data, prepared the figures, analysed the results, and wrote the manuscripts

FB: Supervised the research, edited the figures and manuscript.

3) Toughening of thin ceramic plates using bioinspired surface patterns

Idris Adaviriku Malik and Francois Barthelat

Department of Mechanical Engineering, McGill University, 817 Sherbrooke Street West, Montreal, Quebec, Canada H3A 2K6

International Journal of solids and structures, Volumes 97–98, 15 October 2016, Pages 389–399

http://dx.doi.org/10.1016/j.ijsolstr.2016.07.010

***Author contributions**:*

IAM: Designed the weak interfaces, fabricated the samples, performed the tests and data analyses, overviewed the optimization processes, discussed the results and prepared the manuscript.

FB: Supervised the research, helped analyse the results, and edited the figures and manuscript.

A complete list of publications including peer-reviewed journal articles, conference presentation is presented in Chapter 6 of this thesis.

Chapter 1
Introduction

Chapter 1: Introduction

Modern engineering systems and structures require materials with ever increasing sets of structural performance requirements. Some mechanical properties however remain mutually exclusive, for example, materials that are hard are usually brittle and materials that are tougher are in general softer [1]. This general trends applies for example to steel, which can be made harder by manipulating composition, microstructure or residual stresses, but at the expense of ductility and toughness [2]. A powerful approach for overcoming this limitation is to combine two or more materials with complementary properties into 'hybrid' materials. Hybrid materials offer combinations of performance and functionality not possible to achieve in monolithic materials [3]. In hybrid materials, properties can be manipulated by tuning individual constituents, volumetric content, morphology, size and arrangement [1, 4]. Crack deflection along weak interfaces is key to the high fracture toughness of hybrid materials, as seen for example in layered ceramics [5]. Interestingly, while hybrid materials have only recently emerged in the engineering world, nature has been using this type of materials for millions of years. Natural materials such as bone, teeth or mollusc shells have remarkable combinations of mechanical properties including low weight, high stiffness, high strength and toughness. Researchers have now started to explain the microstructures and mechanisms that enhance these mechanical performances with the help of sophisticated experimental, computational and theoretical tools [4, 6]. Therefore, these biological materials can provide models and inspirations on how hard materials (inorganic minerals and ceramics) and soft materials (organic proteins and polymers) can be combined to make materials with outstanding structural performance. Nacre from mollusc shell for example, is composed of about 95% vol. of brittle aragonite (one of the crystalline forms of calcium carbonate), and of about 5% organic material including a compound of proteins and polysaccharides [7], forming a staggered arrangement of these mineral tablets which are separated by thin a layer

interface of organic materials. The tablets overlap each other in irregular stacked columns which can be described as stacks of coins randomly overlapping each other. Toughening mechanisms in nacre are due to one or combinations of two or more processes which includes creation of new surfaces due to delamination, energy dissipation at the interfaces which is a result of continuous tablet sliding, crack bridging and deflection, and plastic region [8-11]. The waviness of the tablets also leads to a locking mechanism which generates strain hardening and helps to distribute inelastic deformation, thus stabilizing the material up to relatively large strains [9]. Similar mechanisms can be found in other structural biological materials, such as bones and tooth enamel. In all of these natural materials, weak interfaces play a critical role in deflecting cracks, and in channelling deformation. Interfaces are also found as sutures in natural materials, which can take several shapes like sinusoidal [12], more complex geometries as in an adult skull [13, 14], or even hierarchical fractal-like structures as in ammonites [15, 16]. Experiments [17] and computational models [18] have been recently developed to evaluate the influence of hierarchical suture interface patterns on the mechanical behaviour of these sutures.

The main objective of studying the structure and mechanical behaviour of these biological materials is bioinspiration, that is the duplication of these structures and mechanisms in engineering materials. Fabrication of these complex materials remains a challenge to this day. A variety of techniques have been used to fabricate bio-inspired materials including sputtering [19], freeze casting [20], layer by layer deposition [21], self-assembly [22], rapid prototyping [2], laser engraving [23, 24]. In spite of all these techniques, no synthetically produced material could so far duplicate the toughness of nacre (with the same organic layer contents) as compared to its mineral constituent. The well-controlled packing of tablets at small length scales has not been achieved and the continuous tablet sliding in natural nacre could only be duplicated in a few materials at larger scales [2, 25, 26].

1.1. Thesis objectives

The overall aim of this thesis was to design, optimize and fabricate sutured materials inspired from nature. The specific objectives of this thesis were to:

i. Capture the shape of complex 2D sutures using a shape descriptor approach.

ii. Model the pullout response of these sutures using analytical solutions based on simple kinematics and contact mechanics

iii. Model the pullout response of these sutures using finite elements

iv. Use the modelling tool to explore the mechanical performance of simple jigsaw geometries, dovetail geometries, double and multiple locking site geometries.

v. Build performance maps showing strength and energy absorption to compare and select optimum suture geometries.

vi. Fabricate sutured materials from brittle materials like ceramics and Acrylonitrile butadiene styrene (ABS) using Laser engraving and 3D printing, and mechanically test these materials for validation.

1.2. Thesis organization

This is a manuscript based thesis with six chapters. In the current chapter, a brief introduction of biological materials, bioinspiration and thesis motivation and objectives was presented. Chapter 2 presents a general overview and literature reviews on natural materials, focusing on sutures and interface-driven materials such as nacre, cranial sutures, and woodpeckers' beak. Fabrication methods for bioinspired materials are also reviewed and discussed in that chapter.

Chapter 3 presents a jigsaw-like 2D suture, together with analytical and finite element models to predict pullout strength and energy absorption. An exhaustive search optimization method was then used to optimize the mechanical properties with combinations of design variables

(interlocking angle and friction coefficient). These models were validated experimentally using 3D printing and mechanical testing of Acrylonitrile butadiene styrene (ABS). In chapter 4, we extended these studies by systematically generating sutures with a larger number of geometrical parameters, using shape descriptors. Analytical and finite element models were developed to explore the effect of geometrical parameters on the pullout response and maximum stress in a suture, and optimization revealed that the best suture for each of the suture families is with lower friction coefficient and higher interlocking angle, and generally multilocking showed the best suture perfomance. In Chapter 5, the laser engraving method is used to fabricate sutures of intricate shapes in thin ceramic plates. In that chapter, we were able to show that the mechanical properties of sutures can be tuned by changing the geometry of the suture interfaces. These findings propel us to develop analytical and finite element models to further examine the effect of geometrical parameters on jigsaw-like interlocking sutures. Finally, chapter 6 discussed the summary of the accomplishments and the main contribution of this research project. Some recommendations for future work and applications are also presented.

1.3. References

1. Ritchie, R.O., *The conflicts between strength and toughness.* Nat Mater, 2011. **10**(11): p. 817-822.
2. Espinosa, H.D., et al., *Merger of structure and material in nacre and bone – Perspectives on de novo biomimetic materials.* Progress in Materials Science, 2009. **54**(8): p. 1059-1100.
3. Ashby, M.F. and Y.J.M. Bréchet, *Designing hybrid materials.* Acta Materialia, 2003. **51**(19): p. 5801-5821.

4. Ashby, M.F., et al., *The Mechanical Properties of Natural Materials. I. Material Property Charts.* Proceedings: Mathematical and Physical Sciences, 1995. **450**(1938): p. 123-140.

5. Clegg, W.J., et al., *A simple way to make tough ceramics.* Nature, 1990. **347**(6292): p. 455-457.

6. Levi, C., et al., *A remarkably strong natural glassy rod: the anchoring spicule of theMonorhaphis sponge.* Journal of Materials Science Letters, 1989. **8**(3): p. 337-339.

7. Currey, J.D., *Mechanical Properties of Mother of Pearl in Tension.* Proceedings of the Royal Society of London. Series B. Biological Sciences, 1977. **196**(1125): p. 443-463.

8. Katti, K.S. and D.R. Katti, *Why is nacre so tough and strong?* Materials Science and Engineering C, 2006. **26**(8): p. 1317-1324.

9. Barthelat, F., et al., *On the mechanics of mother-of-pearl: A key feature in the material hierarchical structure.* Journal of the Mechanics and Physics of Solids, 2007. **55**(2): p. 306-337.

10. Rabiei, R., S. Bekah, and F. Barthelat, *Failure mode transition in nacre and bone-like materials.* Acta Biomaterialia, 2010. **6**(10): p. 4081-4089.

11. Mayer, G., *Rigid biological systems as models for synthetic composites.* Science, 2005. **310**(5751): p. 1144-7.

12. Li, Y., C. Ortiz, and M.C. Boyce, *Stiffness and strength of suture joints in nature.* Physical Review E, 2011. **84**(6): p. 062904.

13. Maloul, A., et al., *Characterization of craniofacial sutures using the finite element method.* Journal of Biomechanics. **47**(1): p. 245-252.

14. Miura, T., et al., *Mechanism of skull suture maintenance and interdigitation.* Journal of Anatomy, 2009. **215**(6): p. 642-655.

15. Allen, E.G., *Understanding ammonoid sutures: New insight into the dynamic evolution of Paleozoic suture morphology*. Cephalopods Present and Past: New Insights and Fresh Perspectives, ed. N.H. Landman, R.A. Davis, and R.H. Mapes. 2007. 159-180.

16. Klug, C. and R. Hoffmann, *Ammonoid Septa and Sutures*, in *Ammonoid Paleobiology: From anatomy to ecology*, C. Klug, et al., Editors. 2015, Springer Netherlands: Dordrecht. p. 45-90.

17. Lin, E., et al., *Tunability and enhancement of mechanical behavior with additively manufactured bio-inspired hierarchical suture interfaces.* Journal of Materials Research, 2014. **29**(17): p. 1867-1875.

18. Li, Y., C. Ortiz, and M.C. Boyce, *Bioinspired, mechanical, deterministic fractal model for hierarchical suture joints.* Physical Review E, 2012. **85**(3): p. 031901.

19. He, J.L., W.Z. Li, and H.D. Li, *Simulation of nacre with TiN/Pt multilayers and a study of their hardness.* Journal of Materials Research, 1997. **12**(11): p. 3140-3145.

20. Deville, S., et al., *Freezing as a path to build complex composites.* Science, 2006. **311**(5760): p. 515-8.

21. Podsiadlo, P., et al., *Ultrastrong and Stiff Layered Polymer Nanocomposites.* Science, 2007. **318**(5847): p. 80-83.

22. Sellinger, A., et al., *Continuous self-assembly of organic-inorganic nanocomposite coatings that mimic nacre.* Nature, 1998. **394**(6690): p. 256-260.

23. Mirkhalaf, M., A.K. Dastjerdi, and F. Barthelat, *Overcoming the brittleness of glass through bio-inspiration and micro-architecture.* Nature communications, 2014. **5**: p. 3166.

24. Mirkhalaf, M., J. Tanguay, and F. Barthelat, *Carving 3D architectures within glass: Exploring new strategies to transform the mechanics and performance of materials.* Extreme Mechanics Letters, 2016. **7**: p. 104-113.

25. Barthelat, F. and D. Zhu, *A novel biomimetic material duplicating the structure and mechanics of natural nacre.* Journal of Materials Research, 2011. **26**(10): p. 1203-1215.

26. Mayer, G., *New classes of tough composite materials-Lessons from natural rigid biological systems.* Materials Science and Engineering C, 2006. **26**(8): p. 1261-1268.

Chapter 2
Bioinspiration and Biomimetics

Chapter 2: Bioinspiration and biomimetics

2.1 Background and motivation

Biological materials possess remarkable combinations of mechanical properties including low weight, high stiffness, high strength and toughness. Recent research efforts have combined experimental, computational and theoretical tools to explain how the architecture of these materials and their associated mechanisms generate high mechanical performance. These findings serve as the basis for biomimetics and bioinspiration in material science, and to new engineering materials with high performance and new functionalities [1-4]. A common trait to all biological materials is the hierarchical structure that governs their mechanical properties, as seen in siliceous sponges and diatom cells which display simultaneous flexibility, toughness and mechanical protection [5, 6]. In engineering materials, these mechanical properties can be achieved by combining two or more materials with properties that complement each other to produce "hybrid materials". Hybrid materials often surpass monolithic materials in terms of performance and functionalities [7]. Interestingly the properties of hybrid materials can be manipulated in many ways, by tuning individual constituents, volumetric content, morphology, size and arrangement [8, 9]. For example, the presence of weak interfaces, which aid crack deflection is key to the improved fracture resistance to engineering ceramics, provided that the interfaces are weak enough to deflect cracks [10]. The properties of these interfaces can be finely tuned with the addition of fibers or whiskers [11]. Figure 2.1 shows the mechanical performance of synthetic and natural materials in terms of stiffness (Young's modulus) and toughness [12]. The toughness and the elastic modulus of synthetic materials such as metal alloys and ceramics are shown in Figure 2.1a, while Figure 2.1b shows the mechanical performance map for natural ceramics, biopolymer, and their composites [13]. The lower right corner of the map shows stiff but brittle materials, example includes calcite, while the upper left corner of the map shows soft

proteinaceous materials such as skin that possesses mechanical behaviour similar to elastomers. The upper right corner of the map shows how these materials achieve high stiffness by incorporating minerals while retaining exceptional toughness. Nature may therefore suggest pathways to resolving conflicts between toughness, stiffness and strength [9]. The yellow oval shape shows that the properties of these synthetic materials can be tuned through bioinspiration, which is the main objective of this research.

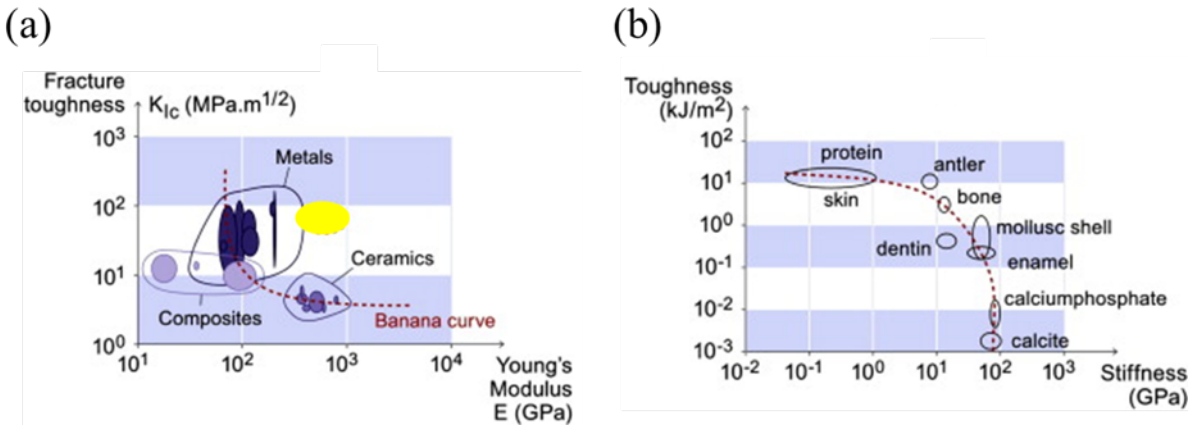

Figure 2.1: The mechanical performance of engineered and biological materials in the stiffness–toughness domain. Figure 2.1a compares the toughness and stiffness properties for a number of biological materials [12]; Figure 2.1b shows toughness and stiffness for synthetic materials, such as metals, alloys and ceramics (yellow portion showing what researchers want to achieve with bioinspired materials) [14].

The remarkable mechanical performance of hard biological materials such as nacre, tooth enamel or bone has generated a significant interest in the past 30 years [15-17]. These materials are mostly made of brittle components, for example hydroxyapatite in bone and teeth, calcium carbonate in seashells and corals, amorphous silica in sponge spicules and diatoms [2]. Despite these brittle ingredients these materials exhibit outstanding strength, modulus, and toughness originating from the way the ingredients are combined into intricate architectures [15, 17]. The hard biological materials are basically products of biomineralization of composites of inorganic oxide phase with addition of biopolymer. Bones and teeth have fibrous architectures which are anisotropic in nature and which contribute to

the mechanical performance of the material [18], while nacre (a more simple structure) has also attracted great attention for biomimetic purposes because of its high mechanical performance [19-21]. Barthelat and Mirkhalaf, [22] examined the general problem of how to combine a soft, energy dissipating material with stiff and strong, but brittle material. A "Universal" solution in nature combines a soft phase to provide energy dissipation, toughness, ductility, and a hard phase to provide stiffness.

2.2 Examples of hard biological Materials

The stiffest biological materials serve as skeleton or protective systems. These materials contain high volume fraction of minerals (>90%), in order to achieve the stiffness and hardness required for these functions. Examples of these materials are mollusc shells, bones, and tooth enamel, which are briefly described below.

2.2.1 Mollusc shells

Mollusc represent a large phylum of invertebrate animals known as the Mollusca, with over 60,000 known species up to date [23]. The vast majority of mollusc grow on or several hard ceramic shells for protection against natural and human factors. Mollusc shells exist in a variety of sizes ranging from micromolluscs approximately 1 mm and 25cm in abalone shells. The shell is grown by a mantle, a soft tissue that covers the inside of the shell, which gives rise to different varieties of shell structures [2]. Mollusc shells are made of either calcite or aragonite, with small amount of organic material which never exceeds 5% of the composition in weight [20, 27, 31]. Nacre is among the strongest and toughest materials found in mollusc shells.

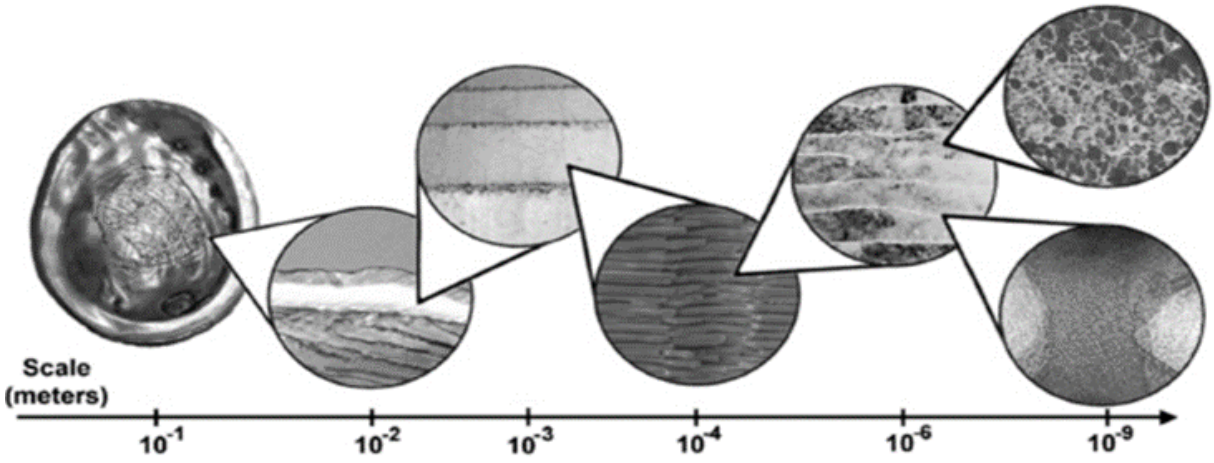

Figure 2.2: The hierarchical structure of red abalone nacre. Adapted from [24, 25]

Nacre is composed of about 95% vol. of brittle aragonite (one of the crystalline forms of calcium carbonate), and of about 5% organic material including a compound of proteins and polysaccharides [26]. Nacre exhibits a lamellar structure resembling a brick-wall where 0.2–0.9 mm thick aragonite tablets are cemented together with thin 30 nm organic layers serving as glue and maintaining the integrity of the whole structure. The tablets overlap each other in an irregularly stacked columns which are described as stack of coins randomly overlapping each other. Mineral tablets in nacre are arranged in a staggered manner which provides the structure with a unique mechanism of deformation and outstanding combinations of stiffness, strength and toughness [16, 27]. Experimental analysis and computational modelling has been used to describe the microstructural features that dictates this excellent performance. Results from these studies show that tablet sliding and progressive pullout is a key deformation mechanism [27]. Cracks propagating across the nacreous layers activate an array of powerful mechanisms such as crack deflection, ligament bridging and effect of process zone [28]. The interfaces in nacre are actually relatively weak as measured by Rabiei et al [29] using interlaminar chevron notch fracture tests on nacre from red abalone, pearl oyster and top shell. The extrinsic toughening mechanisms contribute up to 97% of the toughness while the intrinsic toughness of the organic glue accounts for only 3% of the

overall toughness of nacre [28, 30]. The structure and mechanism of nacre are now the basis of inspiration in the design of next generation synthetic composites material, because it stands out as perfect example of a natural material that developed highly sophisticated microstructure for optimal performance [16, 28, 31, 32].

2.2.2 Bone and teeth

Other examples of hard structural biological materials are bones and tooth enamel. Bone is a fibre-reinforced composite that makes up the skeletal systems of most animals. Bone is primarily made of partially mineralized collagen, a fibrillary structural protein with high tensile strength. The calcium phosphate provides a high compressive strength to the bone, and the organic proteins contribute to the mechanical response of bone like plastic deformation. The high fracture toughness of bone is associated with the crack deflection in the bone matrix and bone osteon for a cylindrical lamellar bone [33-36]. The unusual combination of mechanical properties observed in bone tissue has led to substantial interest in studying natural bone with an aim toward synthesizing bonelike materials, be it for forming replacement bones for medical use [37] or for nonmedical applications [38], figure 2.3(a) shows example of bone. Enamel is another example of a hard biological material. It is the most mineralized tissue in the human body (99% hydroxyapatite) and as a result it is the hardest. This acellular material is composed of long crystals of carbonated hydroxyl apatite. The rods are parallel and normal to the surface near the surface of the tooth, where their weaker interfaces channel surface cracks deeper into the enamel layer to prevent tooth chipping. Deeper in the enamel layer, the rods crisscross which prevents further propagation of cracks and pin cracks [39-41] example of crack propagation, channelling, and toughening mechanisms in tooth enamel is shown in figure 2.3(b).

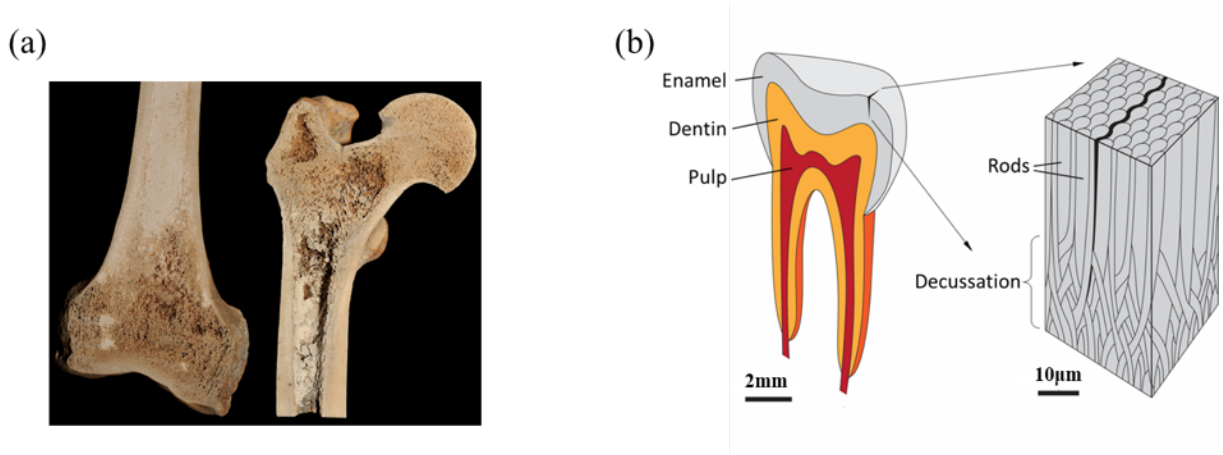

Figure 2.3: (a) picture of right femur bone (adapted from [42]), (b) crack propagation, channelling, and toughening mechanisms in tooth enamel (adapted from [43]).

2.3. Suture natural materials

Suture interfaces are mechanical structures found in rigid natural materials, that provide flexibility for locomotion, growth, and respiration examples are found in ammonoids, human skull, turtle shell, rhamphotheca of woodpeckers' beaks [44-51]. The suture interfaces are seams that connect stiffer components together. The geometry of suture ranges from nearly straight interfaces (infant skulls) [49, 50], to a more complicated fractal-like structures (ammonitic) [44, 47], and are said to have effect on the mechanical performance of the natural materials at different length scales.

2.3.1. Woodpeckers' beak as a material with suture

Woodpeckers beaks and head can withstand repeated and violent shocks associated with pecking trees. The brain is enclosed and protected by a plate-like high strength cranial bone which contains sutures that helps in energy absorption [52]. Woodpeckers' beaks are structural biocomposites which show unique hierarchical structure from macroscale to nanoscale [48]. They are made of an outer brittle mineral layer with rhamphotheca, a β-keratin protein [2, 48, 53]. The ductile protein is sandwiched between the rhamphotheca and a bony core which also helps in providing the strength needed by the beak. The geometry,

area fractions and mechanical properties of woodpeckers' beak changes along the length from the beak tip to the root, which makes it a functionally graded material (Figure 2.4a). The change in the mechanical properties along the length is associated with the modulus and area fraction of the constituents [48]. For example the total strength increases from the beak tip to the root, because the modulus of the bony region is greater than the rhamphotheca modulus and area fraction of the bony layer increase from tip to the root [48]. At the microscale level, the rhamphotheca comprises of overlapping keratin scales with diameter of approximately 50μm and the core of the beak is a closed-cell trabecular like bone [48]. The arrangement of these overlapping keratin scales is such that energy can be dissipated by frictional sliding (Figure 2.4b). Effective crack deflection can also occur in a way similar to those observed in other structural biological materials, like nacre, bone and tooth enamel [16, 33, 41]. The nanostructure of the rhamphotheca show a wavy suture line (Figure 2.4c), with collagen fibres which provide extra strength and stiffness, have the capability to withstand compressive loading, and also provide frictional forces which helps is dissipation and transmission of loads [45, 49, 50]. The fibres are the strongest in the longitudinal direction which corresponds to the direction of loading [48].

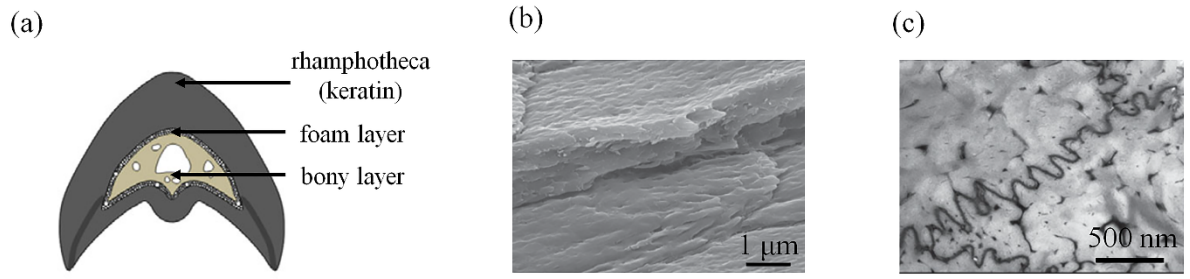

Figure 2.4: (a) Schematic of cross sectional view of the woodpeckers' beak; (b) scanning electron microscope image of the microstructure of rhamphotheca of woodpeckers' beak showing the rough surface of keratin scales; (c) transmission electron microscope image of the rhamphotheca of woodpeckers' beak showing the nanostructure of a cross sectional view that shows the wavy suture lines at the grain boundary [48]

2.3.2. Cranium

The brain is protected by a bony shell called the cranium. Interesting features of the cranium are the cranial sutures, which are lines containing bone edges and compliant collagen fibres that join the bony plates [54-56]. The morphology of cranial sutures evolve with human age and they are broadly classified into three types, depending on the overlapping and complexities [56, 57]. Butt suture joints is a type of suture joint where bones meet at a flat wall perpendicular to the outer surface, which are found in baby's cranium. Scarf suture joints consist of overlapping bones and are found in adults and interdigitating suture joints with a complex geometry and interlocked outer seam, and can be characterized by the number of interdigitations, depth and orientation from the cranial surface [58, 59]. Cranial sutures fulfill various functions depending on the level of infant development. In postnatal stages where there is a possibility of dramatic increase in the brain size, the suture provides flexibility for growth. In adulthood, sutures serve as shock absorbers to dissipate stresses, as well as have the capability to withstand compressive loads [49-51, 54-56, 58, 60, 61]. The skull is subjected to different kind of loadings from all directions in a lifetime: Tensile loadings due to the growth of internal organs during development, cyclic loading due to the nervous system, muscle contraction, mastication [62], and impact loadings due to falls or accidents. The geometry, complexity and fiber inclusion of the cranial sutures play important role in preventing the damage of the cranium. Experimental and computational studies have explored the stress distribution and biomechanics of cranial sutures under different loading conditions [49, 50]. These studies have shown that the wavy pattern of the suture lines increases the strain energy and therefore increases the energy absorption of the cranium. The wavy geometry also helps to delay strain localization, and collagen fibers improve frictional energy dissipation while providing additional strength. Bending strength of cranial sutures was found to increase with an increase in interdigitation [49, 50]. Figure 2.5 shows the

transition from a straight line suture found in newborn baby to an adult suture showing complex interdigitations.

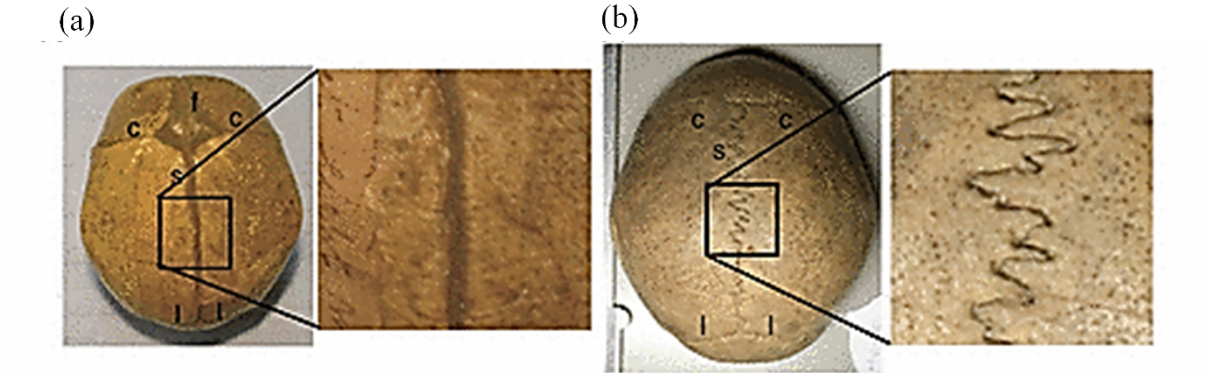

Figure 2.5: Development of skull suture interdigitation. (a) In the newborn human skull, the sagittal suture is straight; (b) In the adult human skull, the sagittal suture shows interdigitation [50].

Other examples of natural bony sutures are found in the carapace of turtle [45], cephalopods [44, 47], the linking girdle of diatoms [63], some species of fish including three-spine stickleback and boxfish [64, 65].

2.4. Bioinspired sutured materials

The design and fabrication of synthetic materials inspired from natural materials is a very active research area. An interesting reason for the study of the structures and mechanical properties of structural biological materials is to reproduce their exceptional mechanical properties like stiffness, hardness, and toughness amplification in synthetic materials [66]. Biological materials however display intricate structures and mechanisms which can be difficult to duplicate in synthetic materials. Bioinspired structural materials can be classified into eight groups: Layered, overlapping, suture, tubular, cellular, gradient, helical, and fibrous [67]. Each of these groups has unique characteristics and advantages and they had been fabricated by one or more fabrication method(s): (i) freeze casting [68] (ii) layer-by-layer deposition [69] (iii) recombinant technologies [70] (iv) magnetic manipulation [71], (v)

3D printing (additive manufacturing) [63], and (vi) laser engraving [43, 72]. A short discussion on two of these methods (3D printing and laser engraving) is discussed below.

2.4.1. 3D printing (additive manufacturing)

As opposed to subtractive manufacturing that chips away volume of materials until desired shape and size of sample is attained, 3D printing is an additive manufacturing process that build material in a layer-by-layer manner to form the desired model [73]. 3D printing is generally divided into four major methods: stereolithography (STL), fused deposition modeling (FDM), inkjet printing and selective laser sintering (SLS) [74]. Each of these 3D printing has its advantages and limitations which depend on the material type, build speed, cost, and curing/sintering materials [75]. For example STL uses an ultraviolet (UV) laser to trace the shape of 3D object by focusing on a bath of liquid photoresin, which cures when exposed to UV radiation. In fused deposition modeling, the part is produced by streams of material that harden immediately to form layers. During printing, these materials take the form of plastic threads or filaments, which are unwound from a coil and fed through an extrusion nozzle then heats up the material. The extrusion nozzle moves over the build platform horizontally and vertically making a cross-section of an object onto the platform. FDM can also be used to extrude ceramics and polymers. Inkjet printing and SLS sinter polymer powders together using different techniques. While inkjet printing uses toxic glue which makes it not useful for medical purposes, SLS uses high power laser to sinter polymer powders. All these methods require the 3D models which can be generated using any computer aided design (CAD) software or any other software that can create 3D images. These images are converted to STL input file which will be converted to a file recognized by the 3D printer. A number of researchers used the 3D printing technique to mimic the structures of some sutures and mechanical tested them to investigate the failure mechanism and deformation [63], and the pullout response of these sutures [76]. Figure 2.7 show

examples of fracture behaviour of bistable interlocked materials which were 3D printed by stereolithography printer with acrylonitrile butadiene styrene as the base material.

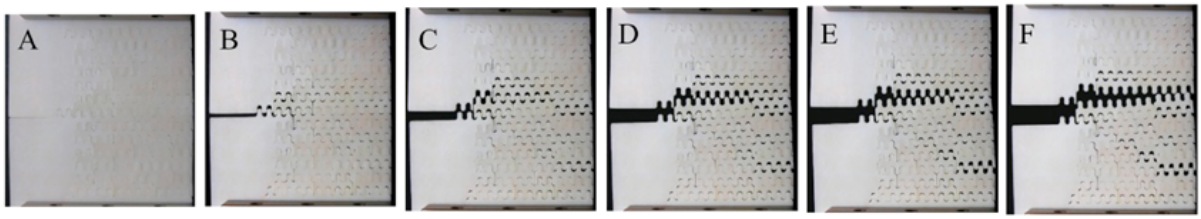

Figure 2.6: Images of sample of bioinspired 3D printed suture interface prototypes [63].

2.4.2. Laser engraving

Since their discovery, lasers have been used to alter the structure and shape of materials [43, 72, 77, 78]. Laser machining is non-conventional subtractive machining technique which is very efficient for the machining of brittle materials with low conductivity. A laser beam focusses onto the surface of materials, and the heat energy of the laser is transferred to the surface to heat and melt or vaporize the material. The depth of the trench formed depends on the laser power, beam spot diameter, and cutting speed [76, 77, 78]. There are different kinds of lasers depending on the type of laser medium used - solid state, excimer, dye, gas, or semiconductor laser. Mirkhalaf et al [43] used a laser engraving technique to fabricate bioinspired glass inspired from nacre microstructure. Examples of laser engraved glasses are shown in figure 2.7. The heat absorbed at the focal point generates thousands of microdefects in form of radial microcavities and microcracks from hoop stresses associated with thermal expansion [79, 80], and the energy of the unfocused beam does not alter the glass structure.

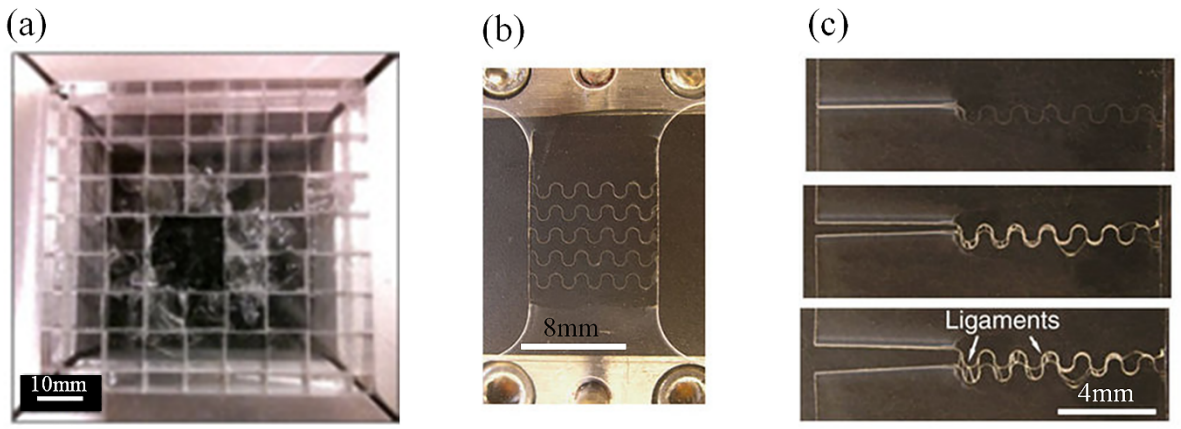

Figure 2.7: (a) An example of architecture glass plane after impact [72] (b) image of actual bioinspired glass sample for tensile test (c) bioinspired glass infiltrated with polyurethane [43]

2.5. References

1. Mayer, G., *Rigid biological systems as models for synthetic composites.* Science, 2005. **310**(5751): p. 1144-7.

2. Meyers, M.A., et al., *Structural biological composites: An overview.* Jom, 2006. **58**(7): p. 35-41.

3. Sarikaya, M. and I.A. Aksay, *Nacre of abalone shell: a natural multifunctional nanolaminated ceramic-polymer composite material.* Results and problems in cell differentiation, 1992. **19**: p. 1-26.

4. Verma, D., et al., *Mechanical response and multilevel structure of biomimetic hydroxyapatite/polygalacturonic/chitosan nanocomposites.* Materials Science and Engineering: C, 2008. **28**(3): p. 399-405.

5. Hamm, C.E., et al., *Architecture and material properties of diatom shells provide effective mechanical protection.* Nature, 2003. **421**(6925): p. 841-843.

6. Levi, C., et al., *A remarkably strong natural glassy rod: the anchoring spicule of theMonorhaphis sponge.* Journal of Materials Science Letters, 1989. **8**(3): p. 337-339.

7. Ashby, M.F. and Y.J.M. Bréchet, *Designing hybrid materials.* Acta Materialia, 2003. **51**(19): p. 5801-5821.

8. Ashby, M., *Designing architectured materials.* Scripta Materialia, 2013. **68**(1): p. 4-7.

9. Ritchie, R.O., *The conflicts between strength and toughness.* Nat Mater, 2011. **10**(11): p. 817-822.

10. Clegg, W.J., et al., *A simple way to make tough ceramics.* Nature, 1990. **347**(6292): p. 455-457.

11. Evans, A.G., *Perspective on the Development of High-Toughness Ceramics.* Journal of the American Ceramic Society, 1990. **73**(2): p. 187-206.

12. Fratzl, P. and R. Weinkamer, *Nature's hierarchical materials.* Progress in Materials Science, 2007. **52**(8): p. 1263-1334.

13. Ashby, M.F., *Chapter 4 - Material Property Charts*, in *Materials Selection in Mechanical Design (Fourth Edition)*. 2011, Butterworth-Heinemann: Oxford. p. 57-96.

14. Ashby, M.F., et al., *The Mechanical Properties of Natural Materials. I. Material Property Charts.* Proceedings: Mathematical and Physical Sciences, 1995. **450**(1938): p. 123-140.

15. Barthelat, F., *Biomimetics for next generation materials.* Philosophical Transactions of the Royal Society A: Mathematical, Physical and Engineering Sciences, 2007. **365**(1861): p. 2907-2919.

16. Barthelat, F., et al., *On the mechanics of mother-of-pearl: A key feature in the material hierarchical structure.* Journal of the Mechanics and Physics of Solids, 2007. **55**(2): p. 306-337.

17. Launey, M.E., M.J. Buehler, and R.O. Ritchie, *On the Mechanistic Origins of Toughness in Bone.* Annual Review of Materials Research, 2010. **40**(1): p. 25-53.

18. Currey, J.D. and J.D. Taylor, *The mechanical behaviour of some molluscan hard tissues.* Journal of Zoology, 1974. **173**(3): p. 395-406.

19. Chen, P.Y., et al., *Structure and mechanical properties of selected biological materials.* Journal of the Mechanical Behavior of Biomedical Materials, 2008. **1**(3): p. 208-226.

20. Munch, E., et al., *Tough, Bio-Inspired Hybrid Materials.* Science, 2008. **322**(5907): p. 1516-1520.

21. Zhu, D. and F. Barthelat, *A Novel Biomimetic Material Duplicating the Structure and Mechanics of Natural Nacre*, in *Mechanics of Biological Systems and Materials, Volume 2*, T. Proulx, Editor. 2011, Springer New York. p. 181-187.

22. Barthelat, F. and M. Mirkhalaf, *The quest for stiff, strong and tough hybrid materials: an exhaustive exploration.* Journal of The Royal Society Interface, 2013. **10**(89).

23. Kohn, A.J., *Encyclopedia of Evolution*. 2002, Oxford University Press.

24. Menig, R., et al., *Quasi-static and dynamic mechanical response of Haliotis rufescens (abalone) shells.* Acta Materialia, 2000. **48**(9): p. 2383-2398.

25. Rousseau, M., et al., *Multiscale structure of sheet nacre.* Biomaterials, 2005. **26**(31): p. 6254-62.

26. Currey, J.D., *Mechanical Properties of Mother of Pearl in Tension.* Proceedings of the Royal Society of London. Series B. Biological Sciences, 1977. **196**(1125): p. 443-463.

27. Espinosa, H.D., et al., *Merger of structure and material in nacre and bone – Perspectives on de novo biomimetic materials.* Progress in Materials Science, 2009. **54**(8): p. 1059-1100.

28. Barthelat, F. and R. Rabiei, *Toughness amplification in natural composites.* Journal of the Mechanics and Physics of Solids, 2011. **59**(4): p. 829-840.

29. Rabiei, R., A. Dastjerdi, and F. Barthelat, *Interfacial Fracture Toughness of Nacre*, in *Mechanics of Biological Systems and Materials, Volume 5*, B.C. Prorok, et al., Editors. 2013, Springer New York. p. 31-38.

30. Lawn, B., *Fracture of brittle solids*. 1993, Cambridge University Press.

31. Barthelat, F. and H.D. Espinosa, *An Experimental Investigation of Deformation and Fracture of Nacre–Mother of Pearl.* Experimental Mechanics, 2007. **47**(3): p. 311-324.

32. Barthelat, F., et al., *Mechanical properties of nacre constituents and their impact on mechanical performance.* Journal of Materials Research, 2006. **21**(8): p. 1977-1986.

33. Gupta, H.S., *Mechanisms of bone deformation and fracture.* IBMS BoneKEy, 2010. **7**(6): p. 218-228.

34. Nalla, R.K., J.H. Kinney, and R.O. Ritchie, *Mechanistic fracture criteria for the failure of human cortical bone.* Nat Mater, 2003. **2**(3): p. 164-168.

35. Ritchie, R.O., et al., *A fracture mechanics and mechanistic approach to the failure of cortical bone.* Fatigue & Fracture of Engineering Materials & Structures, 2005. **28**(4): p. 345-371.

36. Nalla, R.K., J.J. Kruzic, and R.O. Ritchie, *On the origin of the toughness of mineralized tissue: microcracking or crack bridging?* Bone. **34**(5): p. 790-798.

37. Ko, C.-C., et al., *Mechanical properties and cytocompatibility of biomimetic hydroxyapatite-gelatin nanocomposites.* Journal of Materials Research, 2006. **21**(12): p. 3090-3098.

38. Oyen, M.L., *The Materials Science of Bone: Lessons from Nature for Biomimetic Materials Synthesis.* MRS Bulletin, 2008. **33**(01): p. 49-55.

39. Imbeni, V., et al., *The dentin-enamel junction and the fracture of human teeth.* Nat Mater, 2005. **4**(3): p. 229-232.

40. Park, S., et al., *On the brittleness of enamel and selected dental materials.* Dental Materials. **24**(11): p. 1477-1485.

41. Yahyazadehfar, M., D. Bajaj, and D.D. Arola, *Hidden contributions of the enamel rods on the fracture resistance of human teeth.* Acta Biomaterialia, 2013. **9**(1): p. 4806-4814.

42. Jopp-Van Well, E., et al., *The assessment of adipocere to estimate the post-mortem interval – a skeleton from the tidelands.* Anthropologischer Anzeiger, 2016. **73**(3): p. 235-247.

43. Mirkhalaf, M., A.K. Dastjerdi, and F. Barthelat, *Overcoming the brittleness of glass through bio-inspiration and micro-architecture.* Nature communications, 2014. **5**: p. 3166.

44. Allen, E.G., *Understanding ammonoid sutures: New insight into the dynamic evolution of Paleozoic suture morphology*. Cephalopods Present and Past: New Insights and Fresh Perspectives, ed. N.H. Landman, R.A. Davis, and R.H. Mapes. 2007. 159-180.

45. Chen, I.H., W. Yang, and M.A. Meyers, *Leatherback sea turtle shell: A tough and flexible biological design.* Acta Biomaterialia, 2015. **28**: p. 2-12.

46. Cray, J., M.P. Mooney, and M.I. Siegel, *Timing of ectocranial suture activity in Pan troglodytes as related to cranial volume and dental eruption.* The Anatomical Record, 2010. **293**(8): p. 1289-1296.

47. Klug, C. and R. Hoffmann, *Ammonoid Septa and Sutures*, in *Ammonoid Paleobiology: From anatomy to ecology*, C. Klug, et al., Editors. 2015, Springer Netherlands: Dordrecht. p. 45-90.

48. Lee, N., et al., *Hierarchical multiscale structure-property relationships of the red-bellied woodpecker (Melanerpes carolinus) beak.* Journal of the Royal Society Interface, 2014. **11**(96).

49. Maloul, A., et al., *Characterization of craniofacial sutures using the finite element method.* Journal of Biomechanics, 2014. **47**(1): p. 245-252.

50. Miura, T., et al., *Mechanism of skull suture maintenance and interdigitation.* Journal of Anatomy, 2009. **215**(6): p. 642-655.

51. Moazen, M., et al., *Assessment of the role of sutures in a lizard skull: a computer modelling study.* Proceedings of the Royal Society B-Biological Sciences, 2009. **276**(1654): p. 39-46.

52. May, P.A., et al., *Woodpecker drilling behavior: An endorsement of the rotational theory of impact brain injury.* Archives of Neurology, 1979. **36**(6): p. 370-373.

53. Sanchez, C., H. Arribart, and M.M. Giraud Guille, *Biomimetism and bioinspiration as tools for the design of innovative materials and systems.* Nat Mater, 2005. **4**(4): p. 277-288.

54. Persson, M., B.C. Magnusson, and B. Thilander, *Sutural closure in rabbit and man: a morphological and histochemical study.* Journal of Anatomy, 1978. **125**(Pt 2): p. 313-321.

55. Pritchard, J.J., J.H. Scott, and F.G. Girgis, *The structure and development of cranial and facial sutures.* Journal of Anatomy, 1956. **90**(Pt 1): p. 73-86.3.

56. Cohen, M.M., *Sutural biology and the correlates of craniosynostosis.* American Journal of Medical Genetics, 1993. **47**(5): p. 581-616.

57. Kokich, V.G., *Age changes in the human frontozygomatic suture from 20 to 95 years.* American Journal of Orthodontics, 1976. **69**(4): p. 411-430.

58. Walmsley, C.W., et al., *Why the Long Face? The Mechanics of Mandibular Symphysis Proportions in Crocodiles.* PLOS ONE, 2013. **8**(1): p. e53873.

59. Kathe, W., *Comparative morphology and functional interpretation of the sutures in the dermal skull roof of temnospondyl amphibians.* Zoological Journal of the Linnean Society, 1999. **126**(1): p. 1-40.

60. Zhao, H., et al., *The suture provides a niche for mesenchymal stem cells of craniofacial bones.* Nat Cell Biol, 2015. **17**(4): p. 386-396.

61. Strait, D.S., et al., *Craniofacial Strain Patterns During Premolar Loading: Implications for Human Evolution*, in *Primate Craniofacial Function and Biology*, C. Vinyard, M.J. Ravosa, and C. Wall, Editors. 2008, Springer US: Boston, MA. p. 173-198.

62. Mao, J.J., X. Wang, and R.A. Kopher, *Biomechanics of Craniofacial Sutures: Orthopedic Implications.* The Angle Orthodontist, 2003. **73**(2): p. 128-135.

63. Lin, E., et al., *3D printed, bio-inspired prototypes and analytical models for structured suture interfaces with geometrically-tuned deformation and failure behavior.* Journal of the Mechanics and Physics of Solids, 2014. **73**: p. 166-182.

64. Yang, W., et al., *The armored carapace of the boxfish.* Acta Biomaterialia, 2015. **23**: p. 1-10.

65. Song, J., et al., *Quantitative microstructural studies of the armor of the marine threespine stickleback (Gasterosteus aculeatus).* Journal of Structural Biology, 2010. **171**(3): p. 318-331.

66. Meyers, M.A., et al., *Biological materials: A materials science approach.* Journal of the Mechanical Behavior of Biomedical Materials, 2011. **4**(5): p. 626-657.

67. Naleway, S.E., et al., *Structural Design Elements in Biological Materials: Application to Bioinspiration.* Advanced Materials, 2015. **27**(37): p. 5455-5476.

68. Deville, S., et al., *Freezing as a Path to Build Complex Composites.* Science, 2006. **311**(5760): p. 515-518.

69. Tang, Z., et al., *Nanostructured artificial nacre.* Nat Mater, 2003. **2**(6): p. 413-418.

70. Lazaris, A., et al., *Spider Silk Fibers Spun from Soluble Recombinant Silk Produced in Mammalian Cells.* Science, 2002. **295**(5554): p. 472-476.

71. Erb, R.M., et al., *Composites Reinforced in Three Dimensions by Using Low Magnetic Fields.* Science, 2012. **335**(6065): p. 199-204.

72. Mirkhalaf, M., J. Tanguay, and F. Barthelat, *Carving 3D architectures within glass: Exploring new strategies to transform the mechanics and performance of materials.* Extreme Mechanics Letters, 2016. **7**: p. 104-113.

73. X. Gu, G., et al., *Three-Dimensional-Printing of Bio-Inspired Composites.* Journal of Biomechanical Engineering, 2016. **138**(2): p. 021006-021006-16.

74. Wang, A., et al., *3D Printing for 21st Century Medical Learners: Opportunities for Innovative Research and Collaboration.* 2017, 2017. **7**(1).

75. Gibson, I., D.W. Rosen, and B. Stucker, *Development of Additive Manufacturing Technology*, in *Additive Manufacturing Technologies: Rapid Prototyping to Direct Digital Manufacturing*. 2010, Springer US: Boston, MA. p. 36-58.

76. Gattass, R.R. and E. Mazur, *Femtosecond laser micromachining in transparent materials.* Nat Photon, 2008. **2**(4): p. 219-225.

77. Her, T.-H., et al., *Microstructuring of silicon with femtosecond laser pulses.* Applied Physics Letters, 1998. **73**(12): p. 1673-1675.

78. Liu, X., D. Du, and G. Mourou, *Laser ablation and micromachining with ultrashort laser pulses.* IEEE Journal of Quantum Electronics, 1997. **33**(10): p. 1706-1716.

79. Salleo, A., T. Sands, and F.Y. Génin, *Machining of transparent materials using an IR and UV nanosecond pulsed laser.* Applied Physics A, 2000. **71**(6): p. 601-608.

Link between chapter 2 and chapter 3

In the previous chapter we discussed the structure and deformation mechanism of a selection of hard biological materials were discussed. It was discussed that when pushed to the extreme, the concept of using weak interfaces leads to sutured materials, which are now generating a growing interest in the materials research community. Some of the methods used to fabricate the materials in order to mimic their exceptional mechanical performance on synthetic materials were highlighted. Two of the emphasized methods will be used in this thesis. These techniques were chosen because of their high level of fidelity required to capture the complex geometries of sutures with sufficient accuracy. The next chapter is an article which was recently published in the *Journal of mechanics and physics of solids*, volume 102 (2017), 224-238. In this work we used analytical and finite element models to explore the mechanics of sutured materials with a relatively simple "jigsaw-like" geometry. These models, based on simple kinematics and contact mechanics, capture the effects of key design parameters (interlocking angle θ_0, and friction coefficient f) on the pullout response of the suture. The analytical models used both linear elasticity and non-Hertzian contact mechanics while the finite element models were developed to validate the underlying assumptions used in the analytical models. These models serve as guidelines for jigsaw-like sutures which are under tensile loads and with no adhesive between the interfaces.

Chapter 3

Bio-inspired “Jigsaw”-like interlocking sutures: Modeling, optimization, 3D printing and testing

Chapter 3: Bio-inspired "Jigsaw"-like interlocking sutures: Modeling, optimization, 3D printing and testing

I. A. Malik, M. Mirkhalaf and F. Barthelat*

Department of Mechanical Engineering, McGill University, 817 Sherbrooke Street West,

Montreal, QC H3A 2K6, Canada

Journal of mechanics and physics of solids, Volume 102, May 2017, Pages 224–238

https://doi.org/10.1016/j.jmps.2017.03.003

3.1 Abstract

Structural biological materials such as bone, teeth or mollusk shells draw their remarkable performance from a sophisticated interplay of architectures and weak interfaces. Pushed to the extreme, this concept leads to sutured materials, which contain thin lines with complex geometries. Sutured materials are prominent in nature, and have recently served as bioinspiration for toughened ceramics and glasses. Sutures can generate large deformations, toughness and damping in otherwise all brittle systems and materials. In this study we examine the design and optimization of sutures with a jigsaw puzzle-like geometry, focusing on the non-linear traction behavior generated by the frictional pullout of the jigsaw tabs. We present analytical models which accurately predict the entire pullout response. Pullout strength and energy absorption increase with higher interlocking angles and for higher coefficients of friction, but the associated high stresses in the solid may fracture the tabs. Systematic optimization reveals a counter-intuitive result: the best pullout performance is achieved with interfaces with low coefficient of friction and high interlocking angle. We finally use 3D printing and mechanical testing to verify the accuracy of the models and of the optimization. The models and guidelines we present here can be extended to other types of geometries and sutured materials subjected to other loading/boundary conditions. The

nonlinear responses of sutures are particularly attractive to augment the properties and functionalities of inherently brittle materials such as ceramics and glasses.

Keywords: Suture, analytical model, finite element simulation, optimization, 3D printing

3.2 Introduction

Natural hard materials such as bone [1, 2], tooth enamel [3], sea shells [4], or turtle carapace [5] display unique and attractive combinations of strength, toughness, deformability and puncture resistance, properties that are difficult to combine in engineering materials [6]. This outstanding performance is possible by their internal architectures, which can be described as assemblies of stiff and strong building blocks (collagen or chitin fibers, mineral tablets) [7] bonded by weaker interfaces. These interfaces are as important as the building blocks and fulfill critical structural functions [8]: They deflect and channel cracks into toughening configurations [9, 10], they enable large deformations [11] and they provide deformation hardening to spread energy dissipative mechanisms throughout large volumes of the materials [7, 8, 12-15]. The mechanical behavior of these interfaces is typically nonlinear and governed by friction or by the deformation of nanometers-thick layers of organic materials. In addition the morphology of the interfaces plays a critical role in their mechanical response, and as seen in nacre from seashells it can act as a source of progressive locking and "geometric hardening" that delays strain localization and spreads non-elastic deformations over large volumes of materials [14]. In natural suture lines, the interfaces have complex geometries and re-entrant features, as observed in the beak of woodpeckers [16] (Figure 3.1a), the linking girdles of diatoms (Figure 3.1b) [17], the armor of threespine stickleback fishes [18] (Figure 3.1c), the cranial bone [19, 20] (Figure 3.1d), the ammonites shells [12] (Figure 3.1e) or turtle shells [12, 21] (Figure 3.1f). In these examples the suture lines can channel large

deformations, damp shocks and vibrations or absorb impact energy [22]. The suture lines vary in geometry and complexity across species [23-25], and include straight suture lines as observed in new born human skull [25], triangular or wavy sutures with re-entrant features as seen in woodpecker beak [16], interlocked shapes as seen in diatoms [26, 27] and ammonite shells [28] (Figure 3.1). The mechanical strength and toughness of the suture lines are largely governed by their morphology. For example, brittle sinusoidal sutures can be up to three times tougher than straight interfaces made of the same bonding material [29, 30]. In ductile materials, the positioning of second phase particles into a sinusoidal pattern can guide the cracks into "pre-engineered" paths that increase toughness by a factor of 2-3 compared with the same material with random distribution of particles [31]. Stress analysis also revealed that periodic triangular sutures homogenize the transfer of stress across the interface, which is beneficial to overall structural performance [17, 28]. Recent studies have also shown that increasing the number of hierarchies within the triangulated sutures, as seen in ammonites, can augment their mechanical properties [32, 33]. The concept of sutures with tailored geometries and locking features were recently demonstrated in glasses and ceramics, which resulted in large deformations, energy absorption and enhanced toughness in otherwise all-brittle materials [34, 35]. While these materials demonstrated the potential of architecture and sutures as weaker interfaces to enhance the overall mechanical performance, models and optimization approaches are yet to be developed in order to get the most of this strategy. The stiffness, strength and toughness of sutured materials were captured in models using either only elasticity and small deformations [21, 32, 33] or elastic-plastic models [30], but the mechanisms and stresses associated with large pulling displacements and nonlinear geometrical locking behaviors are not well understood. Here we propose a set of models and experiments to characterize the full pullout response of a jigsaw-like suture based on frictional contact and elasticity. We first present an analytical model based on linear elasticity

and frictional contact, which we compared with finite element models. A strategy to optimize the suture is then proposed based on the models. The modeling and optimization are finally verified using 3D printing and mechanical testing.

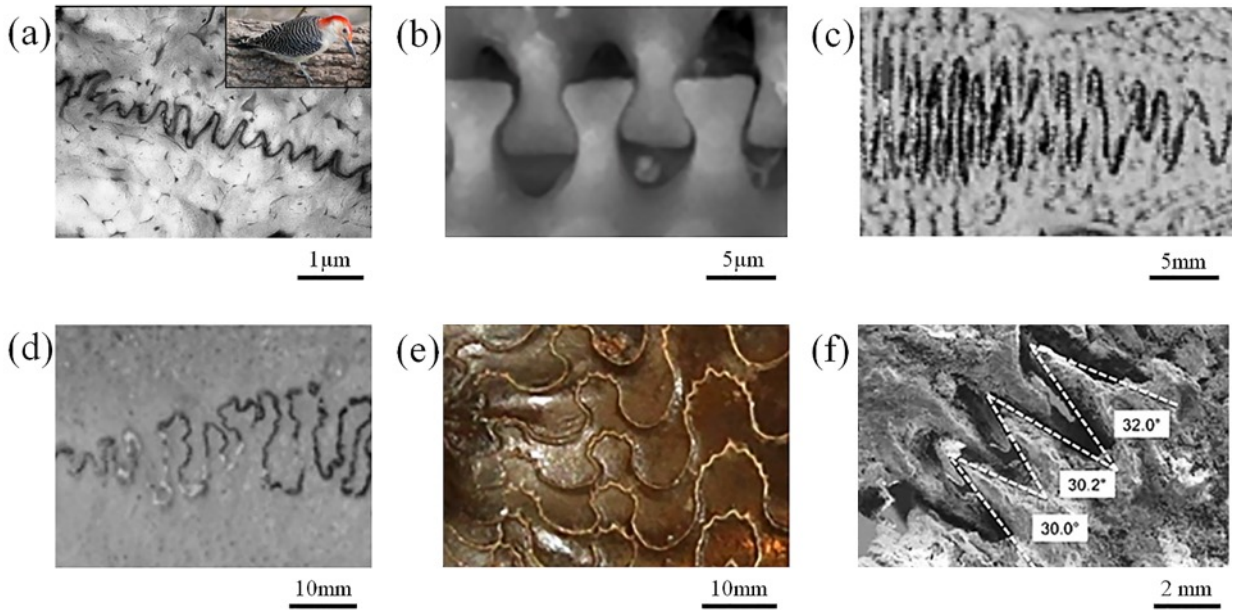

Figure 3.1: Examples of sutured interfaces in nature: (a) red-bellied woodpecker (*Melanerpes carolinus*) beak (adapted from [16]) , (b) Linking girdles of diatoms (adapted from [17]) , (c) marine threespine stickleback (*Gasterosteus aculeatus*) (adapted from [18]), (d) Pan troglodytes cranial sutures (adapted from [36]), (e) Ammonite shell (*Ceratitic ammonoid*) with intricate suture lines [28] (f) osteoderms of a leatherback sea turtle shell (adapted from [5])

3.3 Overview of the "jigsaw" suture

The sutured interfaces we considered in this work have re-entrant rounded features, forming interlocks similar to a jigsaw puzzle (Figure 3.2). The geometry was built from arcs of circles of radius *R*, and blended at locations defined by an interlocking angle θ_0. Rounded features were used to minimize stress concentrations in the solid. The patterns are periodic along the suture so that the geometry can be captured with the unit cell shown on Figure 3.2a. We only considered sutures which are symmetric about a vertical axis, and which also display a 180º rotational symmetry, so that upper and lower solid parts of the suture are identical (Figure 3.2a). The geometry of the suture has therefore only two independent parameters *R* and θ_0. It is however useful to also write the length *L* and the width *w* of the tab (Figure 3.2a):

$$L = 2R(1 + \sin\theta_0) \tag{3.1}$$

$$w = 4R\cos\theta_0 \tag{3.2}$$

The interlocking angle θ_0 clearly governs the level of geometrical interlocking of the tabs (Figure 3.2b). Only the cases where $\theta_0 > 0°$ generate geometrical interlocking. In addition, the contours of the tabs were not allowed to intersect, leading to the geometrical constraint $\theta_0 < 60°$. Figure 3.2b shows how the level of interlocking increases when θ_0 is increased up to $\theta_0 = 60°$ which corresponds to the extreme case where the re-entrant regions of the suture intersect tangentially.

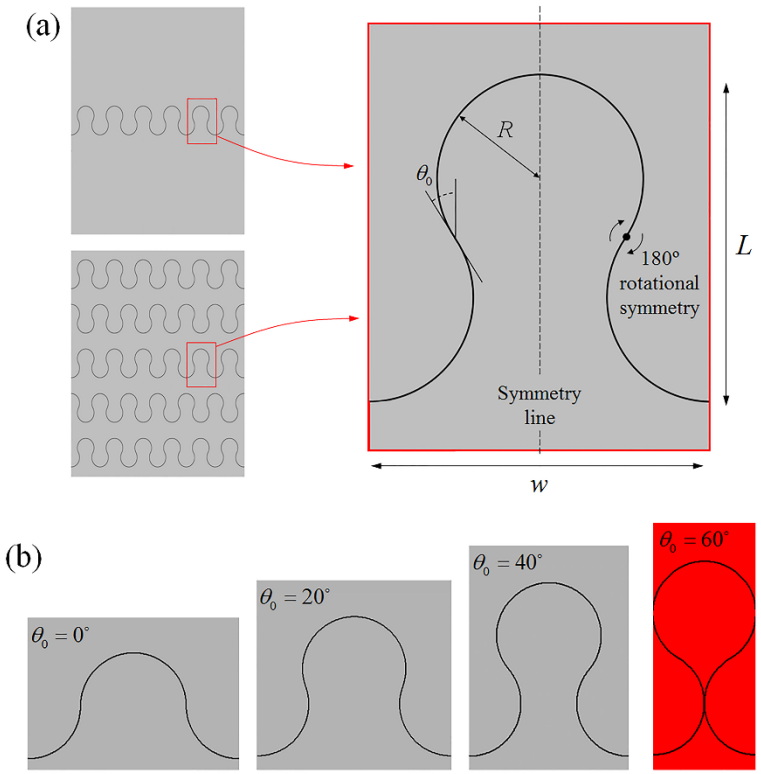

Figure 3.2: (a) An individual suture with jigsaw locking features, and a material containing multiple sutures in series. The geometry and mechanics of these systems can be captured by the unit cell shown; (b) The "strength" of the geometrical interlocking is governed by the interlocking angle θ_0, where $\theta_0 < 60°$ to prevent the re-entrant regions of the tabs to intersect (case highlighted in red).

3.3 Analytical model of pullout response

In this work we focused on the pullout behavior of the suture, where the suture is pulled along the axis of the tabs (along the vertical direction on Figure 3.2). The solid part of the suture was assumed to be isotropic and linear elastic (modulus E and Poisson's ratio ν). We

also only considered the cases where the cohesion of the suture is generated by geometric interlocking and friction, with no adhesive at the interfaces. The pullout mechanism associated with the suture can therefore be captured using linear elasticity and frictional contact mechanics. A representative volume element of a suture in a thin plate of thickness *t* is shown on Figure 3.3a with key dimensions: tab radius *R*, interlocking angle θ_0, length *L* and width of the tab *w*, height of the upper and lower solid domains *h*. We assumed a thin plate, so plane stress conditions are used (the model can easily be transposed to plane strain). The suture was subjected to a uniform pull by imposing:

$$\begin{cases} u_y(x,-h)=0 \\ u_y(x,L+h)=u \end{cases} \tag{3.3}$$

The left and right boundaries were subjected to the periodic boundary conditions:

$$\begin{cases} u_x(w/2,y)-u_x(-w/2,y)=w\bar{\varepsilon}_x \\ u_y(w/2,y)=u_y(-w/2,y) \end{cases} \tag{3.4}$$

Where $\bar{\varepsilon}_x$ is the average strain in the *x* (transverse) direction. The geometry and the loading conditions are symmetric about axis *y* (Figure 3.3a) and therefore the displacements must also satisfy:

$$u_x(x,y)=-u_x(-x,y) \tag{3.5}$$

Combining equations (4) and (5) gives the periodic-symmetric boundary conditions:

$$\begin{cases} u_x(0,y)=0 \\ u_x\left(\dfrac{w}{2},y\right)=\dfrac{w}{2}\bar{\varepsilon}_x \end{cases} \tag{3.6}$$

We now note that $\bar{\varepsilon}_x \neq 0$ would involve elastic deformations in the two solid domains above and below the suture, with uniform strains sufficiently far from the jigsaw tab. However if *h* is sufficiently large, the stiffness of the solid regions along the transverse direction is high

enough so that no deformation can occur in the transverse direction, $\bar{\varepsilon}_x = 0$. The boundary conditions then simply become:

$$\begin{cases} u_x(0,y) = 0 \\ u_x(w/2,y) = 0 \end{cases} \tag{3.7}$$

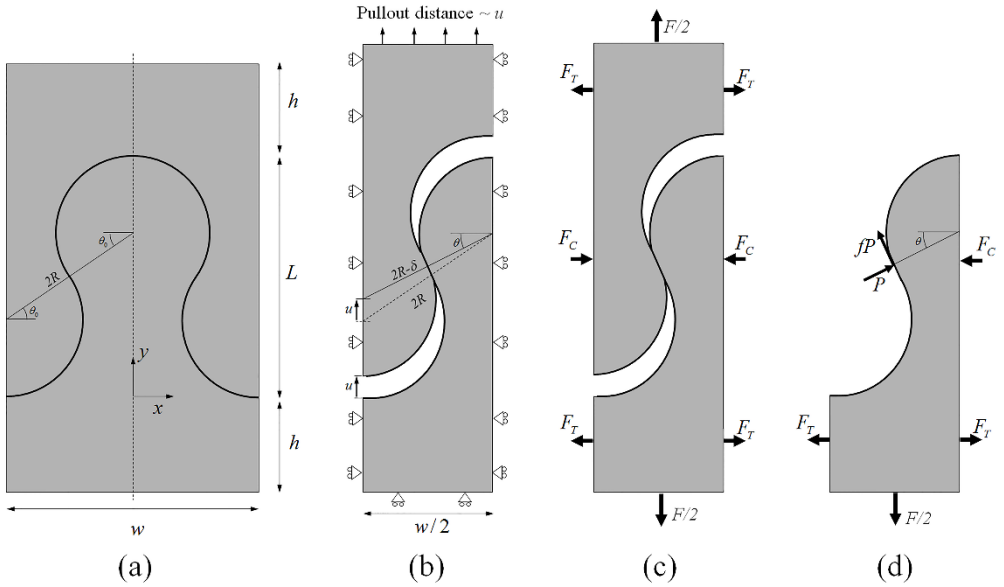

Figure 3.3: (a) Representative volume element of the initial geometry for the jigsaw tab; (b) The same model with symmetry and boundary conditions applied. (c) Free body diagram of the unit cell; (d) free body diagram of the lower tab only, exposing the normal and frictional forces transmitted at the contact between the tabs.

Figure 3.3b shows the model after symmetry was applied, with the boundary conditions corresponding to equations (3.3) and (3.7). This simplified geometry was used to characterize the kinematics and equilibrium of the suture. Assuming that the elastic deformations are negligible compared to the displacement generated by sliding at the interfaces and pullout, the comparison of the initial and deformed configurations yields the kinematic relations:

$$(2R-\delta)\cos\theta = 2R\cos\theta_0 \tag{3.8}$$

$$u = 2R\sin\theta_0 - (2R-\delta)\sin\theta \tag{3.9}$$

In these expressions θ is the angle of the line intersecting the centers of the two circular tabs and δ is the interference between the two tabs, which corresponds to the change of distance between the centers of the two tabs. Initially equal to *2R*, that distance becomes *2R*-δ as the

tabs are pulled apart (Figure 3.3b). The interference δ must be accommodated by local deformations of the tabs, which are governed by contact mechanics. In this context, δ represents the relative "approach" between the two rounded features of the tabs. The kinematics of the system is then fully characterized by the angle θ. During pullout θ decreases monotonically from $+\theta_0$ (initial configuration) down to $-\theta_0$ (the tabs lose contact). The geometric interference δ generates a contact force which results in the pullout force along the (vertical) axis of the tab, but also to (horizontal) compressive forces F_C in the tabs region on both left and right sides of the model. These compressive forces are balanced by tensile forces F_T on the left and right hand sides of the model, so that the sum of forces acting on the right hand side of the model is zero ($F_C = 2F_T$, Figure 3.3c). Figure 3.3d shows a free body diagram of the lower tab only, which exposes the contact forces decomposed as a normal force P and a frictional force fP acting against the direction of the pull. Balancing these forces along the vertical direction gives the pullout force F:

$$F = 2P(\sin\theta + f\cos\theta) \tag{3.10}$$

The forces transmitted between the two tabs are determined from the solution for the contact between two identical disks. The solution of this non-Hertzian contact mechanics problem provides the approach δ (corresponding to the interference defined above and shown on figure 3.3b) as [37]:

$$\delta = \frac{a^2}{2R}\left[2\ln\left(\frac{4R}{a}\right) - 1\right] \tag{3.11}$$

Where a is the half width of the contact surface which in plane stress is given by:

$$a^2 = \frac{4PR}{\pi t E} \tag{3.12}$$

Where t is the thickness of the tab and E is the elastic modulus of the solid material. Equations (3.8) through (3.12) form a set of equations which can be solved to determine the

pullout force F as function of the pullout distance u, for different parameters R, θ_0 and E. The angle θ is used as a kinematic parameter which evolves from $+\theta_0$ to $-\theta_0$ during pullout. The non-dimensional interference is first determined from equation (3.8):

$$\frac{\delta}{R} = 2\left(1 - \frac{\cos\theta_0}{\cos\theta}\right) \tag{3.13}$$

This expression is then combined with equation (3.9) to obtain the non-dimensional pullout distance:

$$\frac{u}{L} = \frac{\sin\theta_0 - \cos\theta_0 \tan\theta}{1 + \sin\theta_0} \tag{3.14}$$

Here the opening u is normalized by the length of the tab L in order to get a measure of the global tensile strain in the tab generated by pullout. Meanwhile, the non-dimensional interference can be used in combination with the contact equations (3.11) and (3.12) to give:

$$\frac{\delta}{R} = \frac{2}{\pi}\frac{P}{RtE}\left[\ln\left(4\pi\frac{RtE}{P}\right) - 1\right] \tag{3.15}$$

This equation can be solved numerically to provide a non-dimensional contact force $\frac{P}{RtE}$, which can then be used to determine the non-dimensional pullout force, using equation (3.10):

$$\frac{F}{RtE} = \frac{2P}{RtE}(\sin\theta + f\cos\theta) \tag{3.16}$$

However, here we prefer to use $\frac{F}{wtE}$, which provides a direct measure of the average tensile stress applied on the suture where w is the width of the tab (Equation (3.2) and Figure 3.2a) and t is the thickness of the tab (wt is therefore the cross-sectional area of the tab). Combining equations (3.2) and (3.16) gives:

$$\frac{F}{wtE} = \frac{P}{RtE}\left(\frac{\sin\theta + f\cos\theta}{2\cos\theta_0}\right) \tag{3.17}$$

Figure 3.4 shows a set of typical pullout responses obtained from this model. The pullout force-displacement curve for the case with no friction (f=0) has a sinusoidal shape where the pullout force increases up to a maximum value, and then decreases again to zero at θ=0. At this particular point the interference δ and the normal contact force P are maximum, but since P acts along the direction transverse to the pull, this force does not generate any axial pullout force. Beyond this point, the contact force P is acting along the direction of pullout, and the tabs "push" on one another. At this stage F therefore becomes compressive to maintain equilibrium. The pullout force F eventually completely vanishes when the tabs lose contact, at $\theta=-\theta_0$, corresponding to $\frac{u}{L}=\frac{2\sin\theta_0}{1+\sin\theta_0}$. In the cases where f >0, the additional frictional contact force fP continuously resists pullout, which translates into a tensile pullout force even beyond θ =0 (Figure 3.4). Equation (3.16) indicates that if $f>\tan\theta_0$, the pullout force F is positive throughout the entire pullout process.

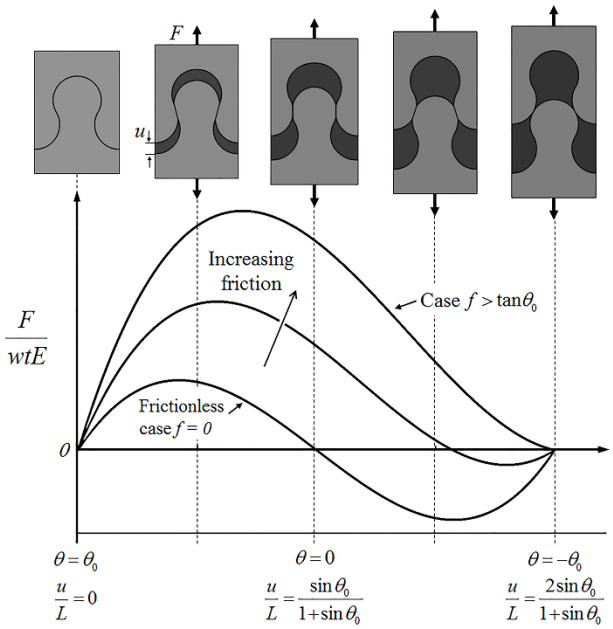

Figure 3.4: Typical traction separation curves obtained from the analytical pullout model using three different friction coefficients. The deformed shape of the system is also showed at five different stages, from initial configuration to complete pullout.

Figure 3.5a and 3.5b show the effects of the interlocking angle θ_0, and friction coefficient f on the pullout response of the suture. We first note that the pullout force is proportional to the modulus of the bulk material E, because the entire process is governed by elastic deformations in the contact region. Higher interlocking angles θ_0 increase the strength because of increased geometrical interlocking, and also increase the maximum pullout distance because the tabs stay in contact over a longer pullout distance (equation (3.14)). Higher coefficients of friction f increase the strength because of increased friction at the contact point, but do not change the maximum pullout distance, which is governed by geometry only. The friction coefficient f and interlocking angle θ_0 have therefore positive effects on the strength and energy absorption. These parameters cannot however be increased indefinitely because the high stresses in the solid parts may fracture the tab, prematurely ending the pullout process. This detrimental failure mode is considered in the next section of the analysis.

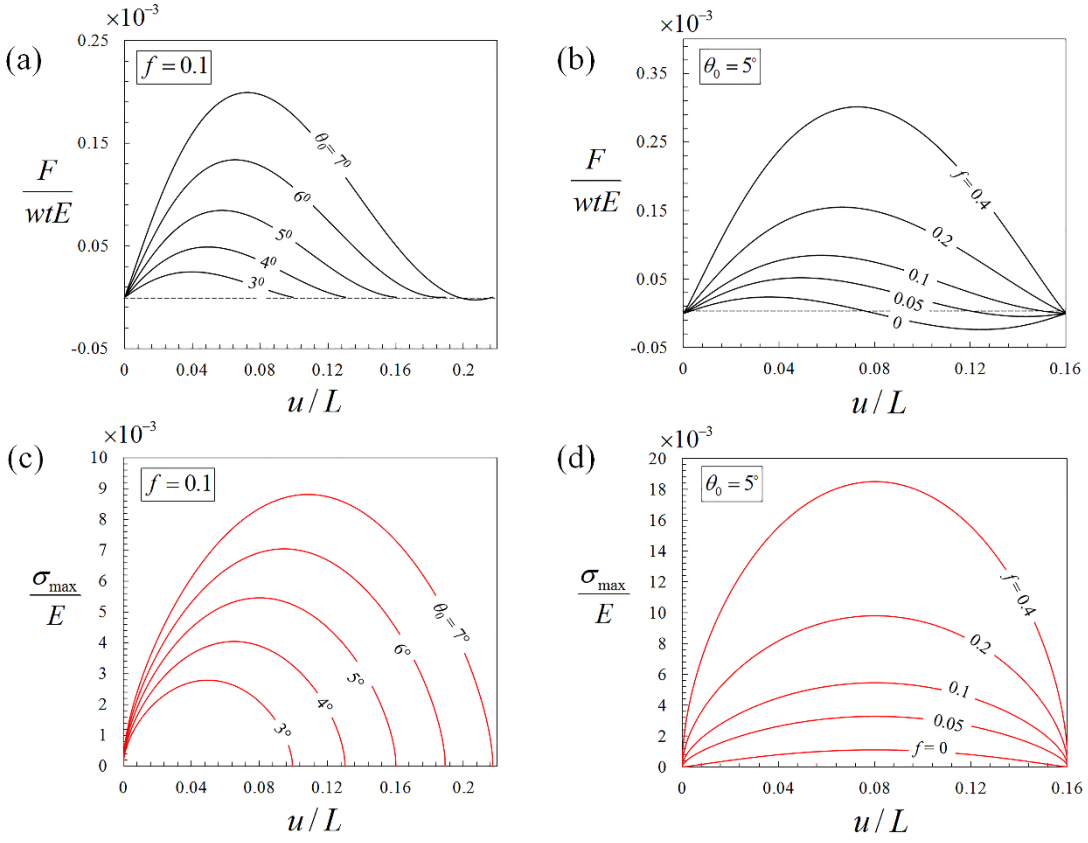

Figure 3.5: Effects of (a) interlocking angle θ_0 and (b) friction f on the pullout response of the suture; effects of (c) interlocking angle θ_0 and (d) friction f on maximum tensile stress in the solid tabs.

In this work we focus on the case where the tabs are made of a brittle material, so that failure of the solid tabs may be predicted by monitoring the maximum principal stress in the tabs. The maximum tensile stress in the tabs was estimated by combining two solutions: (i) a hole in an infinite plate loaded by a point force (figure 3.6i), and (ii) frictional contact mechanics (figure 3.6ii). In both cases, the maximum tensile stress occurs at the surface of the solid (in the direction tangential to the surface), and at the trailing edge of the contact between the sliding tabs.

(i) Hole in an infinite plate loaded by a frictionless pin in the in-plane direction [38, 39]: in this configuration the inner side of a hole is loaded by a contact force acting along the radial direction (Figure 3.6i). The resulting maximum tensile stress is the tangential stress at the edge of the contact area. If the contact area is small ($a << R$) then the stress is given by [38, 39]:

$$\sigma_{\max}^{(P)} = \frac{P}{Rt}\frac{5-\nu}{2\pi} \tag{3.18}$$

Where v is the Poisson's ratio of the solid material. The stress is simply proportional to the contact force P. We note that if $R \to +\infty$ (which corresponds to the case of a point force applied in the normal direction on the surface of a half-space), one recovers $\sigma_{\max}^{(P)} \to 0$.

(ii) Sliding frictional contact: If f >0, the sliding of the tab generates frictional forces and shear tractions acting on the contact area. These surface tractions generate tensile stresses which are maximum at the trailing edge of the sliding contact. Assuming that the contact area is small ($a<<R$) the effect of surface curvature can be neglected and the maximum tangential stress is [37]:

$$\sigma_{\max}^{(fP)} = \frac{4Pf}{\pi t a} \tag{3.19}$$

Superposition of these two solutions gives the total stress at the trailing edge of the contact:

$$\sigma_{\max} = \sigma_{\max}^{(P)} + \sigma_{\max}^{(fP)} = \frac{P}{Rt}\frac{5-\nu}{2\pi} + \frac{4Pf}{\pi ta} \tag{3.20}$$

Or, after normalization:

$$\frac{\sigma_{\max}}{E} = \frac{1}{2\pi}\frac{P}{RtE}\left[(5-\nu)+8\frac{R}{a}f\right] \tag{3.21}$$

Note that the stress is always highest at the edge of the contact region, even for f =0. The tensile stress at the root of the tab (at the smallest cross section) was always smaller than contact stresses. Figure 3.5c and 3.5d shows the maximum stress as function of normalized pullout distance. The maximum stress is always positive, even if the pullout force F becomes negative. This can be explained by equation (3.21), which shows that $\sigma_{\max}$ is proportional to the normal contact force P, which is always positive. As expected, the maximum stress increases with interlocking angle and friction (Figure 3.5c,d), and these stresses can be up to 60 times higher than the pullout traction $\frac{F}{wtE}$. The solutions also show that frictional stresses (second term in equation 3.21) largely govern the maximum stresses in the tab. Frictional stresses are therefore the main limiting factor for the design of the tabs. Design and optimization are examined in more details in section V.

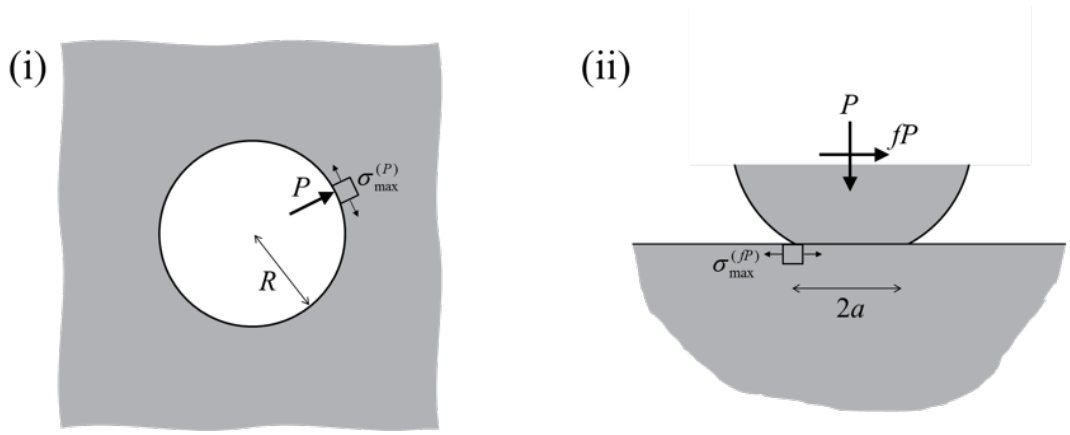

Figure 3.6: The two configurations used to derive the maximum stress in the tabs: (i) Point force P applied radially on the inner edge of a hole in an infinite plate; (ii) Sliding disk on a half space (normal force =P, frictional force = fP). In both cases, the location of the maximum tensile stress is shown. These two solutions are superimposed to obtain the maximum stress in the solid part of the tabs.

3.4 Finite elements simulations

In this section, we present finite element simulations for the pullout of the tabs. The objectives were to assess the validity of key assumptions in the analytical model, and to develop a platform which may be used for more complex sutures where analytical solutions may not be possible. Matlab (R2016a, MA, US) was used to automatically generate APDL input files for ANSYS (version 15.0, PA, US) [40] from the parameters f and θ_0 (R =1 for all simulations). The bulk of the material was meshed with quadratic, plane stress element (PLANE 183), and contact elements (CONTA 172, TARGE 169, symmetric contact) were used to simulate sliding and frictional contact at the interface. The mesh was refined to an element size of R/5000 near the interfaces to ensure converged, mesh independent results. Figure 3.7a shows a typical finite element mesh for the jigsaw geometry. The simulations were performed in about 400 time steps (checked for convergence) and the results were post-processed automatically using ANSYS ADPL and Matlab. This procedure was used to automatically run models [41] for 80 combinations of θ_0 and f. Figure 3.7d and 3.7e are representative comparisons which show excellent agreement between the finite elements and analytical predictions in terms of pullout response and maximum tensile stress within the material. The maximum stress from the finite element model also always occurred at the edge of the contact region (Figure 3.7b, 3.7c), in accordance with the predictions form the analytical solution. Finite elements and analytical solutions are both subjected to approximations and therefore neither of these models are exact solutions that could be used for validation. However, the fact that both models agree to a large extent suggests that they can capture the response of the system with an acceptable level of accuracy. For the case of the simple jigsaw geometry considered here, the analytical solution is easier and faster to

implement and use, and therefore it was used for the design optimization presented in the next section.

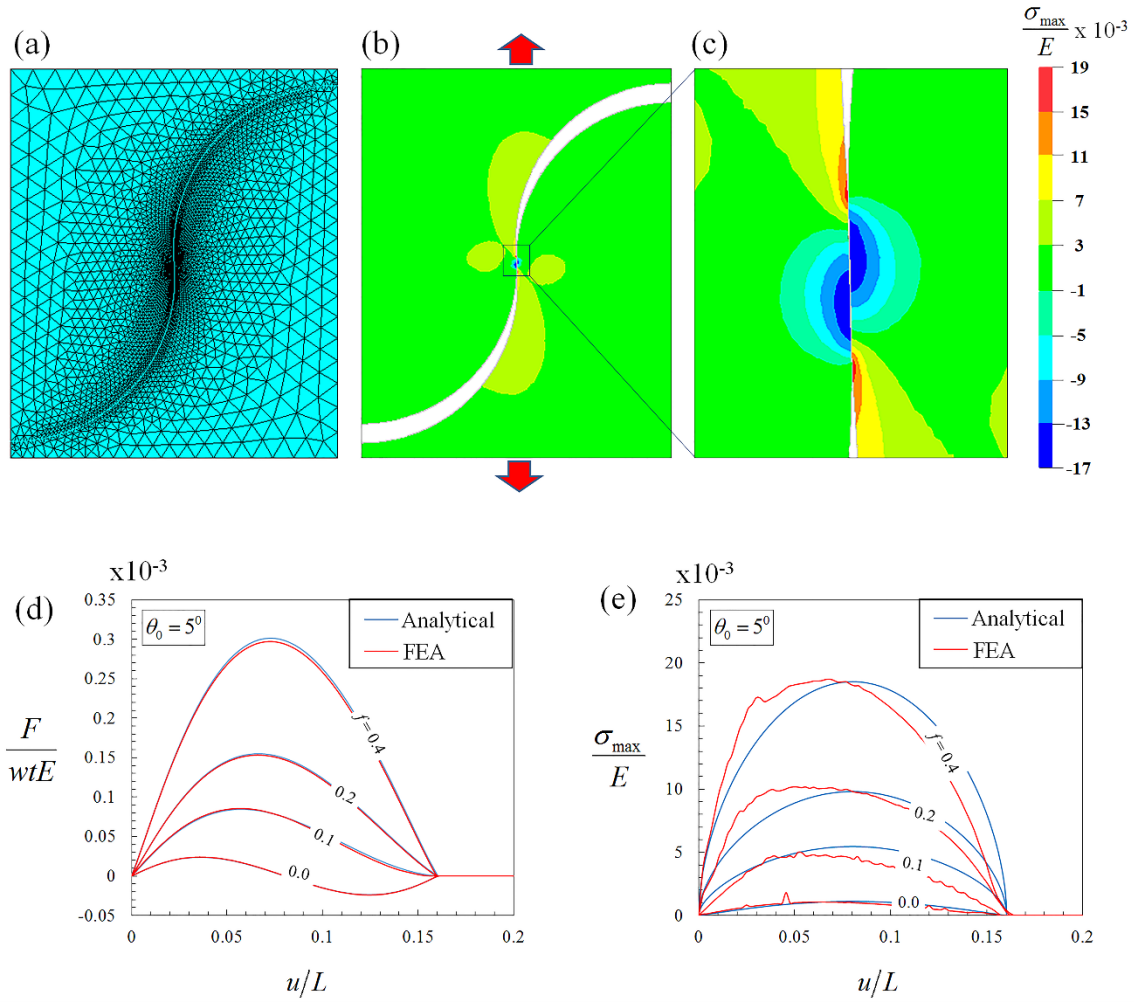

Figure 3.7: (a) An example of a meshed finite element model of the jigsaw tabs ($\theta_0 = 5^0$); (b) and (c) contour plots of maximum principal stress for $\theta_0 = 5^0$ and $f = 0.4$; (d) and (e) traction and stresses as function of pullout distance showing a good agreement between the analytical and finite elements results.

3.5 Design optimization

The models developed for pullout showed that increasing either θ_0 or f improves the pullout response of jigsaw tab, but also gives rise to tensile stresses in the solid material which can fracture the tabs. This failure mode is considered detrimental since it prematurely interrupts the dissipative mechanisms at the interfaces. Here we performed an optimization approach based on exhaustive search of the design space to identify the best combination(s) of design

parameters for any given set of desired of normalized stiffness, strength, maximum extension, and energy absorption. The normalized stiffness of the suture is defined as:

$$\frac{E^*}{E} = L\frac{d}{du}\left(\frac{F}{wtE}\right)_{u=0} \tag{3.22}$$

The strength is simply $\frac{F_{\max}}{wtE}$, the maximum elongation is $\frac{u_{\max}}{L}$ and the energy absorbed is given by the area under the pullout force-displacement curve:

$$\frac{U}{wtLE} = \int_0^{u_{\max}} \frac{F}{wtE}\frac{du}{L} \tag{3.23}$$

Figure 3.8a-d show contour lines (the blue lines) for these four properties as function of f and θ_0. All properties increase with f and θ_0. The frictionless case f =0 can generate stiffness strength through purely geometric interlocking, but it does not absorb energy. The limiting factor for the design is the fracture of the solid tabs, which is governed by the strength of the material. The tabs will therefore fracture when $\sigma_{\max} = \sigma_S$, or $\frac{\sigma_{\max}}{E} = \frac{\sigma_S}{E}$ where $\sigma_{\max}$ is the maximum tensile stress predicted from the model (equation 3.21) and σ_S is the tensile strength of the solid material. For most engineering materials the ratio between the tensile strength and modulus is in the range of $\frac{\sigma_S}{E} = \frac{1}{1000}$ to $\frac{\sigma_S}{E} = \frac{1}{100}$ [42]. The contour lines for $\frac{\sigma_{\max}}{E} = \frac{1}{1000}$ and $\frac{\sigma_{\max}}{E} = \frac{1}{100}$ are therefore superimposed in red on figure 3.8a-d. These lines define the boundaries of gray areas in the upper right portion of the diagram, and any combination of f and θ_0 in the greyed areas of these diagrams leads to the brittle fracture of the tabs. The optimum designs in terms of f and θ_0 will make the most of the solid material and will lie one of the red lines corresponding to the $\frac{\sigma_S}{E}$ ratio for the material considered. These diagrams can therefore be used to identify the optimum suture properties that can be achieved by simply intersecting the contour lines of properties with the limiting lines for tab

fracture. For example, if the friction at the interface is f =0.15 and the material of the tabs is relatively strong ($\frac{\sigma_S}{E} = \frac{1}{100}$), the point where the horizontal line f =0.15 and the contour line $\frac{\sigma_S}{E} = \frac{1}{100}$ intersect gives the optimum interlocking angle of about θ_0 =7°. On figure 3.8b that point corresponds to an optimum suture strength or about $\frac{F_{\max}}{wtE} = 0.2 \times 10^{-3}$. The coordinates of these intercepts was collected for all values of f, with the results displayed on figure 3.9. These plots can serve as guidelines for optimization: with a given friction coefficient f, the optimum stiffness, strength, elongation and energy absorption can be easily identified, along with the interlocking angle θ_0 that will achieve this optimized property. For example, for relatively weak and stiff materials such as ceramics and glasses (σ_s/E=1/1000), the value of interlocking angles and friction coefficients that will prevent tab fracture are small and cover a narrow range (θ_0=2° to 4^0 and f = 0 to 0.05). For stronger and/or more compliant materials such as metals and polymers (σ_s/E=1/100), the range of interlocking angles and friction coefficients that will prevent tab fracture is much wider (θ_0=2° to 12^0 and f = 0 to 0.5). The optimization results also reveals a counterintuitive but important guideline. Parametric studies show that higher coefficient of friction can promote strength, stiffness and energy absorption. However, the high frictional stresses at the interface also generate large tensile stresses in the contact areas, which can precipitate the fracture of the tabs. In contrast, low friction coefficients minimize the tensile stresses in the contact regions, making it possible to use higher interlocking angles without fracturing the tabs, which in turn generate high stiffness and strength. Interestingly, the optimization results show that the maximum stiffness (Fig. 3.9a), strength (Fig. 3.9b) and extension (Fig. 3.9c) are actually achieved for f =0 and high interlocking angle (θ_0 ~13° for σ_s/E=1/100). This result does not however apply to energy dissipation because friction at the interfaces is the only dissipative mechanism in the system. Zero friction f =0 leads to U=0, which is undesirable for the toughness of the suture.

The trend in terms of energy is more complex and displays an optimum coefficient of friction which is function of the ratio σ_s/E only. The models give an optimum friction coefficient for energy absorption of $f = 0.080$ for σ_s/E=1/100 and $f = 0.018$ for σ_s/E=1/1000. These friction coefficients are relatively small, but again for these optimized cases the frictional energy dissipated at the interface can be magnified by high locking angles.

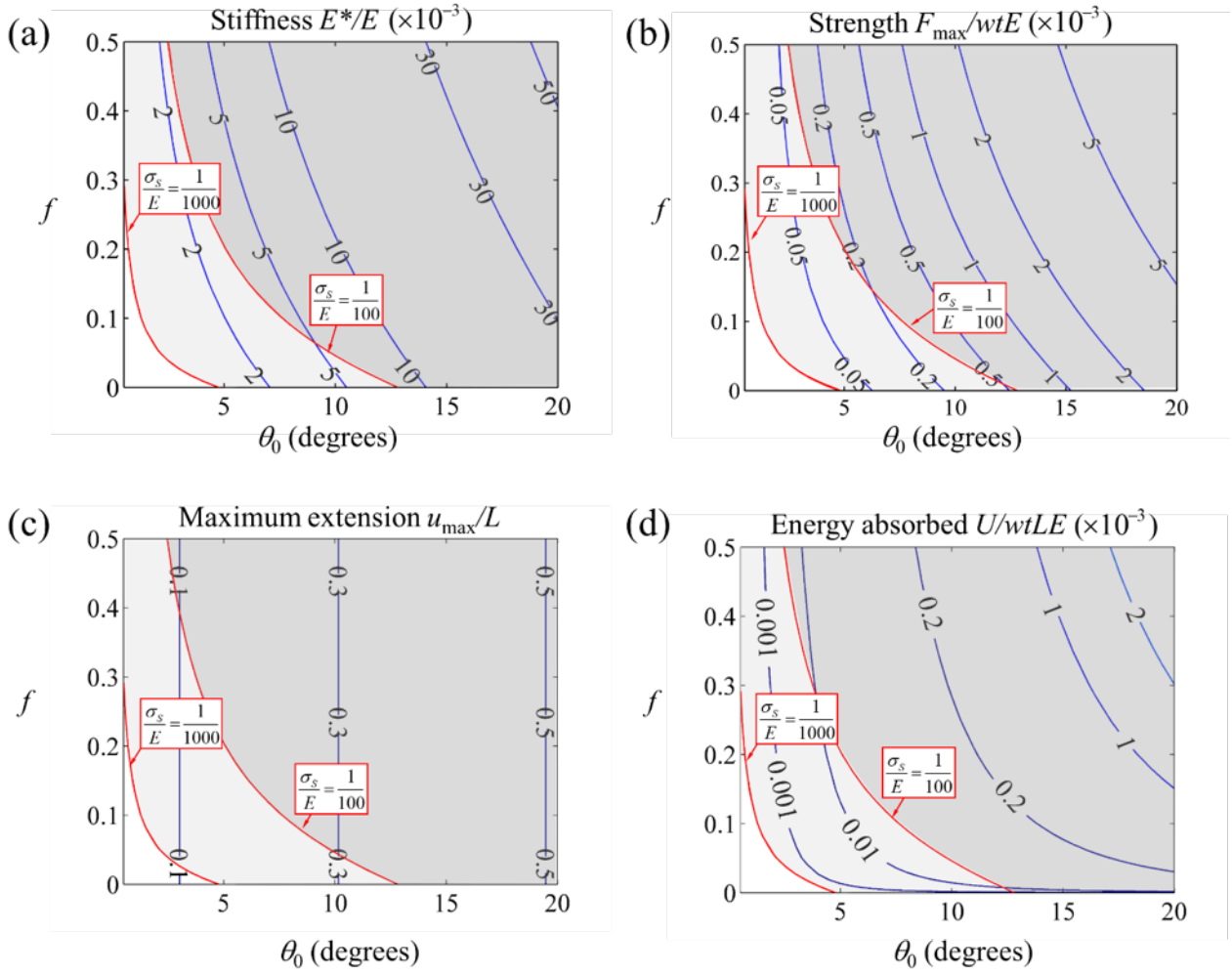

Figure 3.8: Mechanical properties of the jigsaw suture as function of interlocking angle θ_0 and friction coefficient f. The properties are plotted as blue contour lines on each of the diagrams. (a) stiffness; (b) strength; (c) maximum extension and (d) energy absorbed. In each case the red lines show limit designs for which the tensile strength of the material is reached (σ_s/E=1/100 and σ_s/E=1/1000).

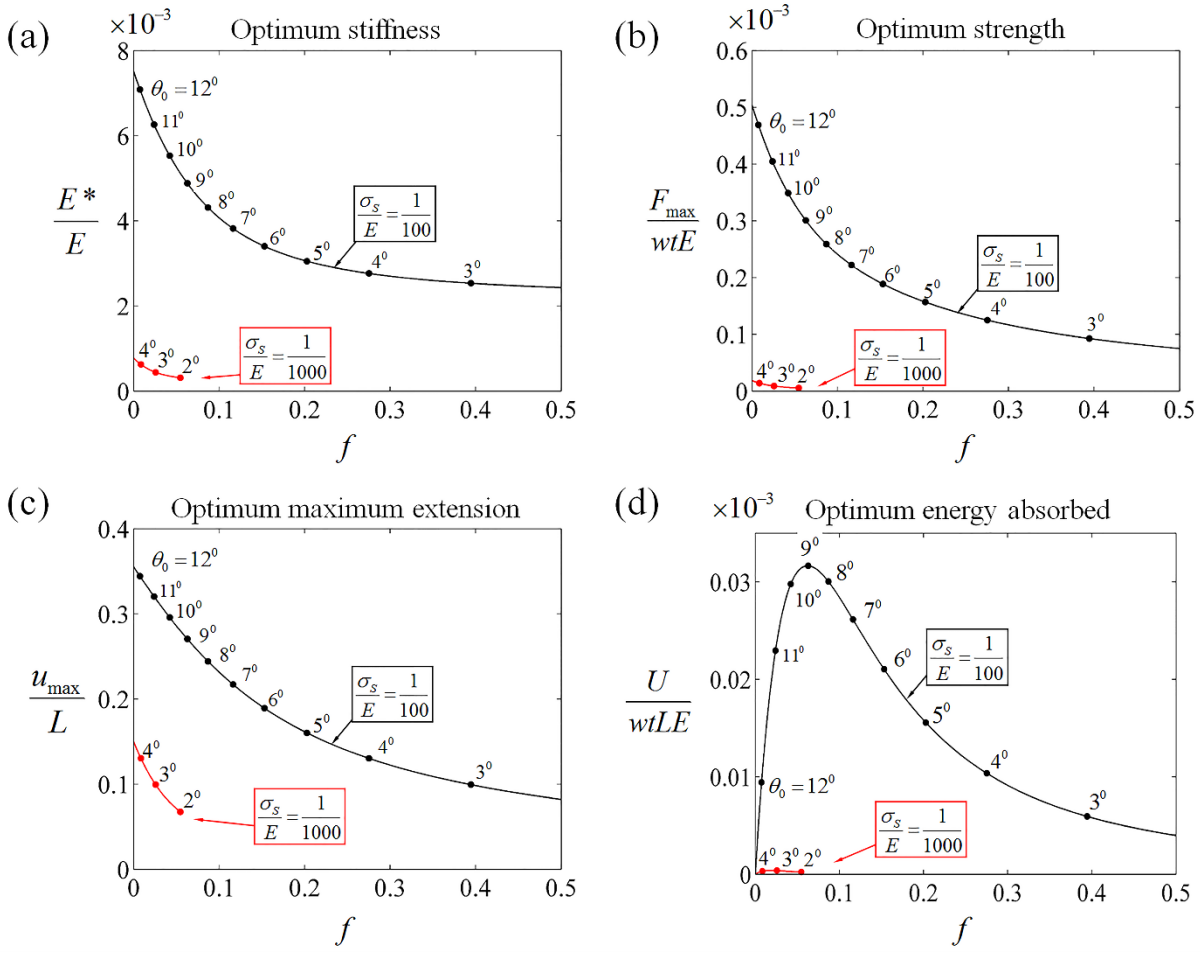

Figure 3.9: Optimum parameters and mechanical properties for the limiting tensile strength of the bulk material for σ_s/E=1/100 and σ_s/E=1/1000: (a) optimum stiffness; (b) optimum strength; (c) optimum maximum extension and (d) optimum energy absorbed.

3.6 3D printing and mechanical testing

In order to validate the pullout models and to explore the optimum designs suggested above, we fabricated and tested jigsaw like interlocked sutures using 3D printing and miniaturized mechanical testing. The solid material was Acrylonitrile Butadiene Styrene (ABS) (EnvisionTech Perfactory, MI, US). A high resolution 3D printer (Micro HiRes Machine, EnvisionTech) based on the digital light processing (DLP) technology [43, 44] was used for fabrication. This particular 3D printer produces fully dense, isotropic solid components with a high level of geometrical fidelity and very smooth surfaces. We measured the mechanical properties of the as-printed ABS material using a three-point bending configuration (N=3),

and found a modulus E= 1.7±0.2 GPa, and a strength σ_S=118±12 MPa (failure was brittle). We verified that the material is isotropic by performing the same measurement along three different orientations with respect to the direction of printing. We also measured the kinetic coefficient of friction of ABS on ABS using ASTM D1894 [45], revealing a coefficient of friction f = 0.35 ± 0.04 (N=3) for this material. Jigsaw-like sutures consisting of a single tab with different interlocking angles θ_0 = 5°, 10°, 15°, 20°, with R =1 mm and thickness t =2 mm (Figure 3.10a) were 3D printed. The printing direction was along the out-of-plane direction for the tabs (axis z on Figure 3.10a) and the layer thickness was 50 µm. In order to prevent any gaps at the interface of the suture, the two solid parts of the sample were printed individually, and then assembled by sliding along the out-of-plane direction (Figure 3.10b, c). Two holes were made in the samples to apply the pull-out force (Figure 3.10a) through loading pins. Each sample contained a single interlocking tab, and in order to prevent lateral bending and transverse strains during pullout (which would not be representative of a periodic suture), the total width of the sample was set to about five times the width of the tab. Pictures of actual samples with three different interlocking angles are shown on Figure 3.10c. The tests were performed at a pulling rate of 0.05 mm/s and with optical imaging to measure displacements. The pullout force F was divided by the cross section wt to obtain the average stress applied onto the interlocking tab, and the pullout displacement u was normalized by the length of the locking tab L. Three samples were tested for each geometry (N=3) for repeatability. Figure 3.11a shows the representative pullout behavior of the suture for each of the four interlocking angles. The bell shape of the curves is similar to the theoretical predictions and has the characteristics of a progressive failure [41]. The stiffness, strength, maximum elongation and energy absorption all increased with interlocking angle as predicted by the models. Sutures with interlocking angle of 20° fractured prematurely, with cracks emanating from the edges of the contact region (Figure 3.11a), also in agreement with the

stress analysis presented above. We compared the experimental pullout response for interlocking angles θ_0 = 5°, 10°, 15°, 20° with the prediction of the models using the values E =1.72 GPa and f =0.35 measured experimentally for ABS. Experiments and models agreed well, figure 3.11b showing a representative comparison obtained for the case θ_0 =10°. Figures 3.11c-e summarize the experimental properties of the suture and show how the stiffness, strength and energy absorption increase with θ_0, up to θ_0 =15°. The model could capture the experimental values for each property over one order of magnitude. On a logarithmic scales with a reference of 0.001 for the lower bound, the difference between model and experiment was only 0.3-7% (Figure. 3.11c-e). On a linear scale the difference is larger and in the 5-25% range. The model could therefore capture the experimental values relatively well for all properties. The tabs fractured at an interlocking angle of 20°, which can also be compared with our models using E =1.72 GPa, f =0.35, Poisson's ratio ν=0.4 (typical value for rigid polymers [46]), and σ_s =118 MPa corresponding to $\frac{\sigma_S}{E} \approx 0.07$. Using these values, our model predicted that the tab would fracture for locking angles θ_0 > 14.66°. In the experiments the tabs were intact for θ_0 =15° but fractured for θ_0 =20° the model therefore only slightly underestimated the strength of the tab. We did not observe permanent, plastic deformations in the tabs, which is consistent with a yielding model based Johnson and Jefferiss [37] for frictional contact problems. Using Von-Mises yield criteria, the model predicts an onset of yielding at a maximum contact pressure of $(p_0)_y = 0.8\sqrt{3}\sigma_y$ for a friction coefficient of f =0.35. With a 0.2% offset yield strength of ABS of σ_y =109.8±8.7 MPa measured experimentally, the model predicts an onset of yielding at $(p_0)_y$ =152.2 MPa. The maximum contact pressure for the two identical disks is given by [37]:

$$p_0 = \frac{2P}{\pi t a} \tag{3.24}$$

The maximum force P occurs at the maximum interference between the tabs given by:

$$\delta_{\max} = 2R(1-\cos\theta_0) \tag{3.25}$$

By solving equations 3.11, 3.12, 3.24 and 3.25 numerically, we determined that the tabs start to yield at interlocking angle $\theta_0 = 16.6°$ which is more than the interlocking angle $\theta_0 = 14.7°$ at which the tabs fracture in a brittle fashion. The implication is that the state of the stresses within the tabs is such that the tabs break before they yield. This prediction agrees with the experiments: the tabs fail catastrophically with little or no plastic deformation.

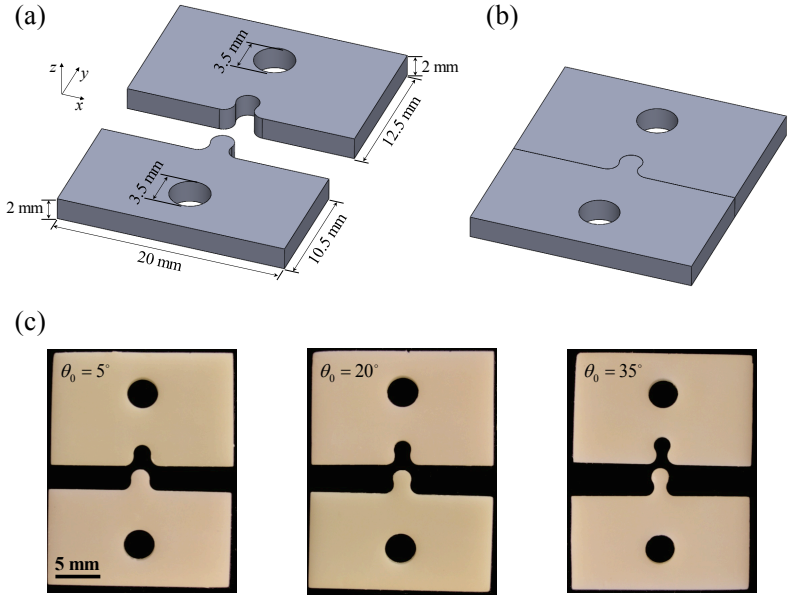

Figure 3.10: 3D printed suture samples: Diagrams showing (a) the shape and dimensions of the two parts of the samples and (b) the assembled sample; (c) Pictures of Samples with different interlocking angles, before assembly.

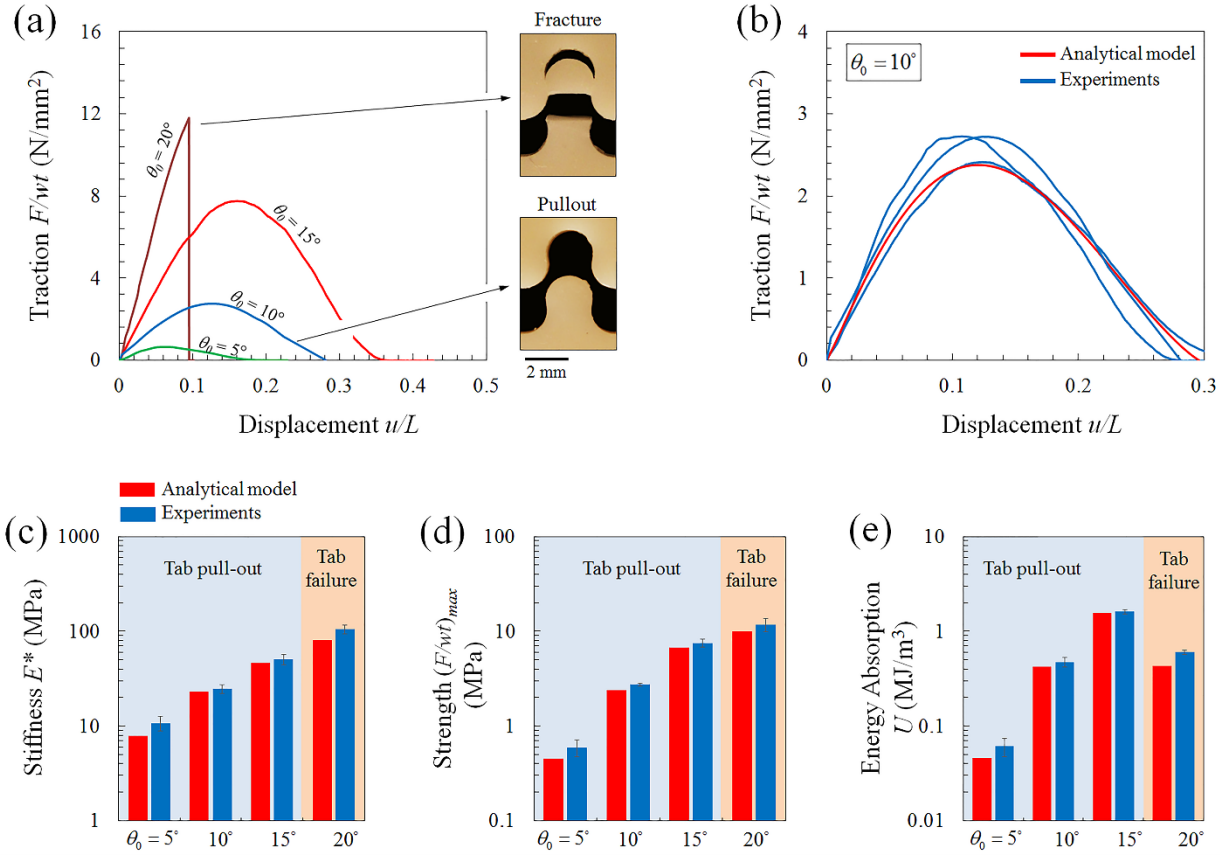

Figure 3.11: Experiments on the jigsaw interlocked tabs. (a) Representative pullout curves with different interlocking angles (θ_0 = 5°, 10°, 15°, 20°), with representative pictures showing two different failure modes: tab pullout and fracture. (b) Comparison between simulation and experimental pullout curves for sutures with θ_0 = 10°. (c) Stiffness, (d) strength, and (e) energy absorption of the suture as a function of interlocking angle, with comparisons from models (the error bars represent ± one standard deviation of the variable).

The models and optimization presented in the previous sections suggest that lower coefficient of friction at the interface would increase the overall properties of the optimized tab, a seemingly counter intuitive result we wanted to verify experimentally. We reduced the coefficient of friction by using paraffin as lubricant [47] and measured f = 0.142 ± 0.021 using a standard friction test [45]. This value of friction coefficient is about 2.5 times lower than the dry case. We fabricated a new batch of sutured materials with locking angles of θ_0 = 10°, 20°, 30°, 35°, and 40°. Prior to assembly of the samples, a thin coating of paraffin was applied on the inner surfaces of the tabs. A set of representative experimental pullout curves are shown on Figure 3.12a. With a reduced friction, the interlocking angle could be increased to θ_0 = 35° without breaking the tabs, as predicted by the model. However the model could

not match the experimental curves, which we attributed to the extensive plastic deformations in the tabs (these limitations of our models would not apply when designing sutures in ceramics or glasses). Nevertheless, the experimental results (Figure 3.12b,c,d) confirmed that significantly higher stiffness, strength and energy absorption can be achieved at higher interlocking angles with a lower coefficient of friction. The stiffness, strength and energy absorption of the lubricated suture with the optimum interlocking angle of $\theta_0 = 35°$, were 2.5, 2 and 2.7 times higher than the highest stiffness, strength and energy absorption achieved with the non-lubricated samples (at $\theta_0 = 15°$).

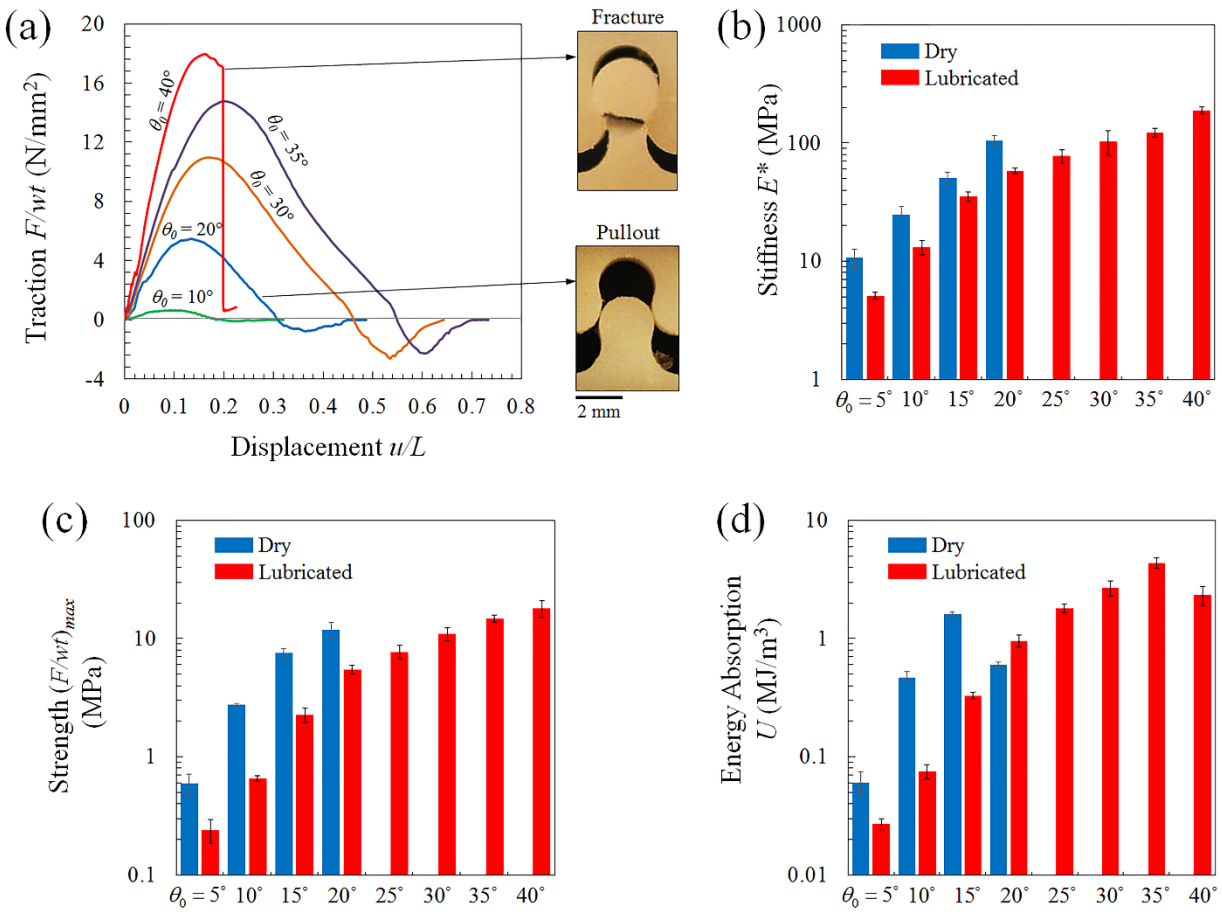

Figure 3.12: Experimental results from sutures with reduced friction coefficient: (a) Representative pullout behavior of the lubricated tab with different interlocking angles (θ_0 = 10°, 20°, 30°, 35°, 40°) with pictures showing two different failure modes. (b) Stiffness, (c) strength, and (d) energy absorption of the lubricated suture as functions of interlocking angle. Comparison between dry and lubricated cases is also shown (the error bars represent ±one standard deviation of the variable).

A potential application of the jigsaw-like suture is to exploit its energy absorption and toughness, as seen in recent examples of all-brittle architectured materials that combine surface hardness with deformability, energy absorption and impact resistance [34, 35, 48]. Here we calculated the effective toughness of the sutured interface with the toughness of ABS. The fracture toughness of plain ABS was measured using a 3-point-bending fracture test configuration [49] and was found to be J_S =300±28.6 J.m^{-2}. By interpreting the pullout data as a traction separation law which would govern the mode I fracture of the suture, the effective toughness of the suture is simply the area under the experimental traction (F/wt) separation (u) curve. Using this method we measured a toughness J=13.76±1.7 kJ.m^{-2} for the optimum suture (θ_0 = 35°, lubricated), which is about 45 higher than plain ABS. Incorporating sutures is therefore a powerful method to increase the effective toughness of materials and structures.

3.7 Summary

Sutured materials are prominent in natural materials and they are now attracting an increasing amount of attention in the context of bio-inspired engineering applications. The strength and fracture mechanics of these sutures were characterized in the past for sinusoidal morphologies [29, 30], or more complex interlocking morphologies but only at small strains [21, 32, 33]. In this work we proposed, for the first time, a model that captures the complete pullout of jigsaw-like features over long distances, with progressive interlocking and frictional interactions at the interfaces. The model also provides the maximum tensile stress in the solid parts of the tabs, which can be used to predict and prevent the brittle fracture of the tabs. The main conclusions from the models are as follow:

- The resistance to pull-out of the suture increases with angle θ_0 and friction coefficient f.
- The highest tensile stresses in the solid are generated by frictional tractions at the contact between the tabs, and occur at the edge of the contact area. These stresses are always significantly larger than the tensile stresses occurring in the smallest cross section of the tabs.
- The design guidelines we present here are useful for non-adhesive contact of jigsaw-like sutures in any brittle material subjected to tensile loading.
- Optimization revealed that to maximize stiffness, strength and energy absorption it is preferable to use low coefficients of friction to minimize the stresses near the frictional contact, combined with high interlocking angles to generate high structural properties for the suture.

We validated the models and these observations by 3D printing and testing actual jigsaw interlocked tabs made of ABS, a relatively brittle polymer. Good agreements between the predicted and actual pullout curves were obtained for different interlocking angles. The models also predicted the failure of tabs with a good accuracy, in terms of both the interlocking angle at which the tabs start to break and the location of the failure (trailing edge of the contact). We finally verified experimentally by lubricating the interfaces that designs with low coefficients of friction and high interlocking angles lead to higher properties overall, including higher energy dissipation. The suture interface is particularly remarkable for its toughness: we found that it is 45 times tougher than plain ABS (in J-terms). These models and optimization results therefore provide a robust platform for the design and optimization of jigsaw-like sutures, which can be exploited in compliant interfaces [12, 21], in morphologically enhanced bond lines [25], and in damping and shock absorbing applications [22]. Dense network of sutures in materials can lead to unusual and attractive homogenized

performance that can surpass monolithic materials: enhanced toughness, deformation and energy absorption in otherwise fragile materials [34, 35]. Finally, the models presented here are restricted to simple jigsaw geometries with only two geometrical parameters (curvature and interlocking angle). Enriching the shape of the suture is likely to generate a wider range of properties, for example by generating "double locking" upon pullout [50]. The models developed here can serve as a starting point for the exploration and optimization of these more complex suture morphologies.

3.8 Acknowledgements

This work was supported by Natural Sciences and Engineering Research Council of Canada and by the Fonds de Recherche du Québec – Nature et Technologies. IAM was supported by a Scholarship from the Nigerian Government through the National Universities commission.

3.9 References

1. Koester, K.J., J.W. Ager, III, and R.O. Ritchie, *The true toughness of human cortical bone measured with realistically short cracks.* Nature Materials, 2008. **7**(8): p. 672-677.
2. Currey, J.D., *Bones : structure and mechanics*. 2002, Princeton, NJ: Princeton University Press.
3. Bajaj, D., et al., *Fracture Processes and Mechanisms of Crack Growth Resistance in Human Enamel.* Jom, 2010. **62**(7): p. 76-82.

4. Barthelat, F., et al., *On the mechanics of mother-of-pearl: A key feature in the material hierarchical structure.* Journal of the Mechanics and Physics of Solids, 2007. **55**(2): p. 306-337.

5. Chen, I.H., W. Yang, and M.A. Meyers, *Leatherback sea turtle shell: A tough and flexible biological design.* Acta Biomaterialia, 2015. **28**: p. 2-12.

6. Ritchie, R.O., *The conflicts between strength and toughness.* Nature Materials, 2011. **10**(11): p. 817-822.

7. Barthelat, F., *Architectured materials in engineering and biology: fabrication, structure, mechanics and performance.* International Materials Reviews, 2015. **60**(8): p. 413-430.

8. Barthelat, F., Z. Yin, and M.J. Buehler, *Structure and mechanics of interfaces in biological materials.* Nature Reviews Materials, 2016. **1**: p. 16007.

9. He, M.Y., A.G. Evans, and J.W. Hutchinson, *Crack deflection at an interface between dissimilar elastic materials: Role of residual stresses.* International Journal of Solids and Structures, 1994. **31**(24): p. 3443-3455.

10. Khayer Dastjerdi, A., R. Rabiei, and F. Barthelat, *The weak interfaces within tough natural composites: Experiments on three types of nacre.* Journal of the Mechanical Behavior of Biomedical Materials, 2013. **19**: p. 50-60.

11. Smith, B.L., et al., *Molecular mechanistic origin of the toughness of natural adhesives, fibres and composites.* Nature, 1999. **399**(6738): p. 761-763.

12. Dunlop, J.W.C., R. Weinkamer, and P. Fratzl, *Artful interfaces within biological materials.* Materials Today, 2011. **14**(3): p. 70-78.

13. Fratzl, P., I. Burgert, and H.S. Gupta, *On the role of interface polymers for the mechanics of natural polymeric composites.* Physical Chemistry Chemical Physics, 2004. **6**(24): p. 5575-5579.

14. Fratzl, P., et al., *The mechanics of tessellations–bioinspired strategies for fracture resistance.* Chemical Society Reviews, 2016. **45**(2): p. 252-267.

15. Meyers, M.A., et al., *Biological materials: Structure and mechanical properties.* Progress in Materials Science, 2008. **53**(1): p. 1-206.

16. Lee, N., et al., *Hierarchical multiscale structure-property relationships of the red-bellied woodpecker (Melanerpes carolinus) beak.* Journal of the Royal Society Interface, 2014. **11**(96).

17. Lin, E., et al., *3D printed, bio-inspired prototypes and analytical models for structured suture interfaces with geometrically-tuned deformation and failure behavior.* Journal of the Mechanics and Physics of Solids, 2014. **73**: p. 166-182.

18. Song, J., et al., *Quantitative microstructural studies of the armor of the marine threespine stickleback (Gasterosteus aculeatus).* Journal of structural biology, 2010. **171**(3): p. 318-331.

19. Miura, T., et al., *Mechanism of skull suture maintenance and interdigitation.* Journal of anatomy, 2009. **215**(6): p. 642-655.

20. Moazen, M., et al., *Assessment of the role of sutures in a lizard skull: a computer modelling study.* Proceedings of the Royal Society B-Biological Sciences, 2009. **276**(1654): p. 39-46.

21. Achrai, B., B. Bar-On, and H.D. Wagner, *Bending mechanics of the red-eared slider turtle carapace.* Journal of the mechanical behavior of biomedical materials, 2014. **30**: p. 223-233.

22. Saunders, W.B., D.M. Work, and S.V. Nikolaeva, *Evolution of complexity in paleozoic ammonoid sutures.* Science, 1999. **286**(5440): p. 760-763.

23. Allen, E.G., *Understanding ammonoid sutures: New insight into the dynamic evolution of Paleozoic suture morphology*. Cephalopods Present and Past: New

Insights and Fresh Perspectives, ed. N.H. Landman, R.A. Davis, and R.H. Mapes. 2007. 159-180.

24. Maloul, A., et al., *Characterization of craniofacial sutures using the finite element method.* Journal of Biomechanics. **47**(1): p. 245-252.

25. Miura, T., et al., *Mechanism of skull suture maintenance and interdigitation.* Journal of Anatomy, 2009. **215**(6): p. 642-655.

26. Genkal, S.I. and G.I. Popovskaya, *Centric diatom algae of the Selenga River and its delta branches.* Inland Water Biology, 2008. **1**(2): p. 120-128.

27. Manoylov, K.M., N. Ognjanova-Rumenova, and R.J. Stevenson, *Morphotype variations in subfossil diatom species of Aulacoseira in 24 Michigan Lakes, USA.* Acta Botanica Croatica, 2009. **68**(2): p. 401-419.

28. Lin, E., et al., *Tunability and enhancement of mechanical behavior with additively manufactured bio-inspired hierarchical suture interfaces.* Journal of Materials Research, 2014. **29**(17): p. 1867-1875.

29. Zavattieri, P.D., L.G. Hector, Jr., and A.F. Bower, *Cohesive zone simulations of crack growth along a rough interface between two elastic-plastic solids.* Engineering Fracture Mechanics, 2008. **75**(15): p. 4309-4332.

30. Cordisco, F.A., et al., *Mode I fracture along adhesively bonded sinusoidal interfaces.* International Journal of Solids and Structures, 2016. **83**: p. 45-64.

31. Srivastava, A., S. Osovski, and A. Needleman, *Engineering the crack path by controlling the microstructure.* Journal of the Mechanics and Physics of Solids, 2017. **100**: p. 1-20.

32. Li, Y., C. Ortiz, and M.C. Boyce, *Bioinspired, mechanical, deterministic fractal model for hierarchical suture joints.* Physical Review E, 2012. **85**(3).

33. Li, Y., C. Ortiz, and M.C. Boyce, *A generalized mechanical model for suture interfaces of arbitrary geometry.* Journal of the Mechanics and Physics of Solids, 2013. **61**(4): p. 1144-1167.

34. Mirkhalaf, M., A.K. Dastjerdi, and F. Barthelat, *Overcoming the brittleness of glass through bio-inspiration and micro-architecture.* Nature communications, 2014. **5**: p. 3166.

35. Malik, I.A. and F. Barthelat, *Toughening of thin ceramic plates using bioinspired surface patterns.* International Journal of Solids and Structures, 2016.

36. Cray, J., M.P. Mooney, and M.I. Siegel, *Timing of ectocranial suture activity in Pan troglodytes as related to cranial volume and dental eruption.* The Anatomical Record, 2010. **293**(8): p. 1289-1296.

37. Johnson, K.L. and K.L. Johnson, *Contact Mechanics*. 1987: Cambridge University Press.

38. Ciavarella, M. and P. Decuzzi, *The state of stress induced by the plane frictionless cylindrical contact. I. The case of elastic similarity.* International Journal of Solids and Structures, 2001. **38**(26–27): p. 4507-4523.

39. Persson, A., *On the Stress Distribution of Cylindrical Elastic Bodies in Contact*. 1964: inst.

40. ANSYS, *ANSYS® Academic Research, Release 15.0.* 2013.

41. Barthelat, F. and M. Mirkhalaf, *The quest for stiff, strong and tough hybrid materials: an exhaustive exploration.* Journal of The Royal Society Interface, 2013. **10**(89): p. 20130711.

42. Ashby, M.F., *Chapter 4 - Material Property Charts*, in *Materials Selection in Mechanical Design (Fourth Edition)*. 2011, Butterworth-Heinemann: Oxford. p. 57-96.

43. Studart, A.R., *Additive manufacturing of biologically-inspired materials.* Chemical Society Reviews, 2016. **45**(2): p. 359-376.

44. Tumbleston, J.R., et al., *Continuous liquid interface production of 3D objects.* Science, 2015. **347**(6228): p. 1349-1352.

45. American Society for Testing and Materials, *Standard Test Method for Static and Kinetic Coefficients of Friction of Plastic Film and Sheeting.* 1894.

46. Tschoegl, N.W., W.G. Knauss, and I. Emri, *Poisson's ratio in linear viscoelasticity–a critical review.* Mechanics of Time-Dependent Materials, 2002. **6**(1): p. 3-51.

47. Jia, B.-B., et al., *Tribological behaviors of several polymer–polymer sliding combinations under dry friction and oil-lubricated conditions.* Wear, 2007. **262**(11): p. 1353-1359.

48. Mirkhalaf, M., J. Tanguay, and F. Barthelat, *Carving 3D architectures within glass: Exploring new strategies to transform the mechanics and performance of materials.* Extreme Mechanics Letters, 2016. **7**: p. 104-113.

49. Standard, A., *Standard test method for measurement of fracture toughness.* ASTM, E1820-01, 2001: p. 1-46.

50. Mirkhalaf, M. and F. Barthelat, *Design, 3D printing and testing of architectured materials with bistable interlocks.* Extreme Mechanics Letters, 2017. **11**: p. 1-7.

Link between chapter 3 and chapter 4

In the previous chapter, we developed analytical and finite element models using linear elasticity and non-Hertzian contact mechanics, which we then used to explore the effect of interlocking angle θ_0 and friction coefficient f on the pullout response and maximum stress in jigsaw-like interlocking sutures. We reported good agreement between the analytical and finite element models, and then we performed an exhaustive search optimization. The optimization results show that the best mechanical properties are achieved with low friction coefficient f and high interlocking angle θ_0. This result was validated by fabricating and testing a set of 3D printed interlocking sutures with ABS as the base material. The model is a guideline for the design, optimization and fabrication of jigsaw-like sutures pulled in tension with no adhesive at the interface. In addition the models show that the mechanical properties of sutures can be tuned with the geometrical parameters, and we therefore extended the model to incorporate other geometrical parameters in order to have a broader view of effect of geometry on mechanical properties. In the next chapter, we used the same underlying assumptions to develop analytical and finite element models. In this case, the sutures were systematically created using some geometrical parameters called shape descriptors. The selected shape descriptors we used are local suture angle(s) ϕ, (interlocking angle θ_0 and transition angle(s) θ_1), radius of curvature R_0/R_1, and plateau length d/R_0. The results show that all the geometrical parameters have positive effect on the pullout response and maximum stress. We then perform an exhaustive search optimization which shows that: (i) for each of the suture families, the geometry that gives optimum performance is the one with low friction coefficient f, and high interlocking angle θ_0, and (ii) multilocking geometry with locking along the pulling direction is the most potent design. This chapter was accepted for publication in the *International Journal of solids and structures*.

Chapter 4

Bioinspired sutured materials for strength and toughness: Pullout mechanisms and geometric enrichments

Chapter 4: Bioinspired sutured materials for strength and toughness: Pullout mechanisms and geometric enrichments

Idris. A. Malik and Francois Barthelat*

Department of Mechanical Engineering, McGill University, 817 Sherbrooke Street West, Montreal, QC H3A 2K6, Canada

Submitted for publication to the International Journal of solids and structures

4.1 Abstract

Hard structural elements in nature are often joined with sutures lines, as seen in human skull, cephalopods or turtle shell. These sutures can arrest cracks, and can provide flexibility for respiration, locomotion or growth. In this paper we introduce a morphometric method to capture the complex shape of sutured interfaces using only a few parameters. The method is simple, and can capture relatively complex suture geometries with re-entrants interlocking features. The study starts with a simple jigsaw-like model which is enriched with additional features (plateau regions in dovetail-like sutures, multiple locking sites). For each case, closed form and finite elements solutions are developed to capture the full nonlinear pullout response and to predict the maximum stress (and potential fracture) in the solid material. These models were then used to identify the geometries and interface properties (friction) that lead to optimum combinations of strength and energy absorption. Suture designs that reduced frictional stress with low coefficient of friction or with multiple contact points were the most efficient. The results can serve as guidelines to design and optimization of non-adhesive sutures with arbitrary shapes made of arc of circles and lines. We found that the best designs involve low coefficient of friction, which raises an interesting hypothesis on the function of the protein layer in natural sutured lines: This soft layer could act as "lubricant" to prevent the fracture of the solid structures.

Keywords: Sutured lines, shape descriptors, analytical models, finite element models, optimization

4.2 Introduction

Components made of hard materials can be joined by suture lines, a structural feature found in multiple examples in nature: shells of cephalopods [1], human skull [2-4], carapace of turtle [5-7], wood peckers beak [8] (Figure 4.1), and in many other hard biological materials where weak interfaces govern deformation and fracture mechanisms [9, 10]. In these examples, stiff skeletal material (mineralized proteinaceous matrices, keratin) are joined by a thin lines of interfacial material which are much softer. The geometrical complexity of the suture lines ranges from nearly straight sutured interfaces in new born baby skull [2, 4], to more complex ceratitic and ammonitic sutures with fractals geometries [1, 11, 12]. In cephalopods such as ammonoid, which produce angular or dendritic sutures, the complexity of the suture lines varies across species [1], or with growth as seen in the interdigitating suture lines in human skull which become more complicated from infant to adult [4, 13]. Some of these interfaces form anti-trapezoidal sutures which are interlocked as seen in linking the girdles of diatoms [14, 15], while others display sinusoidal interfaces which increases resistance to crack propagation [16].

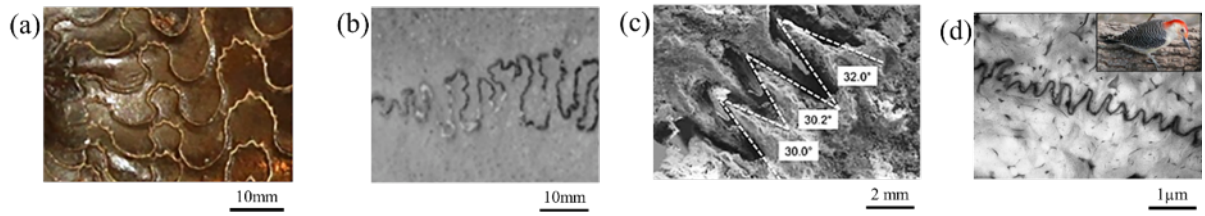

Figure 4.1: Examples of sutured interfaces in nature: (a) Ammonite shell (*Ceratitic ammonoid*) with intricate suture lines [12], (b) Pan troglodytes cranial sutures (adapted from [28]), (c) Osteoderms of a leatherback sea turtle shell (adapted from [6]), (d) red-bellied woodpecker (*Melanerpes carolinus*) beak (adapted from [8]).

The softer interface materials at the sutures enable the relative displacement and/or relative rotation of harder structural components, which facilitates locomotion, respiration or growth

[12, 16]. Sutured interfaces can also absorb impact energy [8], channel the propagation of cracks into toughening configurations, or act as a source of local deformation that can spread energy dissipative mechanisms throughout large volumes [17-19]. The geometry of sutured lines largely governs their mechanical response [11, 12, 21-23]. In particular, interlocking geometrical features can increase strength and energy dissipation [24-27]. We recently developed analytical and finite element models that capture the complete nonlinear pullout response of sutures with simple interlocking jigsaw-like geometries, based on frictional contact and linear elasticity [20]. These models demonstrated how geometry and local friction coefficient govern stiffness, strength and energy absorption, and how geometry and friction can be tuned to optimize the mechanical response. In this article we present new extensions to these models, where we consider sutures with more complex morphologies: dovetail-like sutures and sutures with two or more pairs of locking sites. For each type of suture we performed an exhaustive search to determine the design parameters which maximize strength and energy absorption. A comparative study of the different suture morphologies is provided at the end of the discussion.

4.3 Overview of the suture geometry

Capturing the two-dimensional geometry of a curved suture line requires robust, high fidelity yet relatively simple mathematical models. Methods used in the past include descriptive methods, pattern-matching using geographic information systems, complexity indices, and morphometric methods [1, 15, 29]. In this work, we used a simple 2D shape descriptor approach similar to the morphometric method. Shape descriptors are mathematical objects which can capture geometrical features in a simplified and condensed fashion, for example the radius of a circle, the surface of an area, or geometrical eccentricity [35, 36]. The shape descriptor we used in this study is based on a cumulative angular function of the contour of the suture ϕ as function of the curvilinear position s along the contour (Figure 4.2). The

approach is versatile and more importantly, it enables the modelling of suture lines with re-entrant, interlocking features. For this study we only considered ϕ (s) functions that are multilinear (Figure 4.2a). The 2D profile of the suture can be reconstructed from the ϕ (s) function in the x-y coordinate system using:

$$\begin{cases} x(s) = \int_0^s \cos(\phi(s))ds \\ y(s) = \int_0^s \sin(\phi(s))ds \end{cases}$$

(4.1)

Where the point x=0 and y=0 coincides with s=0. This process generates a periodic unit cell of the suture (figure 2b).

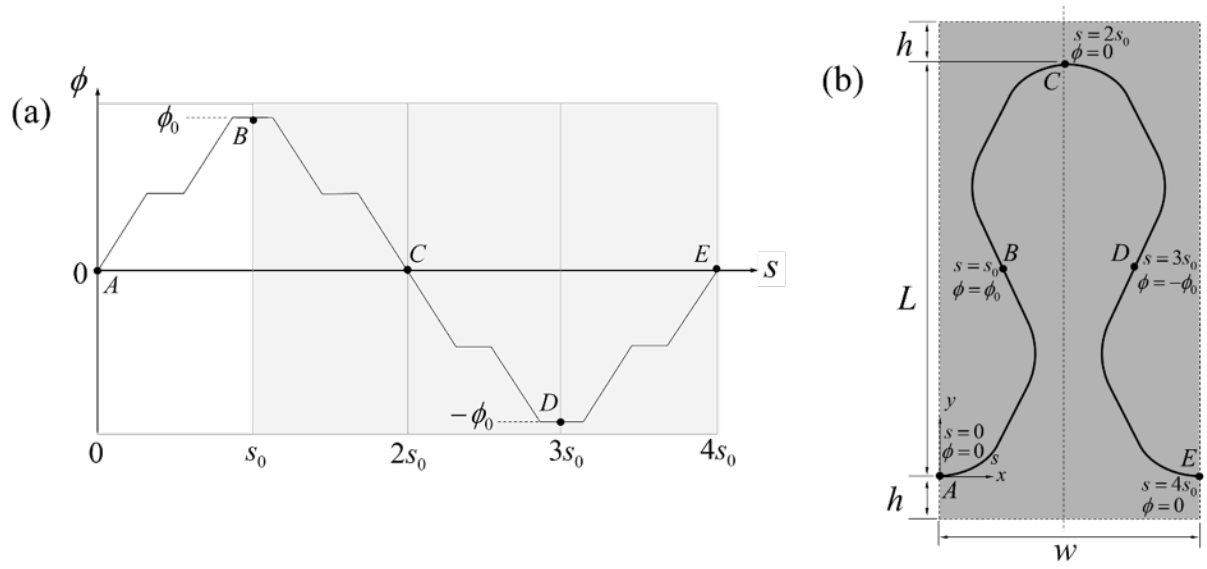

Figure 4.2: (a) A parametric (ϕ-s) curve showing the cumulative angular function as function of curvilinear position; (b) Suture profile in (x,y) reconstructed from the (ϕ-s) function.

For this study we required the contour (x-y) of the suture to be periodic and continuous. We also required contours with no sharp corner or kinks which would generate stress concentrations and lead to sub-optimal designs. The function ϕ (s) therefore had to be continuous. In addition, for a suture line whose general orientation is aligned with the axis x,

the local tangential angle ϕ must take a zero value at least once within the periodic unit cell. For simplicity we chose $\phi(0)=0$. In this work we also only considered sutures with a symmetry about line $x = w/2$, where w is the width of the unit cell in the x-y space. This symmetry implies that the function $\phi(s)$ is antisymmetric about the line $s=2s_0$ (figure 4.2a). Finally, we sought optimum geometries for the suture and therefore we focused on geometries that produce identical stresses on either side of the suture line, because asymmetric suture lines would be sub-optimal with one side inevitably being "better" than the other. Therefore we only considered suture lines with a 180^0 rotational symmetry, which implies that the function $\phi(s)$ is symmetric about the line $s=s_0$ (figure 4.2a). Considering these symmetries, the functions $\phi(s)$ only need to be defined over a quarter of the curvilinear length of the contour in the periodic cell ($0 \le s \le s_0$, Figure 4.2). The first quarter of the (x-y) contour was reconstructed using equation (4.1) up to $s = s_0$, and a 180^0 rotational symmetry was then applied about points $x(s_0), y(s_0)$, in order to produce a half unit cell which was used for the analysis of kinematics, forces and stresses. For display purposes, the full unit cell may be reconstructed with a simple symmetry (figure 4.2b). The full unit cell has width w, and height $L+2h$ where L is the projected length of the suture on the y axis, and h is the height of two regions included in the model on either sides of the suture. The width, w and the height, L of the suture are given by:

$$\begin{cases} w = 2\int_{s=0}^{2s_0} \cos(\phi(s))ds \\ L = \int_{s=0}^{2s_0} \sin(\phi(s))ds \end{cases} \tag{4.2}$$

This "shape generating algorithm" has a few properties that are useful to outline here. The local radius of curvature R on the (x-y) profile of the suture is related to the local suture angle by $Rd\phi = ds$, so that the local slope of $\phi(s)$ is:

$$\frac{d\phi}{ds} = \frac{1}{R} \tag{4.3}$$

An important implication is that horizontal segments in the $\phi(s)$ function ($\phi'(s)$ =0) correspond to straight segments on the (x-y) profile ($R = \infty$). This shape descriptor approach was used to generate a wide array of suture geometries, and the pullout mechanics of each of these geometries was captured with the model described below.

4.4 Pullout models

In terms of mechanics, this study focused on the full pullout response of the suture along the y direction (figure 4.3). We only considered sutures with no adhesive at the interfaces, so that the pullout response was governed only by contact mechanics, friction and geometric interlocking. The solid part of the suture was assumed to be isotropic and linear elastic (modulus E and Poisson's ratio ν), and 2D plane stress conditions were used. Figure 4.3a shows a representative volume element (RVE) of the suture geometry. The pullout was simulated using a displacement controlled boundary conditions:

$$\begin{cases} u_y(x,-h) = 0 \\ u_y(x,L+h) = u \end{cases} \tag{4.4}$$

Where h is the height of the upper and lower portion from the suture interface (figure 4.2c). The sides of the model were subjected to the periodic boundary conditions:

$$\begin{cases} u_x(w/2,y) - u_x(-w/2,y) = w\bar{\varepsilon}_x \\ u_y(w/2,y) = u_y(-w/2,y) \end{cases} \tag{4.5}$$

Where $\bar{\varepsilon}_x$ is the average strain in the x (transverse) direction. The geometry and loading conditions are symmetric about the y-axis so that:

$$u_x(x,y) = -u_x(-x,y) \tag{4.6}$$

Combining equations (4.5) and (4.6), the periodic boundary conditions are written:

$$\begin{cases} u_x(0,y)=0 \\ u_x\left(w/2,y\right)=\dfrac{w}{2}\bar{\varepsilon}_x \end{cases} \tag{4.7}$$

In cases where h is sufficiently large, the stiffness of the solid regions in the transverse direction is high enough to neglect any deformation in the transverse direction, i.e. $\bar{\varepsilon}_x=0$. Equations (4.7) then become (Figure 4.3a):

$$\begin{cases} u_x(0,y)=0 \\ u_x(w/2,y)=0 \end{cases} \tag{4.8}$$

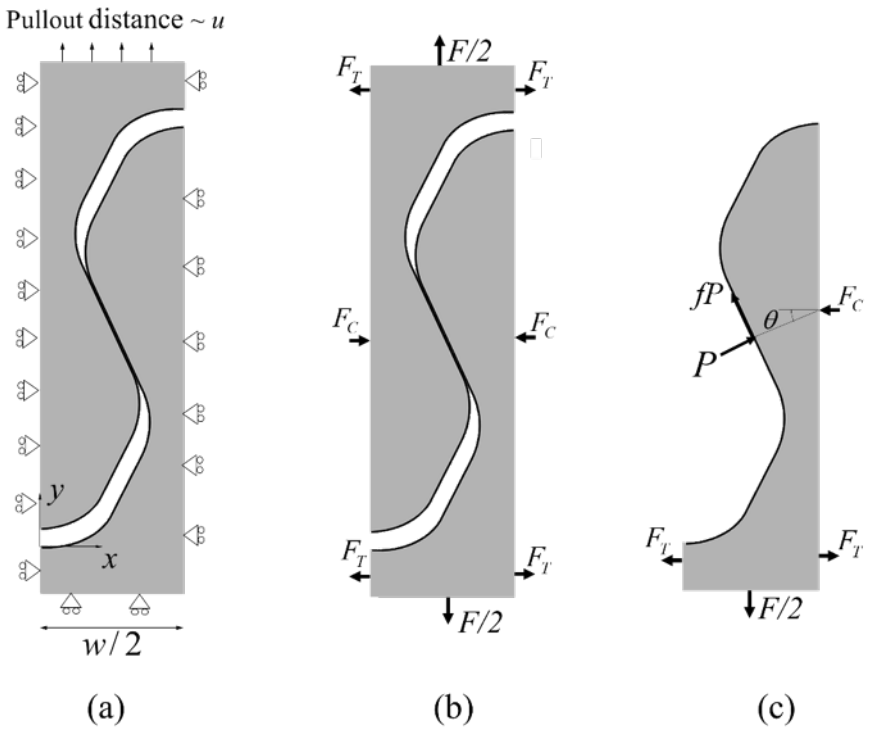

Figure 4.3: (a) Half-unit cell for the suture with symmetry and boundary conditions applied. (b) Free body diagram of the half-unit cell; (c) free body diagram of the lower tab only, exposing the normal and frictional forces transmitted at the contact between the tabs.

When the upper suture is pulled along the y axis, the interlocking at the suture generates a pullout force F along the y axis ($F/2$ on the half unit cell, figure 4.3b). The contact forces at the interfaces also generate a horizontal component, giving rise to a compressive forces F_c

along the x axis. Because the net horizontal force on the unit cell is zero, the compressive forces in the suture region must be balanced by tensile forces F_T transmitted on either sides of the suture line (Figure 4.3b). Figure 4.3c shows a free body diagram of the lower section of the suture, which exposes the contact forces transmitted at the interfaces. These forces can be decomposed into normal force(s) P_i and frictional force(s) fP_i (only one contact force is showed on figure 4.3c, but there might be more sets of contact forces depending on the design of the suture). These contact forces will translate into a pullout force through the equation:

$$F = 2\sum_{i=1}^{N} P_i\left(\sin\theta + f\cos\theta\right) \tag{4.9}$$

The set of forces shown in figure 4.3 also generate stresses in the solid parts of the suture which must be monitored because fracturing the material would abort the pullout mechanisms and cancel their potential benefits. Experiments and stress analysis have shown that for brittle material in sliding dry contact, the highest tensile stresses occur at the surface of the suture, at the edge of the contact area [20]. For each of the geometries presented below, the maximum tensile stress in the solid part was calculated for the entire pullout sequence.

We also used numerical methods for the models, with a combination of finite element simulations (ANSYS parametric design language) interfaced with Matlab (R2016a, MA, US). $\phi(s)$ curves were generated and automatically transformed into suture geometries into x-y profiles using a Matlab. The same code was used to automatically generate APDL input files for ANSYS. The models were meshed with quadratic, plane stress element (PLANE 183), and contact elements (CONTA 172, TARGE 169, symmetric contact) were used to simulate sliding and frictional contact at the interface. To appropriately mesh the model we used an adaptive meshing approach for each geometry. A first model was run with a uniform mesh, and the mesh was automatically refined at the regions of highest stresses. The procedure was

repeated automatically until the results for pullout response and maximum tensile stress in the solid converged, ensuring mesh independent results. Typically the size of the elements in the converged mesh was about $R/5000$ in the contact region, where R is the radius of curvature. The number of time steps in simulation was also adapted automatically to ensure converged results, typically about 500. The results were automatically post-processed using ANSYS ADPL and Matlab. This fully automated exploration procedure enabled the evaluation of thousands of models with different suture geometries and coefficients of friction.

4.5 Exploration of suture geometries

In this section we explore the effect of several suture geometries on pullout behavior. We organized the exploration by starting with a simple design (single jigsaw sutures) based on a single geometrical parameter. We then progressively enriched the geometry of the suture by adding more geometrical features through additional parameters: dovetail-like sutures, double locking sutures, *N*-locking sutures. Within each type of geometry we sought the geometrical parameters and materials properties that lead to optimum combinations of high strength and high energy absorption, while preventing the brittle fracture of the solid part of the suture.

4.5.1 Single jigsaw sutures

The single jigsaw sutures are the simplest form of geometric parameters, with a radius of curvature R_0, and a locking angle θ_0 ([20], Figure 4.4). Since the mechanisms captured here have no specific length scale, all results are normalized by the size of the model, leaving θ_0 the only geometrical parameter. The other geometric parameters can be found using equations (4.2) and (4.4):

$$\begin{cases} \phi_0 = \theta_0 + \pi/2 \\ w = 4R_0 \sin\phi_0 \\ L = 2R_0(1-\cos\phi_0) \end{cases} \tag{4.10}$$

The length of the 1/4 contour of the suture is $s_0 = R_0\phi_0$ and the $\phi(s)$ function is simply (Figure 4.4a):

$$\phi(s) = \frac{s}{R_0}, \quad 0 \le s \le s_0$$

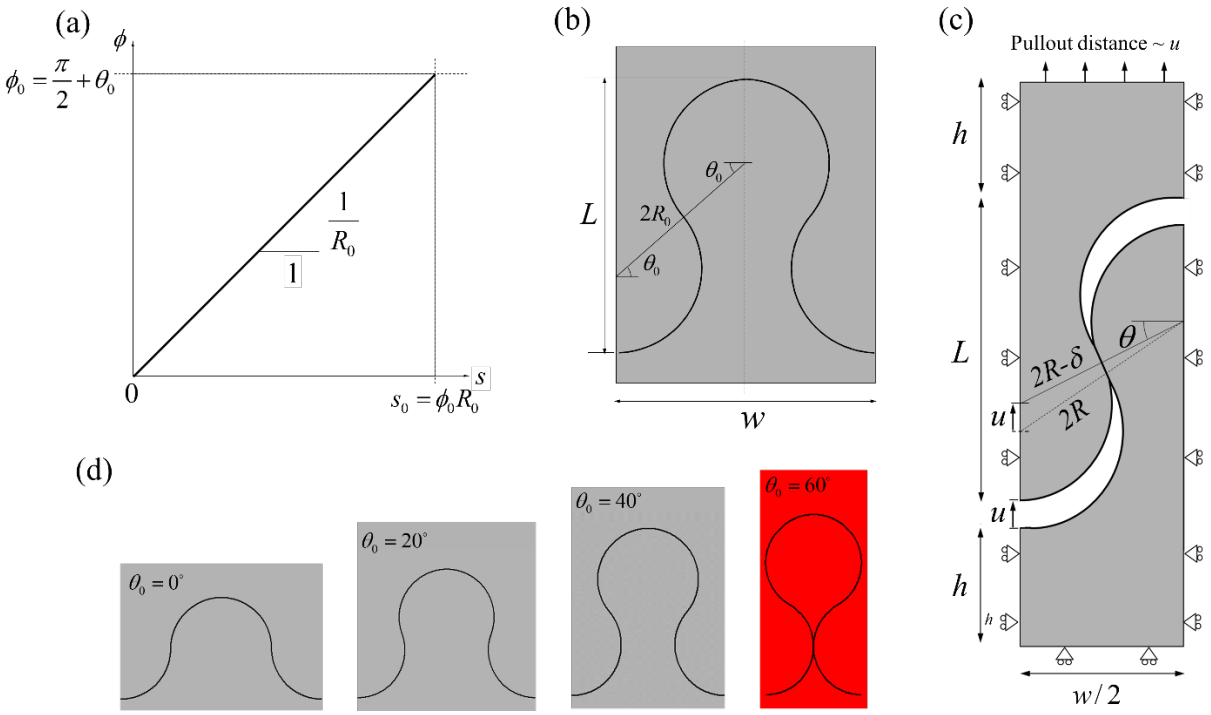

Figure 4.4: (a) (ϕ-s) curve for a one-parameter suture; (b) Corresponding profile; (c) model with symmetry and boundary conditions; (d) The "strength" of the geometrical interlocking is governed by the interlocking angle θ_0, where $\theta_0 < 60°$ to prevent the re-entrant regions of the tabs to intersect (case highlighted in red).

Figure 4.4b shows the reconstructed profile of the suture, which consists of four appended arcs of circle. The level of interlocking increases when θ_0 increases as shown on figure 4.4c, up to the extreme case θ_0 = 60° where the suture line intersects which corresponds to the maximum geometrically allowed locking angle. Sutures with $\theta_0 \geq$ 60° were therefore excluded from the exploration as physically inacceptable. An analytical solution for the

pullout response based on simple kinematics and contact mechanics was presented in a previous article [20], with the main results are summarized below. Figure 4.3b and 4.3c, gives the kinematics relations for [20]:

$$(2R_0 - \delta)\cos\theta = 2R_0 \cos\theta_0 \tag{4.11}$$

$$u = 2R_0 \sin\theta_0 - (2R_0 - \delta)\sin\theta \tag{4.12}$$

Using contact mechanics, the non-dimensional interference is given as:

$$\frac{\delta}{R_0} = \frac{2}{\pi}\frac{P}{R_0 tE}\left[\ln\left(4\pi\frac{R_0 tE}{P}\right) - 1\right] \tag{4.13}$$

Where t is the thickness of the tab. This equation is solved numerically to determine the non-dimensional contact force $\frac{P}{R_0 tE}$ and the non-dimensional pullout force from equation (4.10) is given as:

$$\frac{F}{wtE} = \frac{P}{R_0 tE}\left(\frac{\sin\theta + f\cos\theta}{2\cos\theta_0}\right) \tag{4.14}$$

The effect of Poisson's effects are neglected in this solution, but finite elements confirm that Poisson's ratio has little effects on the solutions.

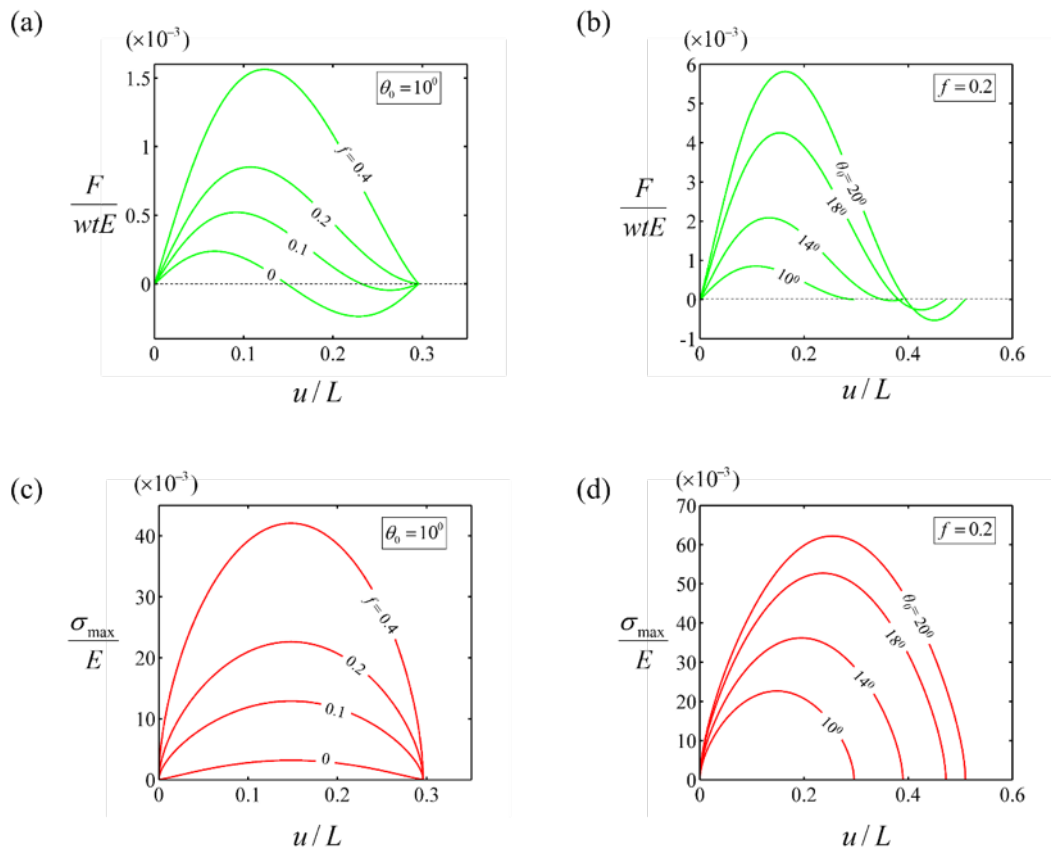

Figure 4.5: Effects of (a) friction f and (b) interlocking angle θ_0 on the pullout response of the suture; effects of (c) friction f and (d) interlocking angle θ_0 on maximum tensile stress in the solid tabs.

Figure 4.5a and 4.5b show the effects of the friction coefficient f, and interlocking angle θ_0 on the pullout response of the suture. High coefficients of friction f lead to relatively high strength because of increased friction at the contact point, but do not change the maximum pullout distance which is governed by geometric parameters. Higher interlocking angles θ_0 increase the strength because of increased geometrical interlocking (figure 4.5b), and also increase the maximum pullout distance because the tabs stay in contact over a longer pullout distance. The friction f and interlocking angle θ_0 have therefore positive effects on strength and energy absorption. However increasing these two parameters also increase frictional stresses, which can lead to the fracture of the tabs. The maximum tensile stress in the suture is divided into frictionless and frictional contact stresses [20], which can be evaluated from

contact solutions. These frictional stresses produce the maximum tensile stresses in the solid tabs, which are plotted as function of pullout distance for different coefficient of friction (figure 4.5c) and different locking angles (figure 4.5d). The contact stresses can also be illustrated with finite element results, with the lowest principal stress $\frac{\sigma_{\min}}{E}$ (i.e. maximum pressure, figure 4.6a,b) and the highest tensile stress $\frac{\sigma_{\max}}{E}$ (figure 4.6c). The contact pressure is distributed over the contact following the expected parabolic profile. The tensile stress is maximum at the edge of the contact surface which is "behind" the direction of sliding. Figure 4.6d and 4.6e show the pullout (force-displacement) curve and the maximum local stress as function of pullout distance. The analytical solution and finite element models are in good agreement.

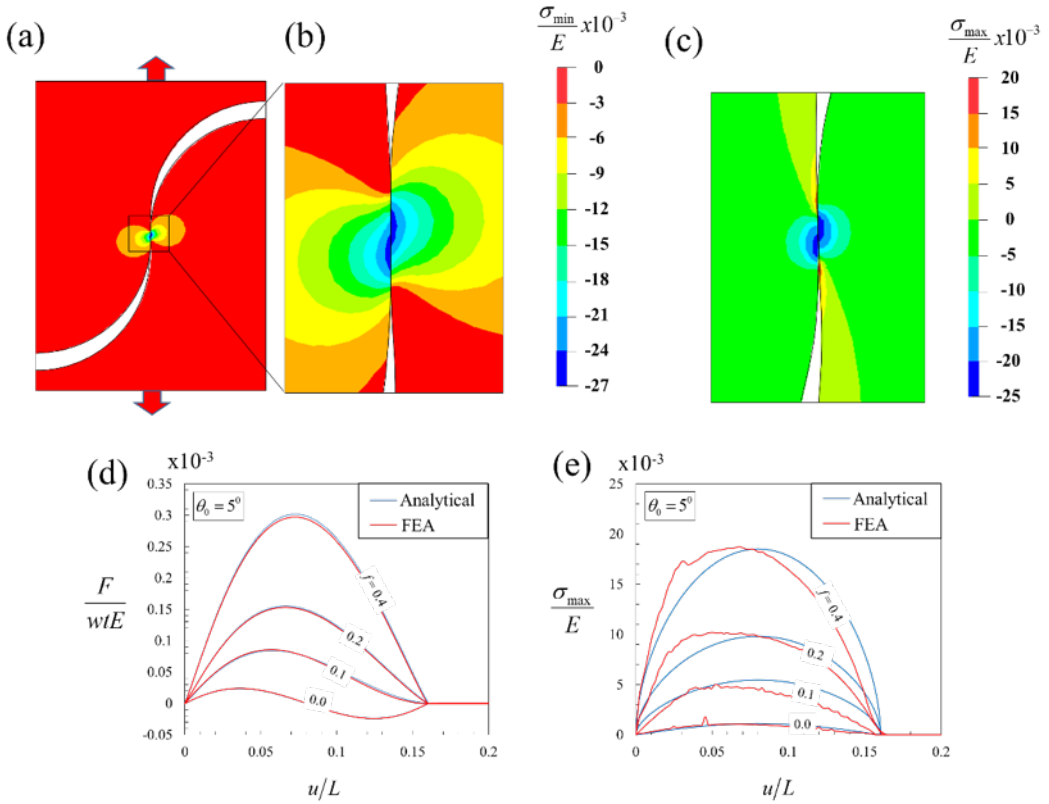

Figure 4.6: (a) and (b) contour plots of maximum pressure (minimum principal stress) for $\theta_0 = 5^0$ and $f = 0.4$; (c) contour plot of maximum principal stress (maximum tensile stress in the tabs); (d) and (e) traction and maximum tensile stresses as function of pullout distance showing a good agreement between the analytical and finite elements results.

The interlocking angle θ_0, and friction coefficient f, increase the maximum pulling force and total energy absorbed during pullout. However the associated local stresses in the solid may cause a premature fracture of the tab, therefore there is need for optimization. Here we performed an exhaustive search of the design space to identify the best combination(s) of design parameters for any given set of desired of normalized stiffness, strength, maximum extension, and energy absorption. The limiting factor for the design is the fracture of the solid tabs, which is governed by the strength of the material. The tabs will therefore fracture when $\sigma_{max}/E = \sigma_s/E$, where σ_{max} is the maximum tensile stress predicted from the model and σ_s is the tensile strength of the solid material. Here we present results for σ_s/E=1/100, which is a common ratio for engineering materials [37]. For a given value of friction coefficient, it is therefore possible to identify the optimum locking angle that will be the largest while preventing fracture of the tabs. The strength is simply $\frac{F_{\max}}{wtE}$, the maximum elongation is $\frac{u_{\max}}{L}$ and the energy absorbed is given by the area under the pullout force-displacement curve, $\frac{U}{wtLE} = \int_0^{u_{\max}} \frac{F}{wtE}\frac{du}{L}$. Figure 4.7a shows the allowable combinations of θ_0 and f that will prevent tab fracture and ensure the complete pullout the suture. Since strength and energy absorption both increase with θ_0 and f, the optimum combinations of θ_0 and f lie on the line defined by $\sigma_{max}/E = \sigma_s/E = 1/100$. As expected, if f is increased then θ_0 must be decreased to prevent the fracture of the tabs. Figure 4.7b shows the corresponding optimal energy absorption $\left(\frac{U}{wtLE}\right)_{opt}$ and the optimal strength $\left(\frac{F_{\max}}{wtE}\right)_{opt}$. The maximum pullout strength is achieved with a locking angle $\theta_0 = 12.75^0$ and a friction coefficient $f = 0$, and at a value $F_{max}/wtE \sim 0.5 \times 10^{-3}$. However, this design does not dissipate any energy upon pullout, because the frictional dissipative mechanise is absent (f=0). To reach the highest energy

dissipation possible f must be increased, and θ_0 must be decreased. The bell-shape of this curve shows there is an optimum point where the energy dissipation is maximum, which is achieved with a locking angle $\theta_0 = 9.25^0$ and friction coefficient $f = 0.06$. This exhaustive search can therefore be used to identify the suture geometry and local friction that will optimize strength and/or toughness. The results also highlight the main limitation of this design: the maximum strength of the suture is only about 5% of the tensile strength of the solid material. In the upcoming sections we explore enriched geometries that aim at reducing the frictional contact stresses by distributing the contact over larger areas.

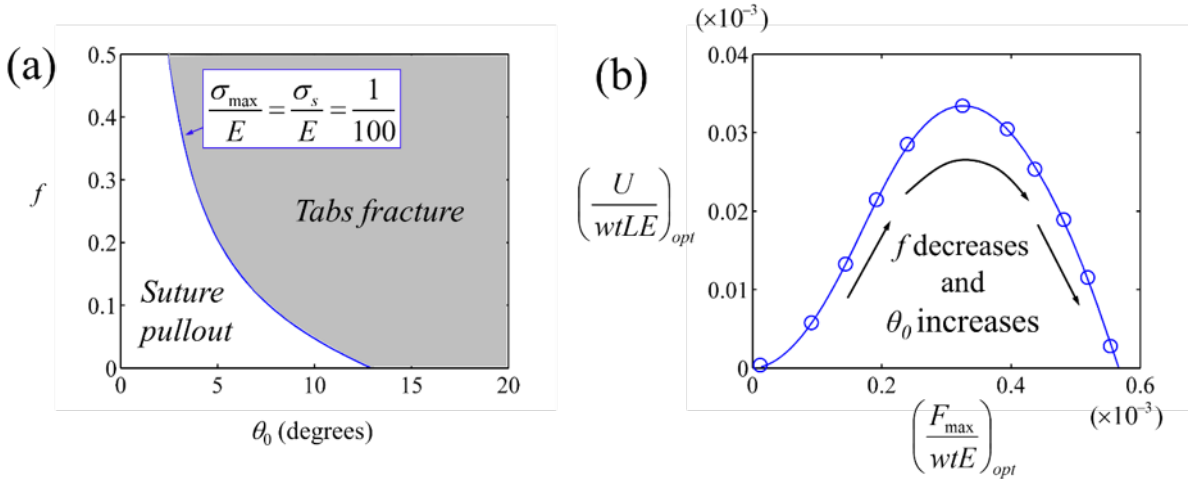

Figure 4.7: (a) Possible combinations of the parameters θ_0 and f for optimum designs; (b) Optimum energy absorbed and optimum pullout strength calculated using the constraint σ_s/E=1/100.

4.5.1 Dovetail-like sutures

As a first extension to the simple jigsaw geometry, we increased the contact area in order to better distribute and to decrease the contact stresses, and in particular those associated with friction. Reducing the contact stresses can delay the fracture of the solid materials, which can enable more extreme locking geometries and more efficient designs. A straight region of length d was added on the suture contour, which produced a "dovetail like" geometry (figure 4.8a,b). This dovetail suture can be described with three independent parameters: interlocking angle θ_0, radius of curvature R_0 and length of straight segment d, which were reduced to two parameters (θ_0 and d/R_0) after normalization. Other geometrical parameters are given by:

$$\begin{cases} \phi_0 = \theta_0 + \pi/2 \\ s_0 / R_0 = \phi_0 + d/2R_0 \\ w/R_0 = 4\sin\phi_0 + 2(d/R_0)\cos\phi_0 \\ L/R_0 = 2(1-\cos\phi_0) + (d/R_0)\sin\phi_0 \end{cases} \tag{4.15}$$

The $\phi(s)$ function (figure 4.8a) was defined as:

$$\begin{cases} \phi(s) = \dfrac{s}{R_0}, & 0 \le s \le s_0 - d/2 \\ \phi(s) = \phi_0, & s_0 - d/2 \le s \le s_0 \end{cases} \tag{4.16}$$

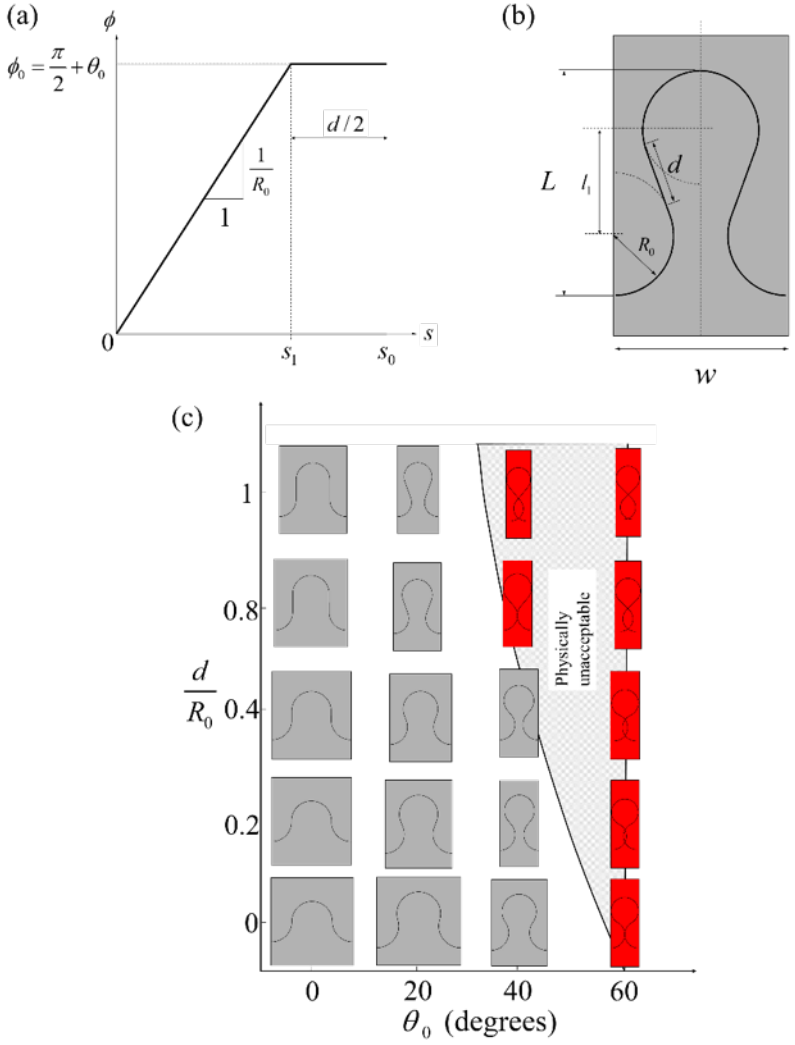

Figure 4.8: (a) (ϕ-s) curve for a two-parameter suture; (b) Corresponding profile; (c) The "strength" of the geometrical interlocking is governed by the interlocking angle θ_0 and the plateau length d/R_0. The geometries highlighted in red are not physically acceptable.

Figure 4.8c shows a set of dovetail suture profiles obtained for different combinations of θ_0 and d/R_0. For $d/R_0 = 0$ the single jigsaw geometry is recovered. With $d/R_0 > 0$ a wide range of geometries can be obtained, but some combinations of parameters lead to the contour intersecting itself. The condition for the contours not to intersect is $2R_0 < w$, which can be written:

$$\theta_0 < \cos^{-1}\left(\frac{R_0}{\sqrt{d^2 + 4R_0^2}}\right) - \tan^{-1}\left(\frac{d}{2R_0}\right) \tag{4.17}$$

On figure 4.8c, equation (4.17) defines the boundary between admissible geometries and inadmissible geometries. As the plateau length d/R_0, increases from zero (single locking) to higher values, the range of allowable locking angles θ_0 becomes narrower. To predict the pullout response of the dovetail suture we used the same procedure as for the single jigsaw model. An analytical solution was first developed by using a 2D flat punch with rounded edge as base solution for the contact interaction [38-41]. The kinematics of two disks in contact is the same as that described above using equation 4.11, and the normalized contact radius a/R_0 can be determined from non-Hertzian contact solution for two similar disks in contact (equation 4.18) [42]:

$$\frac{\delta}{R_0} = \frac{1}{2}\left(\frac{a}{R_0}\right)^2\left[\ln\left(16\left(\frac{R_0}{a}\right)^2\right) - 1\right] \tag{4.18}$$

The normalized contact surface a/R_0 can be obtained by solving equation (4.18) numerically. From a/R_0 one can compute the normal force for a flat punch with rounded ends for plane stress condition is given as [39]:

$$\frac{P}{R_0 tE} = \frac{1}{2}\left(\frac{b}{R_0}\right)^2\left[\frac{\pi}{2} - \frac{d}{2b}\sqrt{1 - \left(\frac{d}{2b}\right)^2} - \arcsin\left(\frac{d}{2b}\right)\right] \tag{4.19}$$

$$\frac{b}{R_0} = \frac{d}{2R_0} + \frac{a}{R_0} \tag{4.20}$$

The pullout is divided into three stages as shown in figure 4.9. The first stage involves the sliding of the flat portion and the interlocking angle remains unchanged while the contact length reduces from d to zero. The pullout distance in the first stage is given as:

$$u_0 = \Delta d \cos\ \theta_0 \tag{4.21}$$

Where Δd is the difference in the sliding length as the pullout progresses from zero to d. At the second and third stage the pullout distance is given by:

$$u_1 = 2R_0 \sin\theta_0 - (2R_0 - \delta)\sin\theta \tag{4.22}$$

where δ is the interference between two disks pressed against each other and θ is used to track the evolution of the interlocking angle.

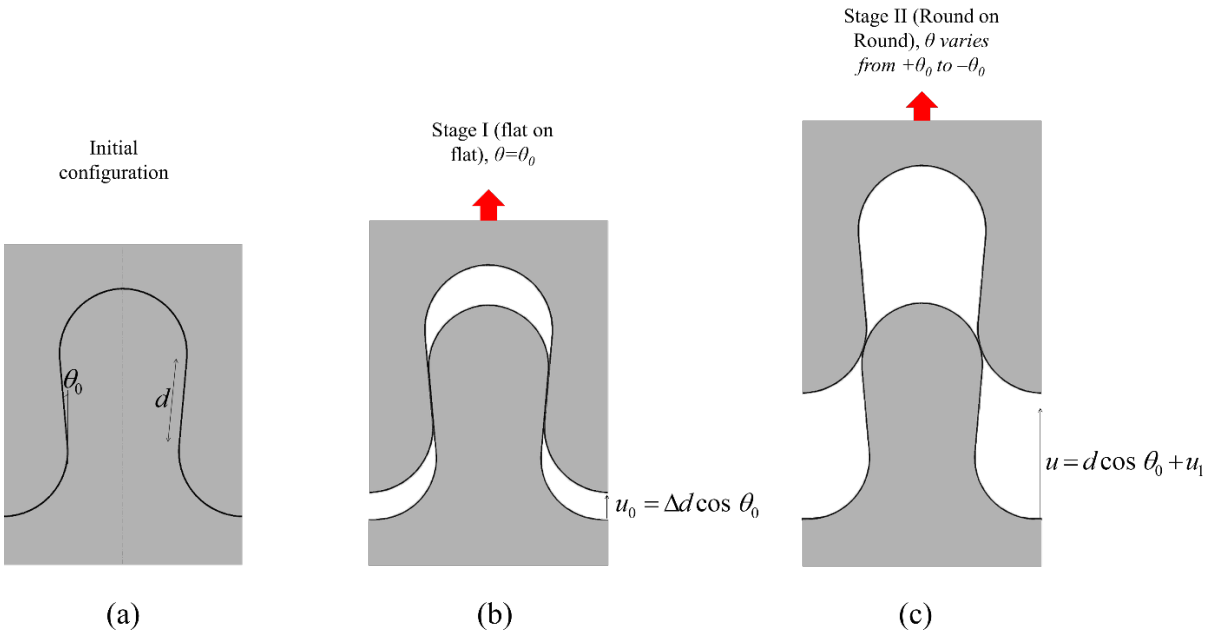

Figure 4.9: Stages of the pullout for a dovetail suture; (a) Initial stage (no force applied), (b) first pullout stage where the flat faces are in contact, (c) second stage where only the rounded sections are in contact.

Resolving the force components vertically and normalizing by the suture width provides the average pullout force:

$$\frac{F}{wtE} = \frac{P}{R_0 tE}\left(\frac{\sin\theta + f\cos\theta}{2\cos\theta_0 - d\sin\theta_0}\right) \tag{4.23}$$

The angle θ is used to track the progressive pullout of the suture, and it remains constant along the flat portion of the suture, but later evolves from $+\theta_0$ to $-\theta_0$ at the rounded ends of the suture. Figures 4.10a-c show the effect of friction coefficient f, interlocking angle θ_0, and plateau length d/R_0, on the average pullout force. Friction (Figure 4.10a) and interlocking angle (Figure 4.10b) have the same effect as we observed for the single jigsaw design- they both increase maximum pullout force and energy absorption. Increasing the length d of the plateau increases the area of contact, which increases the pullout force (Figure 4.10c).

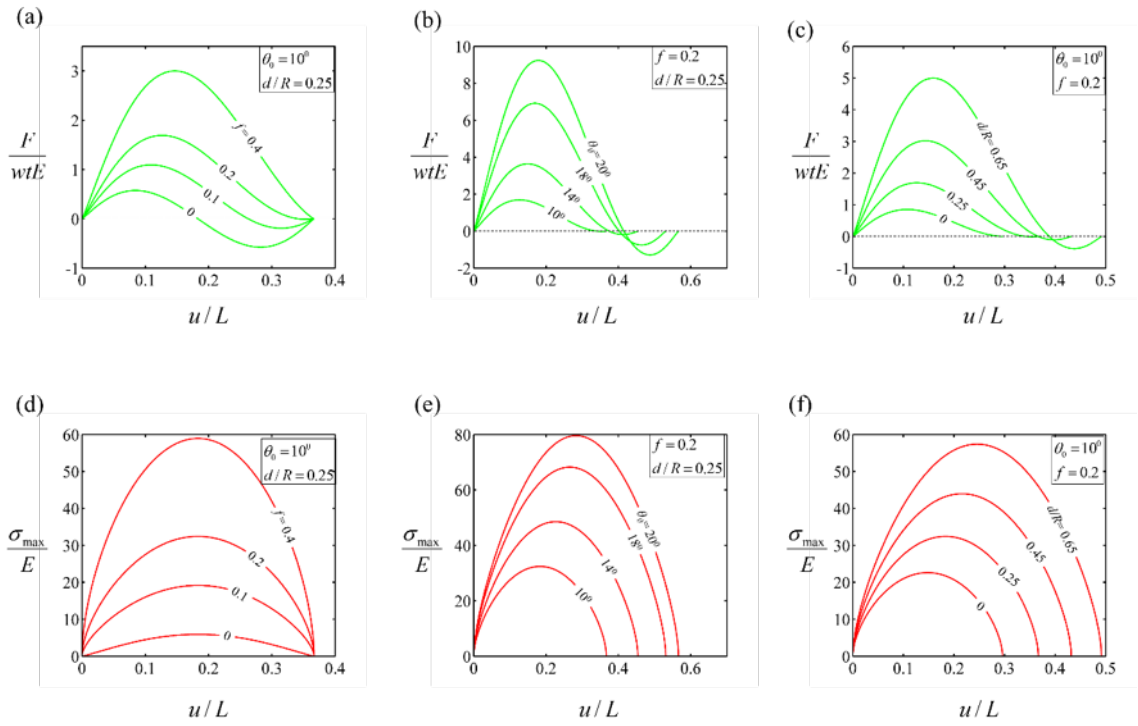

Figure 4.10: Effects of (a) friction f (b) interlocking angle θ_0, and (c) plateau length d/R_0, on the pullout response of the suture; effects of (d) friction f (e) interlocking angle θ_0, and (f) plateau length d/R_0, on maximum tensile stress in the solid tabs.

The maximum tensile stress in the suture is divided into frictional contact stress and frictionless (hole in an infinite plate loaded by a frictionless pin in the in-plane direction) maximum tensile stress. The frictionless maximum stress is given as [43]:

$$\sigma_{\max}^{(P)} = \frac{P}{R_0 t}\frac{5-\nu}{2\pi} \tag{4.24}$$

The sliding frictional contact stress is given as [39]:

$$\sigma_{\max}^{(fP)} = 2fpk \tag{4.25}$$

Where p is the contact pressure given as $p = \frac{2P}{\pi t b}$ and k is a geometrical factor that defines the effect of contact length ratio, $d/2b$ on the pressure distribution of flat punch with rounded edges. If $d = 0$, then $k = 1$ which reduces to a cylinder-on-cylinder contact [39].

$$p = \frac{2P}{\pi t b}$$

$$k = \sqrt{\frac{1-\left(2/\pi\right)\arcsin\left(d/2b\right)}{1-\left(2/\pi\right)\arcsin\left(d/2b\right)-\left(2/\pi\right)\left(d/2b\right)\sqrt{1-\left(d/2b\right)^2}}} \tag{4.26}$$

$$\sigma_{\max}^{(fP)} = \frac{4Pf}{\pi t b}k$$

Superposition of these two solutions gives the total stress at the trailing edge of the contact:

$$\sigma_{\max} = \sigma_{\max}^{(P)} + \sigma_{\max}^{(fP)} = \frac{P}{R_0 t}\frac{5-\nu}{2\pi} + \frac{4Pf}{\pi t b}k \tag{4.27}$$

Normalizing this equation gives:

$$\frac{\sigma_{\max}}{E} = \frac{1}{2\pi}\frac{P}{R_0 t E}\left[(5-\upsilon)+8\left(\frac{R_0}{b}\right)kf\right] \tag{4.28}$$

The maximum stress increases with interlocking angle, plateau length, and friction (Figure 4.10d, e, f). Figure 4.11 shows the minimum principal stress, maximum stress contour plots and the comparison between the pullout response and maximum stress. The result shows that both the analytical and finite element models are in good agreement. For the rest of this section we used the analytical model because of its simplicity.

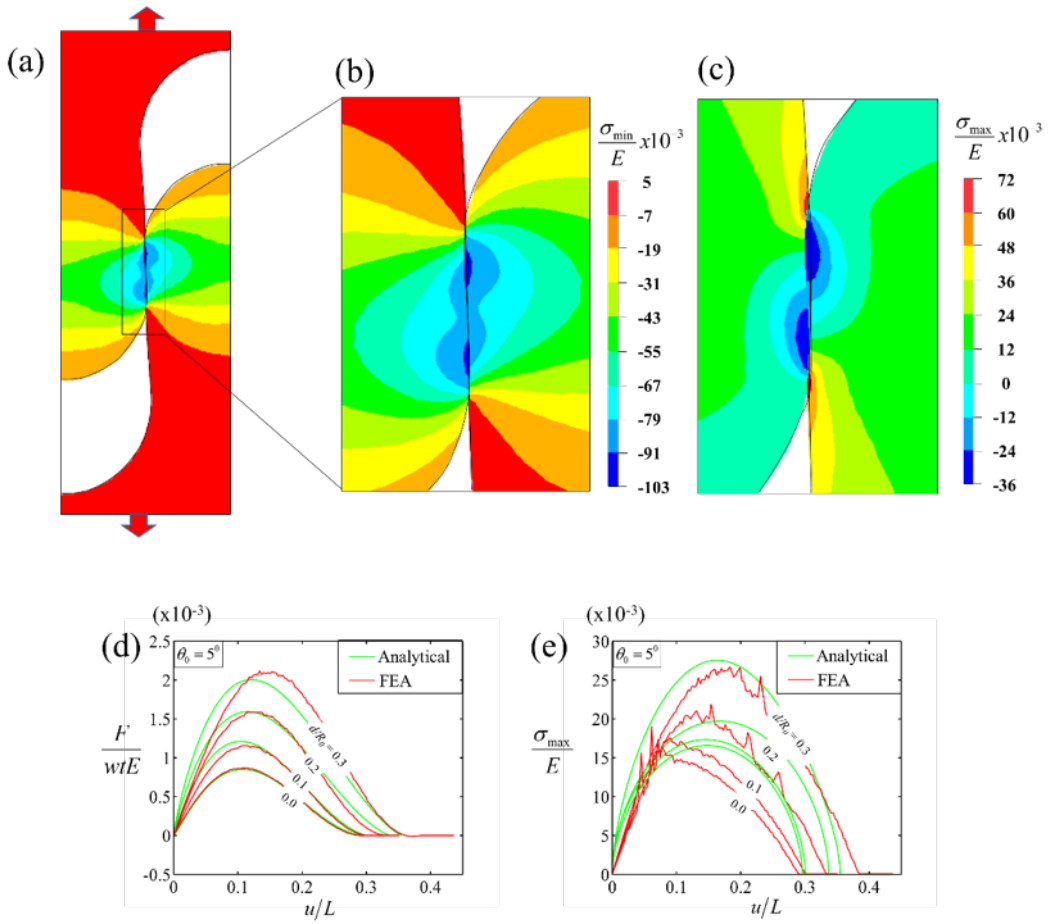

Figure 4.11: (a) and (b): contour plots of maximum pressure for $\theta_0 = 5^0$, $d = 0.8$, and $f = 0.4$; (c) contour plot of maximum principal stress (d) and (e) traction and stresses as function of pullout distance showing a good agreement between the analytical and finite elements results.

To identify optimum sets of design parameters, we followed the same procedure as for the single jigsaw, by performing an exhaustive parametric study on f, θ_0 and d/R_0. In particular, we identified optimum sets of parameters that prevent fracture of the tabs, using σ_s/E=1/100 for the tensile strength of the solid material. Figure 4.12(a) shows different combinations of f and θ_0 that achieve this condition, and for four different values of d/R_0. As expected, increasing the plateau d/R_0 must be accompanied by a reduction of f and/or θ_0 to prevent the fracture of the tab. Figure 4.12b shows the corresponding optimum energy absorption and strength. Compared to the single jigsaw tab design adding straight regions produced narrower bell-shape curves, because as mentioned above the range of permissible f and θ_0 is more

restricted. The dovetail design however produced higher increases energy absorption, up to 2.5 times higher than what can be obtained from the single jigsaw design. The maximum pullout strength possible is however the same, at $F_{max}/wtE \sim 0.5\text{x}10^{-3}$ for all designs. Interestingly, the optimum design achieves the highest possible strength and energy absorption simultaneously. This optimum design has a friction coefficient of 0.12, a long dovetail d/R_o =0.6 and a vanishingly small locking angle (θ_0=0.125º). A further increase in the plateau length ($d/R_0 > 0.6$) did not generate any further improvements.

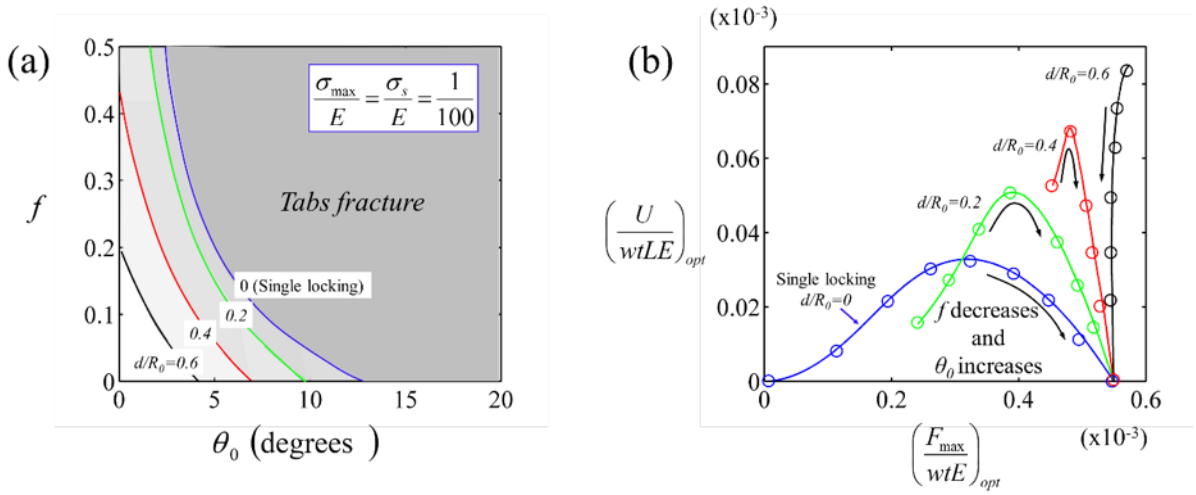

Figure 4.12: (a) Possible combination of the parameters θ_0, f, and d/R_0 for optimum designs; (b) material property map showing the optimum energy absorbed and the optimum pullout strength for different d/R_0 and for a design constraint σ_s/E=1/100.

4.5.3 Double locking sutures

The dovetail design demonstrated how distributing the contact stresses over a larger area could delay fracture of the tabs and lead to higher performance. We now examine another approach, where the pullout force is transferred over more than one contact area. "Double locking" suture geometries were obtained by enriching the $\phi(s)$ with a second segment with a nonzero slope (Figure 4.13a). The most interesting cases are produced when this second slope is negative, which then produces a second locking site of radius R_1 (Figure 4.13b). The slope of that segment is therefore $-1/R_1$ on the $\phi(s)$. This enriched design has therefore three

independent non-dimensional geometrical parameters: (i) interlocking angle θ_0, (ii) radii ratio R_0/R_1, (iii) cumulative angular function ϕ_0/ϕ_1. The suture angle function is written:

$$\begin{cases} \phi(s) = \dfrac{s}{R_0}, & 0 \le s \le s_1 \\ \phi(s) = 2\phi_0 - \dfrac{s}{R_1}, & s_1 \le s \le s_0 \end{cases} \tag{4.29}$$

Other geometrical parameters are written:

$$\begin{cases} \phi_0 = \theta_0 + \pi/2 \\ \phi_1 = -\theta_1 + \pi/2 \\ s_1 = R_0\phi_0 \\ s_0 = R_0\phi_0 + R_1(\theta_0 + \theta_1) \\ w = 2\left[2(R_0 + R_1)\sin\phi_0 - 2R_1\sin\phi_1\right] \\ L = 2\left[R_0(1-\cos\phi_0) - R_1(\cos\phi_0 - \cos\phi_1)\right] \end{cases} \tag{4.30}$$

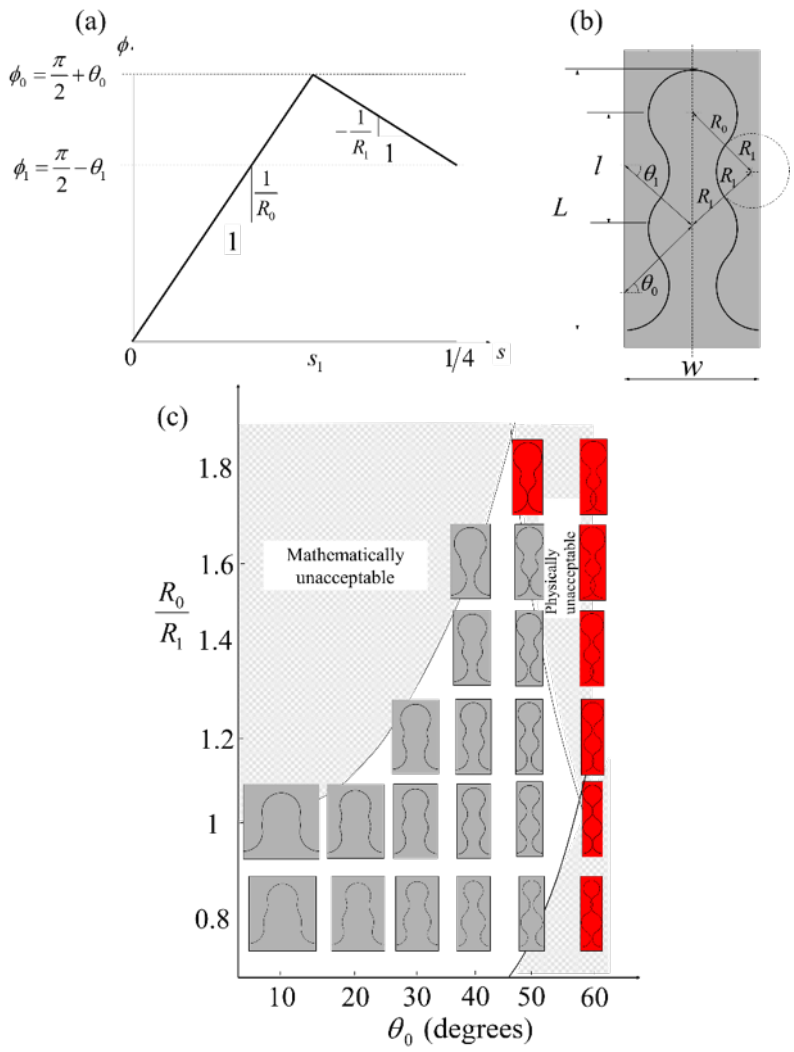

Figure 4.13: (a) (ϕ-s) curve for a two-parameter suture; (b) Corresponding profile; (c) The "strength" of the geometrical interlocking is governed by the interlocking angle θ_0 and by R_0/R_1. The geometries highlighted in red are not physically acceptable.

There are geometric constraints on R_0 / R_1 and θ_0 which restrict the range of possible designs for this suture. The transition angle θ_1 can be written:

$$\theta_1 = \cos^{-1}\left(\frac{1}{2}\left(\frac{R_0}{R_1}+1\right)\cos\theta_0\right) \tag{4.31}$$

However equation (4.31) has a solution only if:

$$\frac{R_0}{R_1} \le \frac{2}{\cos\theta_0} - 1 \tag{4.32}$$

In addition the contour of the suture cannot intersect, therefore a physical condition is given as:

$$\frac{1-\cos\theta_0}{\cos\theta_0} < \frac{R_0}{R_1} < \frac{\cos\theta_0}{1-\cos\theta_0} \tag{4.33}$$

Equations (4.32) and (4.33) define the boundaries of admissible geometries for this type of sutures (figure 4.13c). The pullout response can be decomposed into two stages. In the first stage, the two pairs of locking sites are in contact (figure 4.14a). As the pullout progresses the system may reach a second stable locking configuration, which can occur if $R_0/R_1 \geq 1$. Further pullout from that position only involves one contact pair. Using figure 4.3a-c, and figure 4.13b above, we can derive the kinematics relations for stage 1:

$$\frac{\delta}{R_0} = \left(1+\frac{R_1}{R_0}\right)\left[1-\frac{\cos\theta_0}{\cos\theta}\right] \tag{4.34}$$

$$\frac{u}{L} = \frac{\sin\theta_0 - \sin\theta + 0.5(\delta/R_0)\sin\theta}{1+3\sin\theta_0} \tag{4.35}$$

$$\frac{F}{wtE} = \frac{P}{R_0 tE}\left(\frac{\sin\theta + f\cos\theta}{\cos\theta_0}\right) \tag{4.36}$$

At the second stage:

$$\frac{u}{L} = \frac{3\sin\theta_0 - \sin\theta + 0.5(\delta/R_0)\sin\theta}{1+3\sin\theta_0} \tag{4.37}$$

$$\frac{F}{wtE} = \frac{P}{R_0 tE}\left(\frac{\sin\theta + f\cos\theta}{2\cos\theta_0}\right) \tag{4.38}$$

These equations are combined to compute the pullout response of the suture. We found that f and θ_0 have the expected effect: they both increase the strength and energy absorption of the suture, but they also increase the maximum stress in the tabs. Figure 4.14b shows the effect

of R_0/R_1 on the pullout response. The case R_0/R_1 =1 produces two force peaks, the first peak corresponding to the force generated by two contact pairs, the second peak being generate by only one contact pair. As a result, the second peak is half of the first one. Interestingly increasing R_0/R_1 increases the second peak, because the second pullout stage is generated by a larger geometric interference between the tabs. This effect is very sensitive to the value of R_0/R_1. For R_0/R_1=1.02 the two peaks are equal, and for R_0/R_1=1.03 the second peak becomes higher than the first. This "geometric hardening" can generate some attractive mechanisms at large length scales [26].

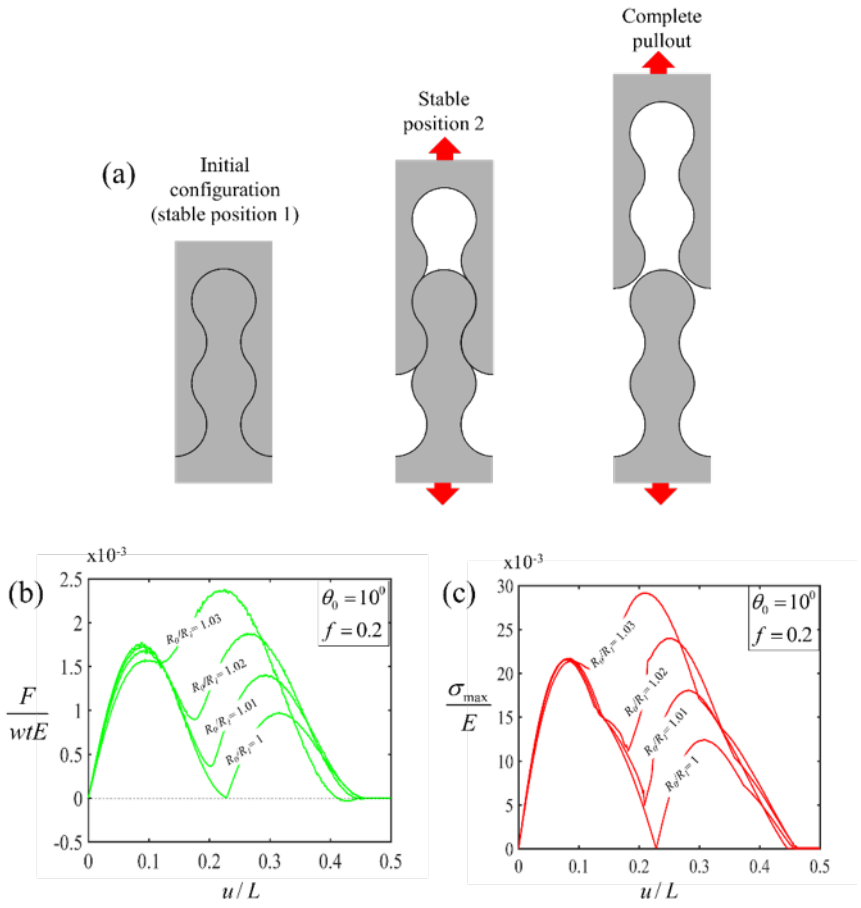

Figure 4.14: (a) Progressive pullout showing the two locking stages; effects of radii ratio R_0/R_1 on (b) pullout response and (c) maximum tensile stress in the solid tabs.

The maximum tensile stresses can be divided into a contribution from normal forces, and a contribution from the frictional forces.

(i) *Hole in an infinite plate loaded by a frictionless pin in the in-plane direction* [43, 44]: in this configuration the inner side of a hole is loaded by a contact force acting along the radial direction. The resulting maximum tensile stress is the tangential stress at the edge of the contact area.

$$\sigma_{\max}^{(P)} = \frac{P}{Rt}\frac{5-\nu}{2\pi} \tag{4.39}$$

(ii) *Periodic frictional contact*: With a sliding frictional contact, the maximum tensile stress is close to the trailing edge of contact. A solution was derived using Kolosov-Muskhelishvili general formula and the theory of automorphic functions [45-47]. A sinusoidal periodic contact problem is considered and the sinusoidal equation with amplitude Δ and wavelength l is given as:

$$y = \delta - \Delta\left(1 - \cos\frac{2\pi x}{l}\right) \tag{4.40}$$

Where x is the coordinate of the interface, δ is the interference between two contacting tabs. Assume that the contact area and the amplitude is small ($a<<R$ and $\Delta<<R$), the maximum pressure is given as:

$$p_0 = \frac{El}{2\pi R_0}\sin\left(\frac{\pi b}{l}\right) \tag{4.41}$$

Where R_0 is the radius of curvature, b is the half-width of contact area and it is given as $b = \frac{l}{\pi}\sin^{-1}\left(\frac{\pi a}{l}\right)$, E, ν are the elastic modulus and Poisson's ratio for the solid material. The maximum tangential stress in frictional contact is given as $\sigma_{\max}^{(fP)} = 2fp_0$ [42], and the superposition of both frictionless and periodic frictional contact stresses gives the maximum tensile stress in the suture. Figure 4.14c shows the dependence of maximum tensile stress on

radii ratio R_0/R_1. The maximum pressure and maximum stress from the finite element model are shown in figure 4.15a-c below. The maximum stress occurred at the edge of the contact region (Figure 4.15c) which agrees with the analytical solution. Figure 4.15d and 4.15e shows excellent agreement between the finite elements and analytical predictions in terms of pullout response and maximum tensile stress within the material.

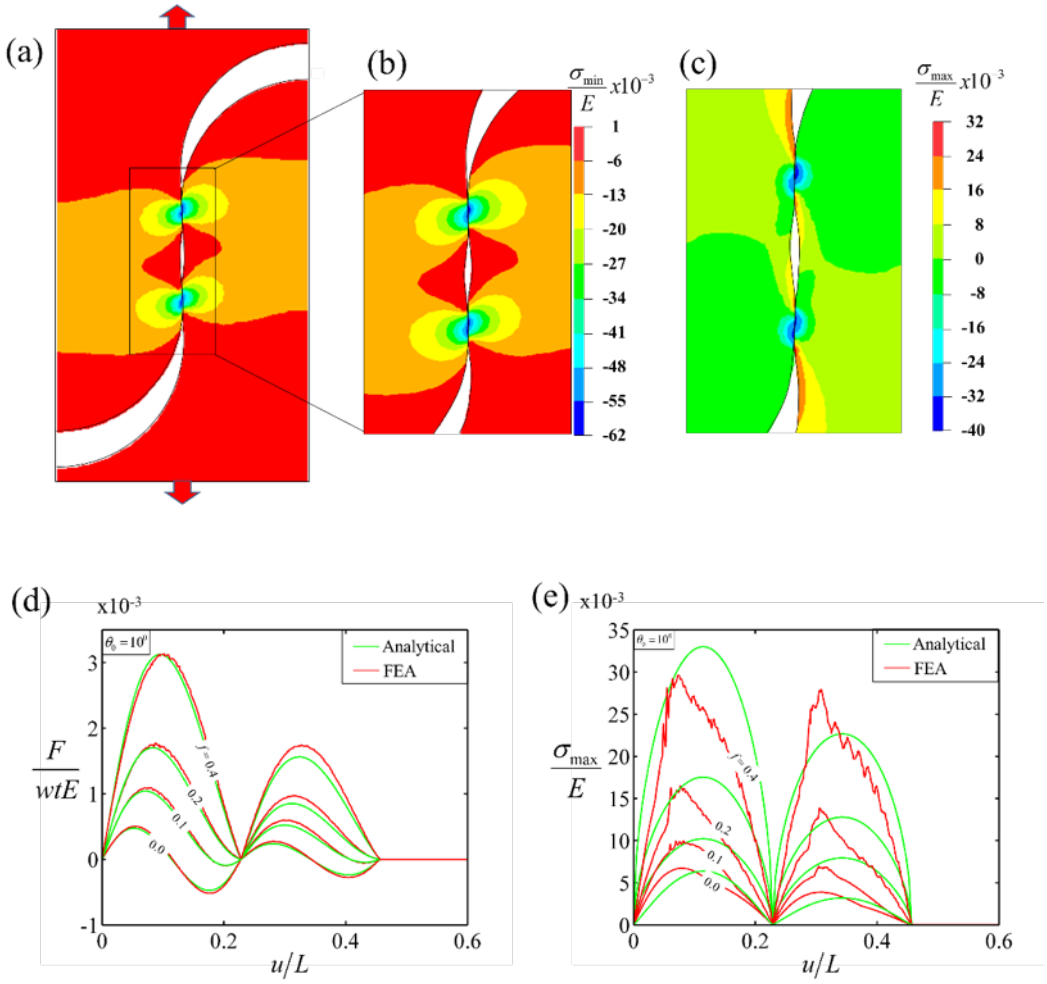

Figure 4.15: (a) and (b) contour plots of maximum pressure for $\theta_0 = 10^0$ and $f = 0.4$; (c) contour plot of maximum principal stress (d) and (e) traction and stresses as function of pullout distance showing a good agreement between the analytical and finite elements results.

A design optimization was performed on the geometry of the double locking design, with the maximum stress in the tab as design constraint. The material fractures when $\frac{\sigma_{max}}{E} = \frac{\sigma_S}{E}$ and figure 4.16a shows for any given radii ratio R_0/R_1, the possible combination(s) of friction

coefficient f and interlocking angle θ_0 from the optimization method by setting the strength-modulus ratio to $\frac{\sigma_S}{E} = \frac{1}{100}$. The results show that R_0/R_1 has little effect on the failure map within the range explored. Figure 4.16b shows the optimum energy absorption and strength of material distribution for different designs. Compared to the single locking design, the double locking design increases the optimum strength by a factor of two, and the optimum energy absorption by a factor of about three. When R_0/R_1 is increased the possible range of angles and friction becomes narrower, and relatively high values of R_0/R_1 (R_0/R_1 =1.02) become sub-optimal in terms of energy absorption. For all designs, the optimum material properties are achieved with a low friction coefficient f, and relatively high interlocking angle θ_0.

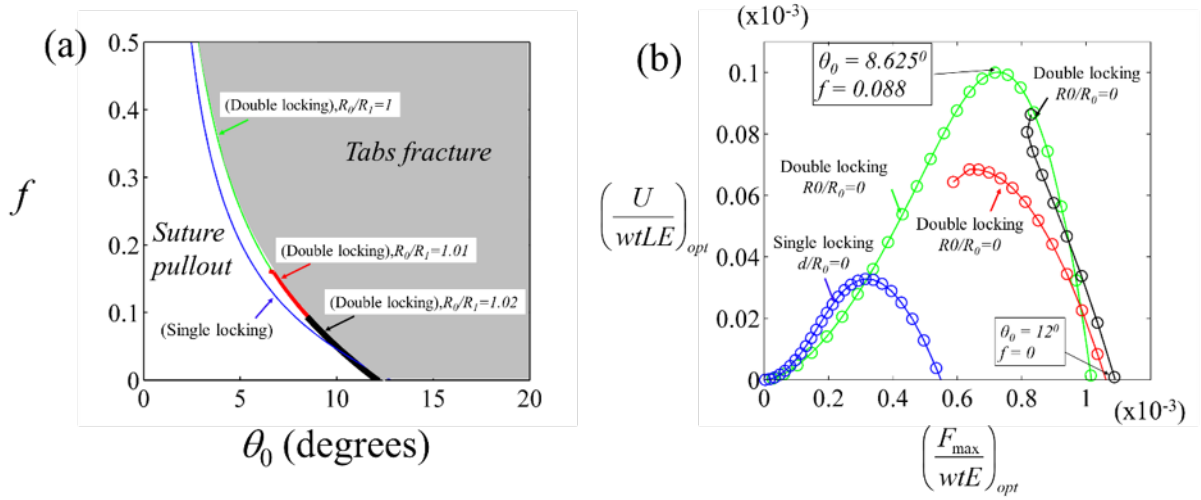

Figure 4.16: (a) Possible combination of the parameters θ_0, f and R_0/R_1 for optimum designs; (b) material property map showing the optimum energy absorbed and the optimum pullout strength, for R_0/R_1=*1, 1.01, 1.02* and with the design constraint σ_s/E=1/100.

4.5.4 Multi-locking (N>2) suture geometries

With the same objective to decrease the frictional stress by creating more contact points, we finally explore locking geometries with N (N>2) pairs of locking sites. Figure 4.17a shows a $\phi(s)$ function for a N=3 design. There are seven independent, normalized geometric

parameters for N=3: θ_0, R_0/R_1, R_0/R_2, R_1/R_2, ϕ_0/ϕ_1, ϕ_0/ϕ_2, and ϕ_1/ϕ_2. More generally, multi-locking sutures with N contact pairs have $1+2\sum_{k=1}^{N-1}(N-k)$ independent, normalized geometric parameters: θ_0, R_0/R_1, ..., R_0/R_{N-1}, ϕ_0/ϕ_1, ..., ϕ_0/ϕ_{N-1}. The previous section showed that in terms of strength and energy absorption R_0/R_1 = 1 is the best design for double locking sutures. Therefore in this section we only consider cases where $R_0=R_1=\ldots=R_{N-1}=1$.

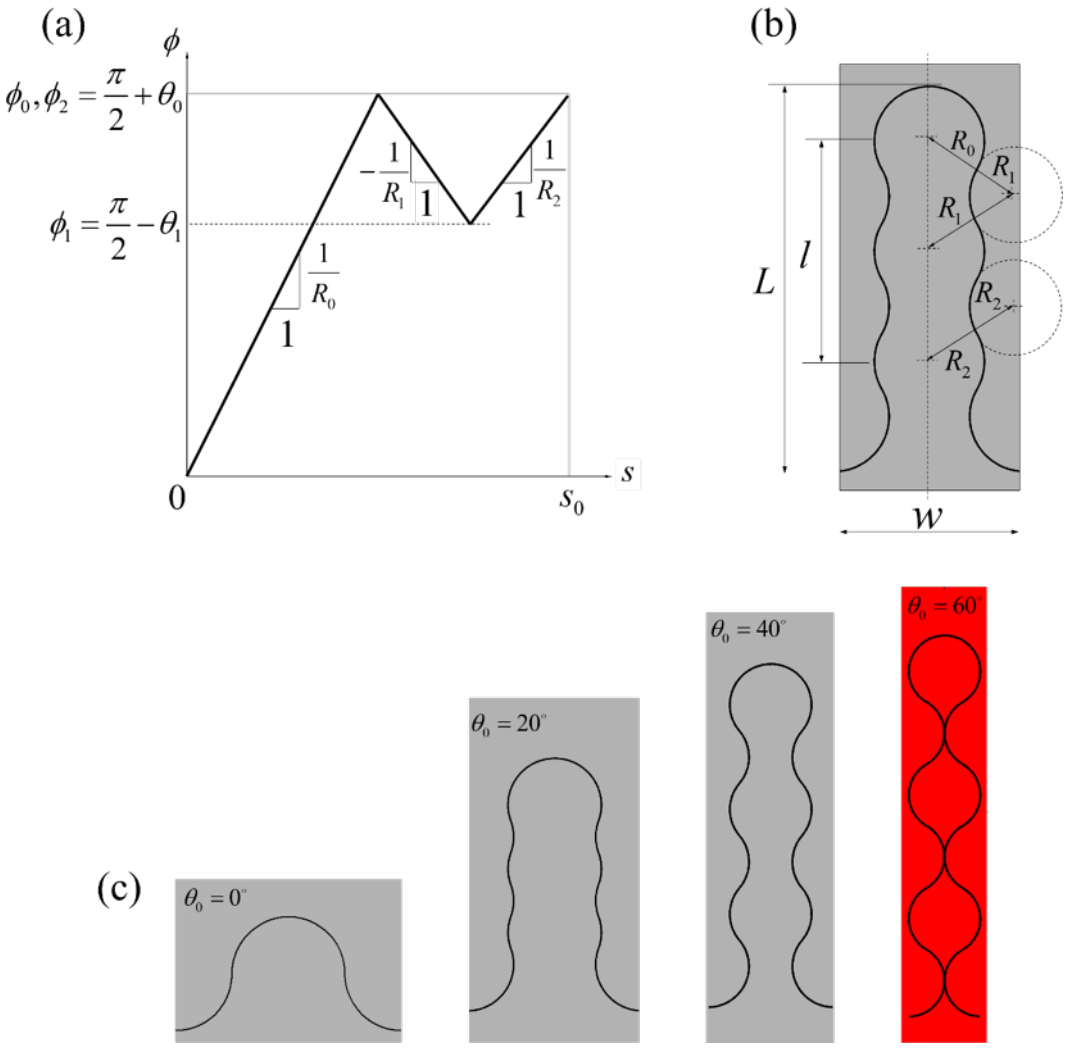

Figure 4.17: (a) (ϕ-s) curve for a two-parameter suture; (b) Corresponding profile; (c) Here the "strength" of the geometrical interlocking is governed by the interlocking angle θ_0 and by the number of clocking sites. The cases highlighted in red is not physically acceptable.

A closed form for the pullout response can be obtained by extending the N=2 solution. There are N stages of pullout, and the pullout force for the first stage is given as:

$$\frac{F}{wtE} = \frac{NP}{R_0 tE}\left(\frac{\sin\theta + f\cos\theta}{2\cos\theta_0}\right) \tag{4.42}$$

The equations for stress are similar to the double locking and the major difference is the half-width of contact b and length l, which is given as $b = \frac{l}{\pi}\sin^{-1}\left(\frac{\pi a}{l}\right)$, for all sutures with $N > 1$.

Figure 4.18b and 4.18c show the effect of N on the pullout force and maximum tensile stress. For each design there is a total of N local peaks of force corresponding to N stages of pullout. The first peak is the maximum pullout force, and it increases proportionally with N because of the addition of locking sites of equal strength. The peaks then decrease linearly until complete pullout. For comparison we also performed finite element simulations, with some representative results shown in Figures 4.19. The progressive pullout was captured in the models (Figure 4.19a) and we obtained good agreement with the closed form solution in terms of pullout behaviour (Figure 4.19b) and maximum stress (Figure 4.19c).

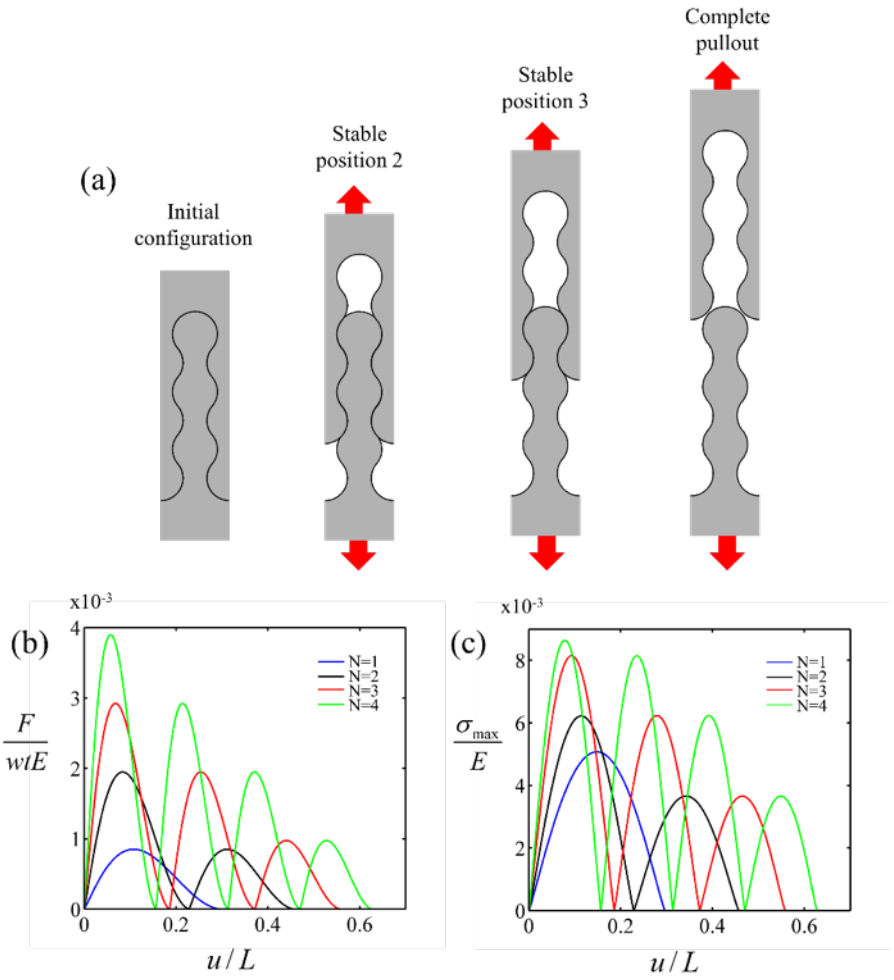

Figure 4.18: (a) Progressive pullout showing the three locking stages for suture with $N = 3$; effect of number of locking on (b) average pullout force of the suture, and (c) maximum tensile stress in the solid tabs.

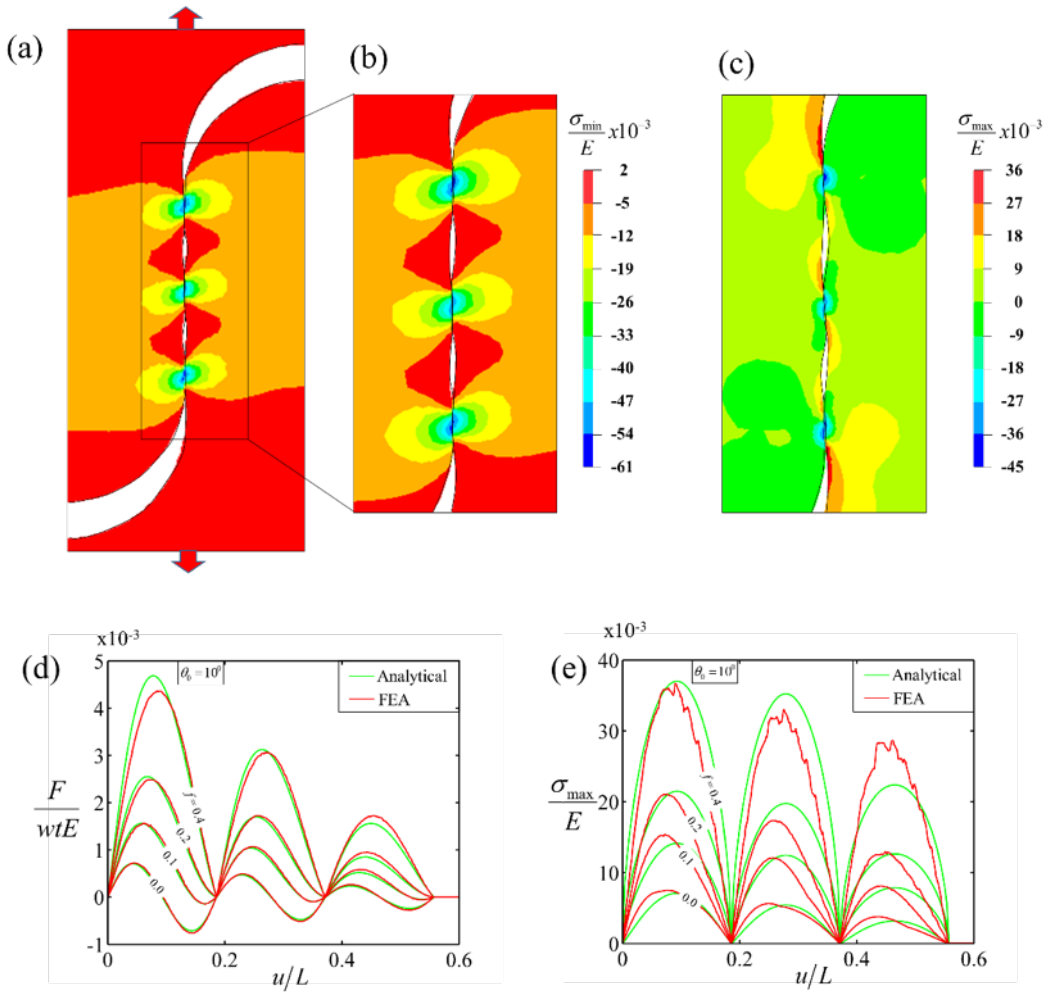

Figure 4.19: (a) and (b) contour plots of maximum pressure for $\theta_0 = 10^0$, $N = 3$, and $f = 0.4$; (c) contour plot of maximum principal stress (d) and (e) traction and stresses as function of pullout distance showing a good agreement between the analytical and finite elements results.

The failure transition map (Figure 4.20a) is not affected by a significant by *N*. The material property map for *N*=1 to *N*=7 (Figure 4.20b) reveal that the optimum strength increases up to *N*=4-5, but then decreases thereafter. The optimum energy absorption increases by a significant margin up to *N*=4-5, after which the gain is marginal for *N* =6 and 7, and above *N* = *7*, the optimum energy absorption continuously decreases.

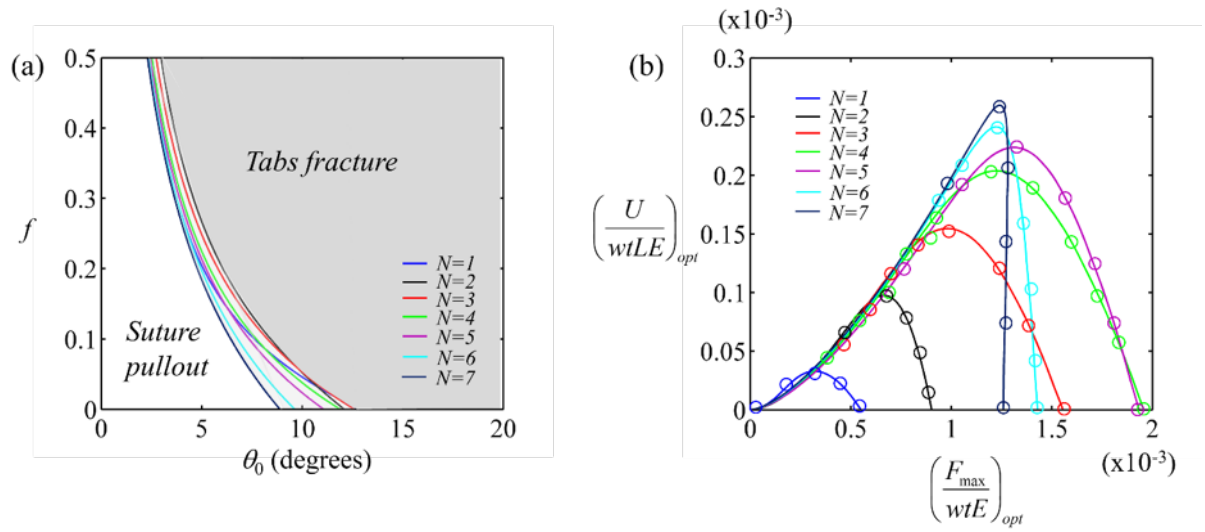

Figure 4.20: (a) Possible combinations of the parameters θ_0, f and N for optimum designs; (b) Material property map showing the optimum energy absorbed and the optimum pullout strength, for design constraints σ_s/E=1/100.

4.6 Summary

Sutured interfaces and geometric interlocking are common in natural materials. In this study we used a morphometric method to capture the contour of sutures by using the cumulative angular function $\phi(s)$ as a function of curvilinear position s. The two dimensional profile (x-y) of the suture is then easily reconstructed from $\phi(s)$. While the method is simple, relatively complex profiles can be captured using only a few geometrical parameters. Importantly, the method allows for re-entrant features, an essential characteristic of interlocking sutures. The study starts with a simple jigsaw-like model which is enriched with additional features (plateau regions in dovetail-like sutures, multiple locking sites). For each case, closed form solutions are developed to capture the full nonlinear pullout response and to predict the maximum stress (and potential fracture) in the solid material. These closed form solution are in close agreement with finite elements. A "brute force" optimization approach was used on each type of design, where every combination of geometrical parameters is examined. We could then identify the optimum parameters for pullout strength and/or energy absorption.

Figure 4.21 summarizes our finding by showing the best design and their performance. The single locking material is largely outclassed by all the other designs, and we found that the best geometry is the multi-locking tab with N=5 (using a limit strength for the solid of $\frac{\sigma_S}{E}=\frac{1}{100}$, which is typical of engineering materials). For comparison, the pullout of a perfectly straight cylindrical rod or fiber would require an initial compressive stress across the interface to generate any pullout force. In fiber reinforced ceramic-ceramic composites, this initial compression can be generated, for example, by thermal expansion mismatch between fiber and matrix [48]. In contrast, our sutures start in a stress-free state, and compression across the interfaces is generated by geometric interference as the suture is pullout out. Overall the limiting factor for optimization is the frictional stress, and the results show that it is very advantageous to add more contact points to decrease that stress. For the same reason it is also preferable to use very low coefficients of frictions. This result raises an interesting hypothesis on the function of the protein layer in natural sutured lines. These soft proteins are often described as essential to provide compliance and toughness at the interface. Our result suggest that their function could also be to "lubricate" the suture line to prevent the fracture of the solid structures. These models can serve as guidelines to design and optimization of non-adhesive sutures with arbitrary shapes from multilinear signatures or sutures made of arc of circles and lines.

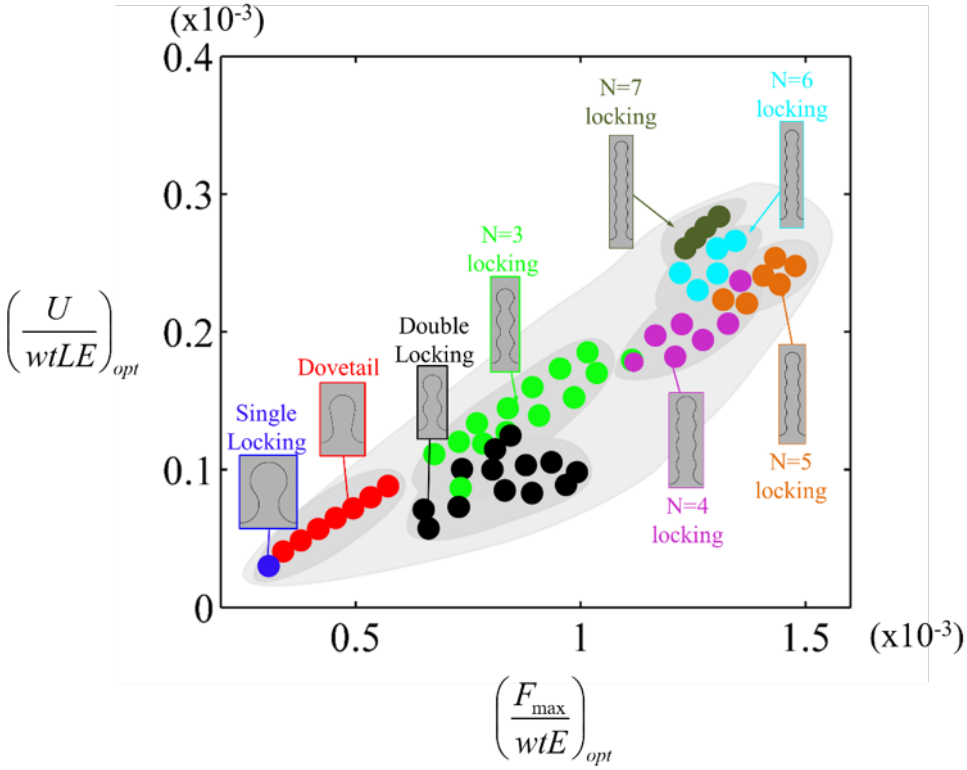

Figure 4.21: Material property map showing the optimum energy absorbed and the optimum pullout strength for all the designed explored in this study (σ_s/E=1/100).

4.7 Acknowledgements

This work was supported by a Discovery Grant from the Natural Sciences and Engineering Research Council of Canada (NSERC). IAM was supported by a Scholarship from the Nigerian Government through the National Universities commission.

4.8 References

1. Allen, E.G., *Understanding ammonoid sutures: New insight into the dynamic evolution of Paleozoic suture morphology*. Cephalopods Present and Past: New Insights and Fresh Perspectives, ed. N.H. Landman, R.A. Davis, and R.H. Mapes. 2007. 159-180.

2. Coats, B. and S.S. Margulies, *Material Properties of Human Infant Skull and Suture at High Rates.* Journal of Neurotrauma, 2006. **23**(8): p. 1222-1232.

3. Maloul, A., et al., *Characterization of craniofacial sutures using the finite element method.* Journal of Biomechanics, 2014. **47**(1): p. 245-252.

4. Miura, T., et al., *Mechanism of skull suture maintenance and interdigitation.* Journal of Anatomy, 2009. **215**(6): p. 642-655.

5. Achrai, B., B. Bar-On, and H.D. Wagner, *Bending mechanics of the red-eared slider turtle carapace.* Journal of the Mechanical Behavior of Biomedical Materials, 2014. **30**: p. 223-233.

6. Chen, I.H., W. Yang, and M.A. Meyers, *Leatherback sea turtle shell: A tough and flexible biological design.* Acta Biomaterialia, 2015. **28**: p. 2-12.

7. Zhang, W., et al., *Microstructure and mechanical property of turtle shell.* Theoretical and Applied Mechanics Letters, 2012. **2**(1): p. 014009.

8. Lee, N., et al., *Hierarchical multiscale structure-property relationships of the red-bellied woodpecker (Melanerpes carolinus) beak.* Journal of the Royal Society Interface, 2014. **11**(96).

9. Dunlop, J.W.C., R. Weinkamer, and P. Fratzl, *Artful interfaces within biological materials.* Materials Today, 2011. **14**(3): p. 70-78.

10. Barthelat, F., Z. Yin, and M.J. Buehler, *Structure and mechanics of interfaces in biological materials.* Nature Reviews Materials, 2016. **1**(4).

11. Li, Y., C. Ortiz, and M.C. Boyce, *Bioinspired, mechanical, deterministic fractal model for hierarchical suture joints.* Physical Review E, 2012. **85**(3).

12. Lin, E., et al., *Tunability and enhancement of mechanical behavior with additively manufactured bio-inspired hierarchical suture interfaces.* Journal of Materials Research, 2014. **29**(17): p. 1867-1875.

13. Maloul, A., et al., *Characterization of craniofacial sutures using the finite element method.* Journal of Biomechanics. **47**(1): p. 245-252.

14. Genkal, S.I. and G.I. Popovskaya, *Centric diatom algae of the Selenga River and its delta branches.* Inland Water Biology, 2008. **1**(2): p. 120-128.

15. Manoylov, K.M., N. Ognjanova-Rumenova, and R.J. Stevenson, *Morphotype variations in subfossil diatom species of Aulacoseira in 24 Michigan Lakes, USA.* Acta Botanica Croatica, 2009. **68**(2): p. 401-419.

16. Li, Y., C. Ortiz, and M.C. Boyce, *Stiffness and strength of suture joints in nature.* Physical Review E, 2011. **84**(6).

17. Barthelat, F., et al., *On the mechanics of mother-of-pearl: A key feature in the material hierarchical structure.* Journal of the Mechanics and Physics of Solids, 2007. **55**(2): p. 306-337.

18. Barthelat, F., Z. Yin, and M.J. Buehler, *Structure and mechanics of interfaces in biological materials.* Nature Reviews Materials, 2016. **1**: p. 16007.

19. Fratzl, P., I. Burgert, and H.S. Gupta, *On the role of interface polymers for the mechanics of natural polymeric composites.* Physical Chemistry Chemical Physics, 2004. **6**(24): p. 5575-5579.

20. Malik, I.A., M. Mirkhalaf, and F. Barthelat, *Bio-inspired "jigsaw"-like interlocking sutures: Modeling, optimization, 3D printing and testing.* Journal of the Mechanics and Physics of Solids, 2017. **102**: p. 224-238.

21. Li, Y., C. Ortiz, and M.C. Boyce, *A generalized mechanical model for suture interfaces of arbitrary geometry.* Journal of the Mechanics and Physics of Solids, 2013. **61**(4): p. 1144-1167.

22. Lin, E., et al., *3D printed, bio-inspired prototypes and analytical models for structured suture interfaces with geometrically-tuned deformation and failure behavior.* Journal of the Mechanics and Physics of Solids, 2014. **73**: p. 166-182.

23. Zavattieri, P.D., L.G. Hector, Jr., and A.F. Bower, *Cohesive zone simulations of crack growth along a rough interface between two elastic-plastic solids.* Engineering Fracture Mechanics, 2008. **75**(15): p. 4309-4332.

24. Malik, I.A. and F. Barthelat, *Toughening of thin ceramic plates using bioinspired surface patterns.* International Journal of Solids and Structures, 2016.

25. Mirkhalaf, M., A.K. Dastjerdi, and F. Barthelat, *Overcoming the brittleness of glass through bio-inspiration and micro-architecture.* Nature communications, 2014. **5**: p. 3166.

26. Mirkhalaf, M. and F. Barthelat, *Design, 3D printing and testing of architectured materials with bistable interlocks.* Extreme Mechanics Letters, 2017. **11**(Supplement C): p. 1-7.

27. Haldar, S., T. Sain, and S. Ghosh, *A novel high symmetry interlocking micro-architecture design for polymer composites with improved mechanical properties.* International Journal of Solids and Structures, 2017. **124**(Supplement C): p. 161-175.

28. Cray, J., M.P. Mooney, and M.I. Siegel, *Timing of ectocranial suture activity in Pan troglodytes as related to cranial volume and dental eruption.* The Anatomical Record, 2010. **293**(8): p. 1289-1296.

29. Saunders, W.B., D.M. Work, and S.V. Nikolaeva, *Evolution of complexity in paleozoic ammonoid sutures.* Science, 1999. **286**(5440): p. 760-763.

30. Allen, E.G., *New approaches to fourier analysis of ammonoid sutures and other complex, open curves.* Paleobiology, 2016. **32**(2): p. 299-315.

31. Dommergues, C.H., J.-L. Dommergues, and E.P. Verrecchia, *The Discrete Cosine Transform, a Fourier-related Method for Morphometric Analysis of Open Contours.* Mathematical Geology, 2007. **39**(8): p. 749-763.

32. Klug, C. and R. Hoffmann, *Ammonoid Septa and Sutures*, in *Ammonoid Paleobiology: From anatomy to ecology*, C. Klug, et al., Editors. 2015, Springer Netherlands: Dordrecht. p. 45-90.

33. Pérez-Claros, J.A., P. Palmqvist, and F. Olóriz, *First and Second Orders of Suture Complexity in Ammonites: A New Methodological Approach Using Fractal Analysis.* Mathematical Geology, 2002. **34**(3): p. 323-343.

34. Zahn, C.T. and R.Z. Roskies, *Fourier Descriptors for Plane Closed Curves.* IEEE Transactions on Computers, 1972. **C-21**(3): p. 269-281.

35. Fang, Y., et al. *3D deep shape descriptor*. in *2015 IEEE Conference on Computer Vision and Pattern Recognition (CVPR)*. 2015.

36. Kim, H.-K. and J.-D. Kim, *Region-based shape descriptor invariant to rotation, scale and translation.* Signal Processing: Image Communication, 2000. **16**(1–2): p. 87-93.

37. Ashby, M.F., *Chapter 4 - Material Property Charts*, in *Materials Selection in Mechanical Design (Fourth Edition)*. 2011, Butterworth-Heinemann: Oxford. p. 57-96.

38. Ciavarella, M., D.A. Hills, and G. Monno, *The influence of rounded edges on indentation by a flat punch.* Proceedings of the Institution of Mechanical Engineers, Part C: Journal of Mechanical Engineering Science, 1998. **212**(4): p. 319-327.

39. Ciavarella, M., G. Macina, and G.P. Demelio, *On stress concentration on nearly flat contacts.* The Journal of Strain Analysis for Engineering Design, 2002. **37**(6): p. 493-501.

40. Giannakopoulos, Suresh, and Chenut, *Similarities of stress concentrations in contact at round punches and fatigue at notches: implications to fretting fatigue crack initiation.* Fatigue & Fracture of Engineering Materials & Structures, 2000. **23**(7): p. 561-571.

41. Sackfield, A., D. Dini, and D.A. Hills, *The finite and semi-infinite tilted, flat but rounded punch.* International Journal of Solids and Structures, 2005. **42**(18): p. 4988-5009.

42. Johnson, K.L. and K.L. Johnson, *Contact Mechanics*. 1987: Cambridge University Press.

43. Ciavarella, M. and P. Decuzzi, *The state of stress induced by the plane frictionless cylindrical contact. I. The case of elastic similarity.* International Journal of Solids and Structures, 2001. **38**(26–27): p. 4507-4523.

44. Persson, A., *On the Stress Distribution of Cylindrical Elastic Bodies in Contact*. 1964: inst.

45. Dundurs, J., K.C. Tsai, and L.M. Keer, *Contact between elastic bodies with wavy surfaces.* Journal of Elasticity, 1973. **3**(2): p. 109-115.

46. Goryacheva, I.G. and R.M. Martynyak, *Contact problems for textured surfaces involving frictional effects.* Proceedings of the Institution of Mechanical Engineers, Part J: Journal of Engineering Tribology, 2014. **228**(7): p. 707-716.

47. Kuznetsov, E.A., *Periodic contact problem for half-plane allowing for forces of friction.* Soviet Applied Mechanics, 1976. **12**(10): p. 1014-1019.

48. Evans, A.G., *Perspective on the development of high-toughness ceramics.* Journal of the American Ceramic Society, 1990. **73**(2): p. 187-206.

Link between chapter 4 and chapter 5

In the previous chapter, we developed analytical and finite element models using linear elasticity and non-Hertzian contact mechanics, which were used to explore the effect of geometry and friction coefficient f, on the pullout response and maximum stress in interlocking sutures. The geometrical parameters explore are interlocking angle θ_0, radius of curvature R_0/R_1, and plateau length d/R_0. The results from the models show that the mechanical properties of interlocking sutures can be tuned with these geometrical parameters. The maximum stress in the sutures increases with increase in any of the design variables which might lead to premature fracture of the tabs, therefore we performed an exhaustive search optimization. The optimization results show that the best mechanical properties are achieved with low friction coefficient f, and high interlocking angle θ_0 and the most potent suture geometry is the multilocking sutures where locking is along the pulling direction. This model provides guidelines for the design, optimization and fabrication of interlocking sutures pulled in tension with no adhesive at the interface. The next chapter is an article which was recently published in the *International Journal of Solids and Structures* 97–98 p389–399 (2016). In this chapter, we used laser engraving technique to explore the effect of geometry on mechanical performance of aluminium oxide. We engraved surface trenches on thin plate of aluminium oxide in order to guide cracks into different suture configurations. The experiments show that the fracture toughness of the aluminium oxide can be improved if the cracks are deflected into transverse or sinusoidal interfaces but with no stable crack propagation. In addition we engraved jigsaw-like interlocking interfaces that showed better mechanical response when tested in fracture. The mechanical response can be modified by tuning the interlocking angle θ_0, for the jigsaw-like sutures, the amplitude-wavelength ratio

A/λ, for the sinusoidal sutures. It was concluded that the jigsaw-like interfaces dissipate the most energy which depends on the interlocking angle θ_0, and friction at the interface.

Chapter 5

Toughening of thin ceramic plates using bioinspired surface patterns

Chapter 5: Toughening of thin ceramic plates using bioinspired surface patterns

Idris A. Malik and Francois Barthelat*

Department of Mechanical Engineering, McGill University, 817 Sherbrooke Street West, Montreal, QC H3A 2K6, Canada

*francois.barthelat@mcgill.ca

International Journal of solids and structures, Volumes 97–98, 15 October 2016, Pages 389–399

http://dx.doi.org/10.1016/j.ijsolstr.2016.07.010

5.1. Abstract

High-performance natural materials such as bone, teeth or mollusk shells contain a large volume fraction of minerals to generate stiffness and hardness. They are also packed with weak interfaces, which generate nonlinear deformations and channel cracks into powerful toughening configurations. As a result, these natural materials achieve simultaneous stiffness, hardness and toughness, which are properties which are mutually exclusive in engineering materials. Following these concepts, we have engraved trenches with controlled patterns and depth in thin plates of aluminum oxide. The trenches can guide propagating cracks, which we use to implement toughening mechanisms and unusual deformation mechanisms. We present fracture results on samples with transverse interfaces and sinusoidal interfaces. We also explore interlocking-jigsaw like interfaces, which dissipate the most energy and produce the highest toughness. These interfaces also profoundly change the way the material deform in tension, by introducing controlled non-linear deformations accompanied with geometric hardening and frictional pullout, in an otherwise all-brittle material.

***Keywords**: Bio-inspiration, Sutured materials, Fracture toughness, Ceramics, Laser engraving, Crack deflection.*

5.2. Introduction

Improving the properties of traditional engineering materials is an ongoing challenge. An interesting and promising source of inspiration is nature, which provides many examples of materials with unusual and attractive properties. For example bone, teeth or mollusk shells are hard biological materials which must prevent catastrophic fracture from fatigue, overloading or impacts. While these materials are weaker than our best engineering composite materials, they are much stronger and tougher than their base components, boasting amplifications of properties which are unmatched in manmade materials. In these materials, relatively high contents of minerals generate the stiffness, strength and hardness which are required for their function. Considering the high content of brittle minerals of these materials, they are also remarkably tough and they can therefore combine high stiffness, strength and toughness, properties which are mutually exclusive in traditional engineering materials [1]. As a universal strategy in these materials, the propagation of cracks is managed and prevented by the many weak interfaces they contain [2-5]. For example, cracks are deflected and twisted by the weak cement lines in cortical bone, which is a major toughening mechanism in this material [6, 7]. In teeth, cracks propagating along the proteinaceous sheaths between the mineral enamel rods are channeled towards region where propagation is more difficult (Figure 5.1a, [8]). In nacre, the massive inelastic deformations of interfaces in a process zone around cracks dissipate large amounts of energy, which is the main toughening mechanisms in this material (Figure 5.1b, [9]). Mechanisms of crack deflection or deformation at the interfaces are governed by friction, unfolding of proteins, hydrogen bonds or electrostatic interactions at the molecular scale [5]. In turn, the architectures of the interfaces amplify their local response to generate inelastic deformation and fracture

mechanisms at larger length scales, ultimately leading to unusual and attractive combinations of stiffness, strength and toughness. The morphology of the interfaces has a strong influence on their mechanical response. For example cement lines in bone, sheaths in tooth enamel and interfaces in nacre are wavy, which increases the resistance to sliding and pullout [10]. More extreme cases are also found in nature in the form of interlocked suture lines [11] as seen in ammonites [12] (Figure 5.1c), osteoderms of turtle shells [3, 13] (Figure 5.1d), or the linking girdles of diatoms [14].

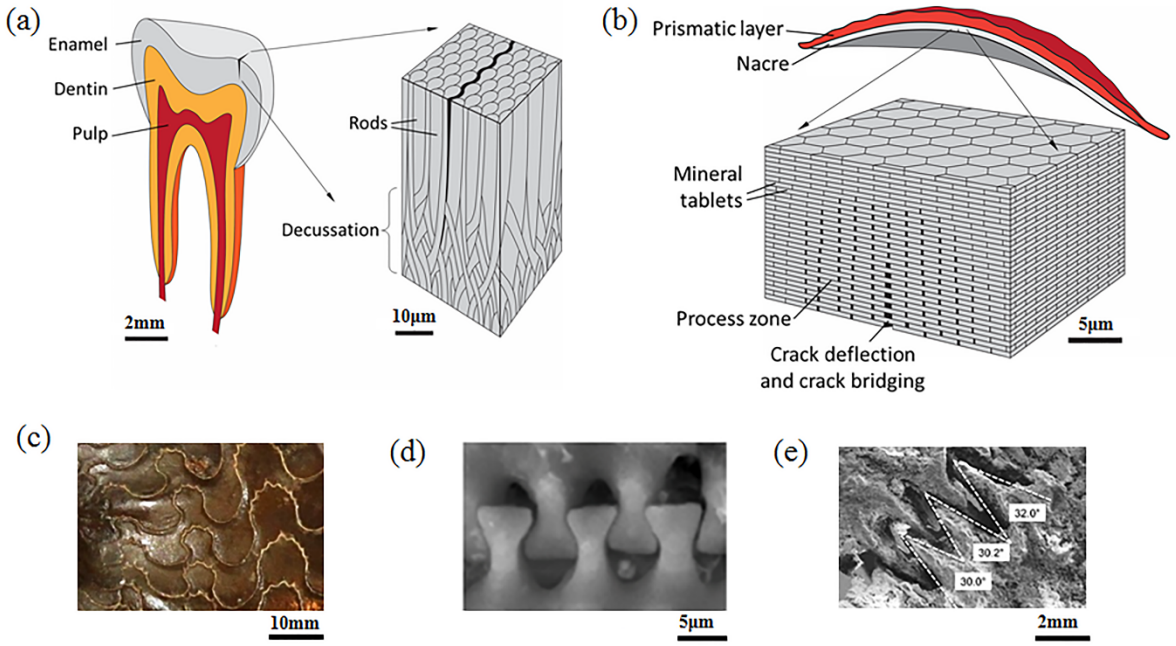

Figure 5.1: Overview of mammalian tooth and micro-architecture of enamel (adapted from [15]); (b) overview of nacre and the toughening mechanisms (adapted from [15]); Other natural system showing sutures: (c) *Ceratitic ammonoid* with intricate suture lines [12], (d) Linking girdles of diatoms (adapted from [14]), and (e) Suture between osteoderms of a leather back sea turtle shell (adapted from[13]).

Hard biological materials may also be interpreted as architectured materials [4], where stiff blocks with precise shapes and arrangement are bonded by weaker and more deformable interfaces [16, 17]. The general concepts associated with this particular type of material are shown in figure 5.2. On a generic force-deformation plot, brittle materials deform linearly and fail at very small deformations (Figure 5.2a). The addition of weak interfaces that can open (in mode I) or slide (in mode II) decreases the strength but increase overall deformation

and energy absorption. Nonlinear deformations can spread over large volumes of material, from geometric hardening [10], from strain hardening or from strain rate hardening at the interfaces [18, 19]. In terms of fracture, a monolithic brittle material has a relatively low toughness which remains constant with crack extension (Figure 5.2b). A material with weak interfaces will channel cracks along these interfaces which require these interfaces to be sufficiently weak compared to the bulk [20-22], with the implication that the initiation toughness is lower than the bulk material. However, with an adequate architecture, the cracks can be channeled into configurations that eventually impede crack propagation, increasing the toughness to levels which are higher than the monolithic material (Figure 5.2b). In this general description, the stiff but brittle material occupies 95-99% of the volume of the material as seen in nacre [10], tooth enamel [23] and other synthetic architectured materials [24].

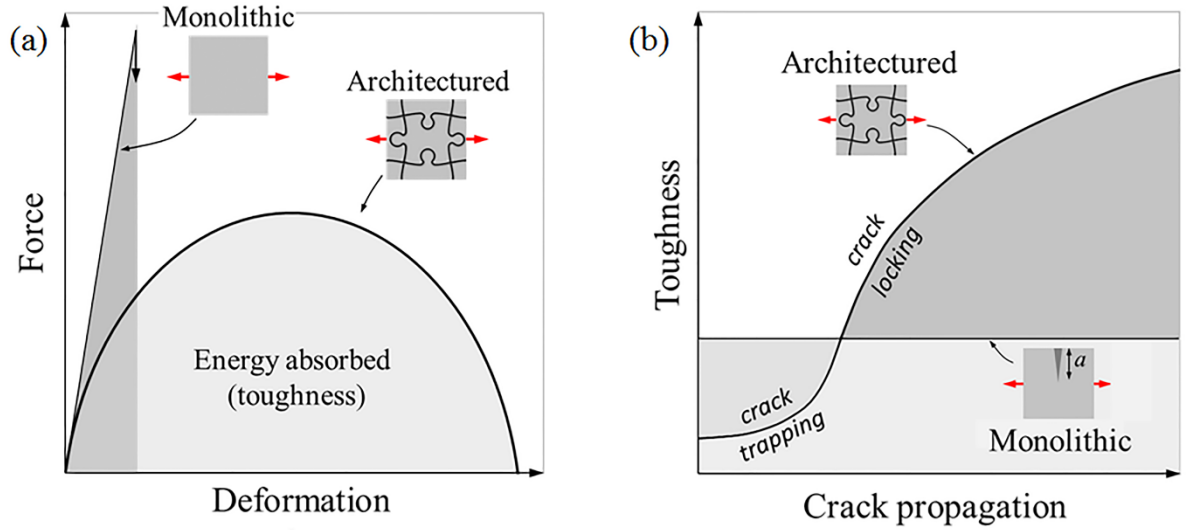

Figure 5.2: General concepts in architectured materials for (a) large deformation and energy absorption, and (b) toughness (adapted from [15]).

The concept of weak interfaces carefully interspersed within materials is already used in engineering materials such as fiber reinforced composites [25] and layered ceramics [26-28]. However, the nature and morphology of the interfaces in these materials are far less sophisticated than what is observed in nature. Recently, we have implemented the idea of

carving weak interfaces within the bulk of transparent glass to increase some of its mechanical properties, with emphasis on toughness and resistance to impacts [15]. Here we use a laser engraving technique to carve a variety of well-controlled patterns of trenches on the surface of thin ceramic plates, providing weak interfaces that interact with incoming cracks, modify overall fracture toughness and in some cases completely transform the way this initially brittle material deforms and fails in tension.

5.3. Sample preparation

The base materials used in this study were 0.63 mm thick plates of nonporous, high-purity alumina (McMaster-Carr, IL, USA). Trenches with controlled patterns and depth were carved on the surface of the alumina using a laser engraver (Vitrolux, Vitro Laser solutions UG, Minden, Germany) to serve as guides for propagating cracks. The system uses a pulsed UV laser (355nm, 500mW cw pumped, 4 kHz repetition rate, 4-5 ns pulse duration) which is focused at a series of predefined points (Figure 5.3a), ablating material from the surface of the ceramic plate to form a continuous trench. The pattern of the trench was created by the computer-controlled tilting of the laser beam with a set of mirrors, and the removal rate for the ceramic was adjusted by tuning the power of the laser and the spacing between the pulsed energy delivered by the laser [29, 30]. The depth of the trench was controlled by the tuning of the removal rate and by the numbers of times the laser engraving was repeated on the same pattern.

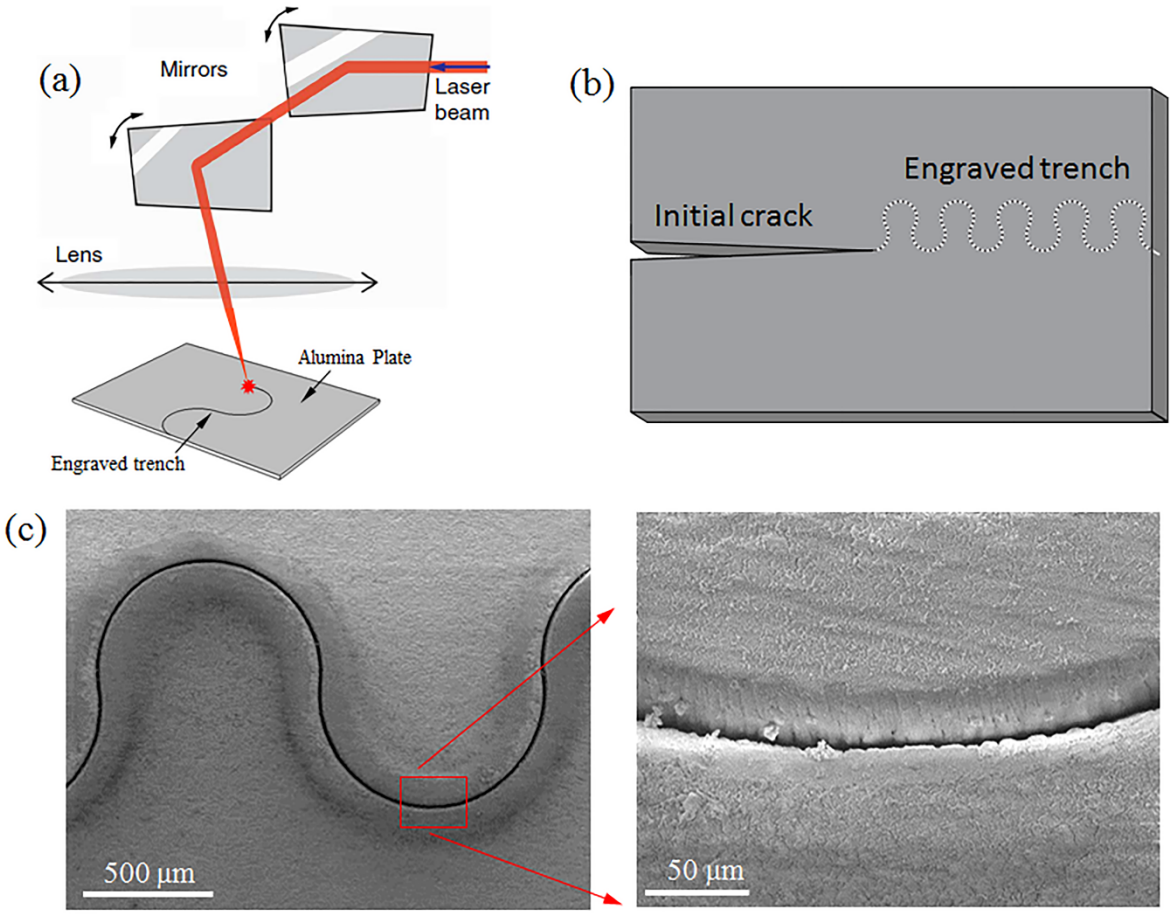

Figure 5.3: (a) A 3D laser engraving set-up (b) a trench engraved ahead of a crack, in the shape of jigsaw line. (c) SEM images of a sample of the engraved alumina, showing the width of the trench

Figure 5.3b and 5.3c show an example of a pattern for the trench, in this case in the shape of an interlocking jigsaw-like suture. The spatial resolution of the pattern is high, the pattern of the trench on the ceramic perfectly matching the geometry of the desired pattern, with a uniform width of about 30 microns (Figure 5.3c). The effects of the trenches on fracture toughness were evaluated using compact tension samples with the dimensions shown in figure 5.4a. The contours of the samples were cut from the plates. A 400-micron deep trench following the contour of the sample was first laser engraved, and a high-powered ultrasonicator with a flat ended probe (Sonics vibra cell, Sonics & Materials Inc., 53 Church Hill, Newtown CT USA) was then pressed directly onto the engraved trench. The probe transmitted high-frequency cyclic stress waves onto the sample, which propagated cracks from the engraved lines where the stresses were higher. This method of controlled fatigue

crack propagation using ultrasonic stress waves is similar to experimental methods developed for the accelerated fatigue testing of materials [31]. With our setup the cyclic stress waves applied to the material propagated fatigue cracks through the thickness, completely cutting the plate in about four minutes. The same method was used to prepare pin holes and the initial notch of the fracture samples.

5.4. Mechanical tests

The compact tension fracture samples and the tensile samples were tested using a miniature loading machine (Ernest F. Fullam Inc., Latham NY USA) at a displacement rate of 2 μms^{-1}.

5.4.1 Tests on the bulk ceramic

The first series of tests was used to measure the toughness of the ceramic plate with no engraved trench. The force-deflection curve for the compact tension test sample was linear up to fracture which, as expected, was brittle. The maximum tensile force was used to compute the toughness of the ceramic using standard methods from linear elastic fracture mechanics with a compact tension configuration [32]. A toughness of $K_{IC}^{(b)}$= 5.04±0.06 MPa.$m^{1/2}$ (N=3 samples) was found for the bulk ceramic, which is consistent with usual values for the toughness of aluminum oxide [33]. This value served as a reference to assess the effect of various engraving patterns on overall toughness. We also measured the modulus and strength of the ceramic using a three-point bending configuration on small beams. We measured a modulus of about 355 GPa and a tensile strength of 365-395 MPa (N=2 samples). The range of strength is approximate and we did not attempt a full characterization of the Weibull statistic for this material.

5.4.2. Fracture toughness of a straight engraved trench

The next series of tests was used to measure the apparent toughness of the engraved trench, and to assess the effect of its depth. We prepared and tested compact tension fracture samples which had exactly the same dimensions as the samples used to measure the toughness of the

bulk ceramic, with the exception that these samples contained a straight engraved trench of controlled depth *s* ahead of the notch (Figure 5.4a). Here and for the rest of this study, we were concerned with the apparent changes in toughness in reference to the bulk material, and we used the same standard methods to compute the fracture toughness of the engraved sample. All the samples discussed in section *5.4.2*, *5.4.3* and *5.4.4* of this article failed in a brittle fashion, and possible local changes of stiffness or inelastic processes due to the engraved patterns were not considered when calculating toughness. We therefore assumed small scale yielding, where the state of stress at the crack tip is governed by a stress intensity factor K_I (the samples presented in section *5.4.5* were analyzed differently). Figure 5.4b shows the fracture toughness $K_{IC}^{(i)}$ of the interface formed by the engraved trench normalized by the fracture toughness of the intact plate $K_{IC}^{(b)}$, and as a function of the normalized depth of the trench *s/t*. The data shows how the effective toughness of the interface can be tuned to any value between the toughness of the bulk (i.e. $K_{IC}^{(i)} / K_{IC}^{(b)} = 1$, no trench), to zero (i.e $K_{IC}^{(i)} / K_{IC}^{(b)} = 0$, through cut) by adjusting the relative depth of the trench *s/t*. The laser engraving method therefore grants the ability to decrease the toughness of pre-defined lines that can deflect and guide propagating cracks within the plate. While the cracks can initially easily propagate along the weakened lines, carefully designed patterns can make crack propagation increasingly difficult. The cracks can therefore become progressively "trapped" as they propagate, which can effectively increase overall toughness by a significant margin.

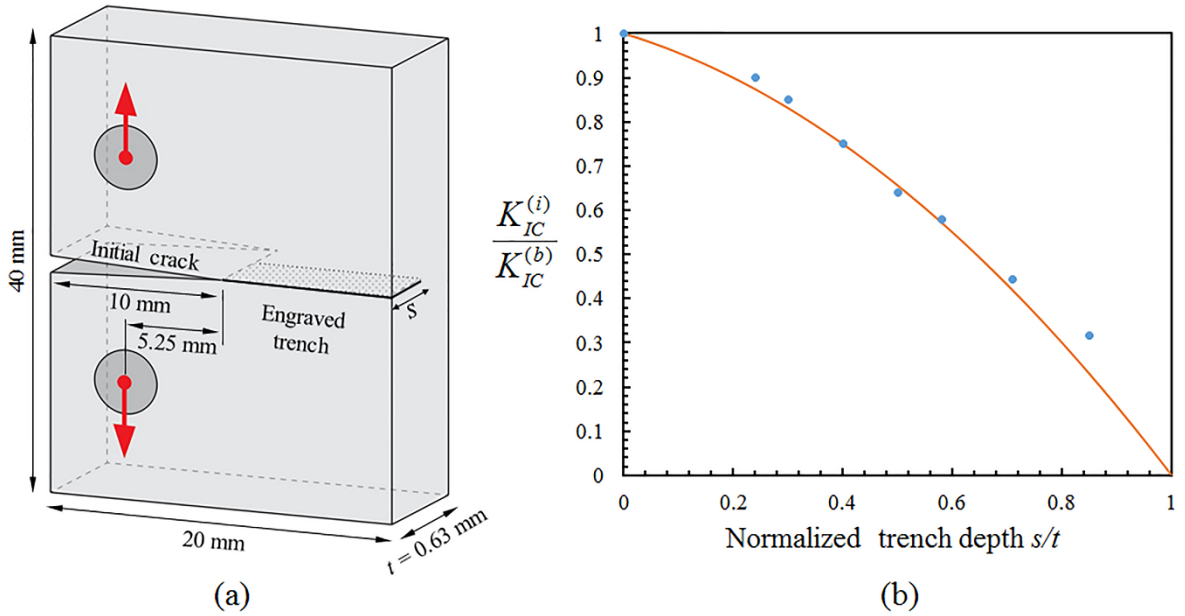

Figure 5.4: (a) Schematic of the compact fracture sample with dimensions. In this case the sample contains a straight engraved trench ahead of the initial crack; (b) Effect of trench depth s (normalized by the plate thickness t) on the fracture toughness of the interface defined by the trench $K_{IC}^{(i)}$, normalized by the fracture toughness of the bulk ceramic $K_{IC}^{(b)}$.

5.4.3. Transverse interfaces

Crack deflection along weak interfaces is a well-known and powerful toughening mechanism for engineering and natural materials, including for ceramics and ceramic-ceramic composites [26-28]. This strategy consists of creating weak interfaces across the expected crack path (which must be known a priori from the loading configuration of the component). The weak interfaces deflect propagating cracks transversely and away from the direction of the main driving force, which result in an overall increase of toughness [20, 26]. In this study, we fabricated compact tension ceramic samples with a series of five straight trenches spaced by a distance d=10 mm and oriented at 90º from the initial notch (Figure 5.5a). The length of the trenches was varied using L_i=12 mm, 18 mm and 22 mm. Preliminary tests showed that shallow trenches could not deflect the main crack. The crack could only be deflected for $s/t > 0.7$, corresponding to a relative interface toughness of $K_{IC}^{(i)} / K_{IC}^{(b)} < 0.45$ from our experimental calibration (Figure 5.4b). A condition for crack deflection into a weak interface

at 90 degree from crack propagation is $G_c^{(i)}/G_c^{(b)} < 1/4$, where $G_c^{(i)}$ and $G_c^{(b)}$ are the critical strain energy release rates for the interface and the bulk of the material, respectively [21]. Setting aside the effects of fracture mode mixity as a coarse approximation, the condition can be written in terms of fracture toughness as $K_{IC}^{(i)}/K_{IC}^{(b)} < 1/2$. Our experimental observations on crack deflection are therefore in good agreement with theoretical predictions. In all cases, fracture of the samples was brittle, with no sign of stable crack propagation (upon fracture the force decreased sharply to zero). The crack followed the entire length of the engraved interface, after which the crack followed a horizontal trajectory parallel to the initial notch (Figure 5.5b). Engraving transverse lines spanning the entire sample resulted in the sample completely splitting in the across direction. The apparent sample toughness was computed from the maximum force and reported on figure 5.5c. This toughness was about 45% higher than the bulk. The length of the engraved lines had no effect on this improvement, suggesting that the toughness improvement occurred upon crack initiation. A likely mechanism is the blunting of the initial crack by the engraved trench, a well-known mechanism described by Cook and Gordon [20].

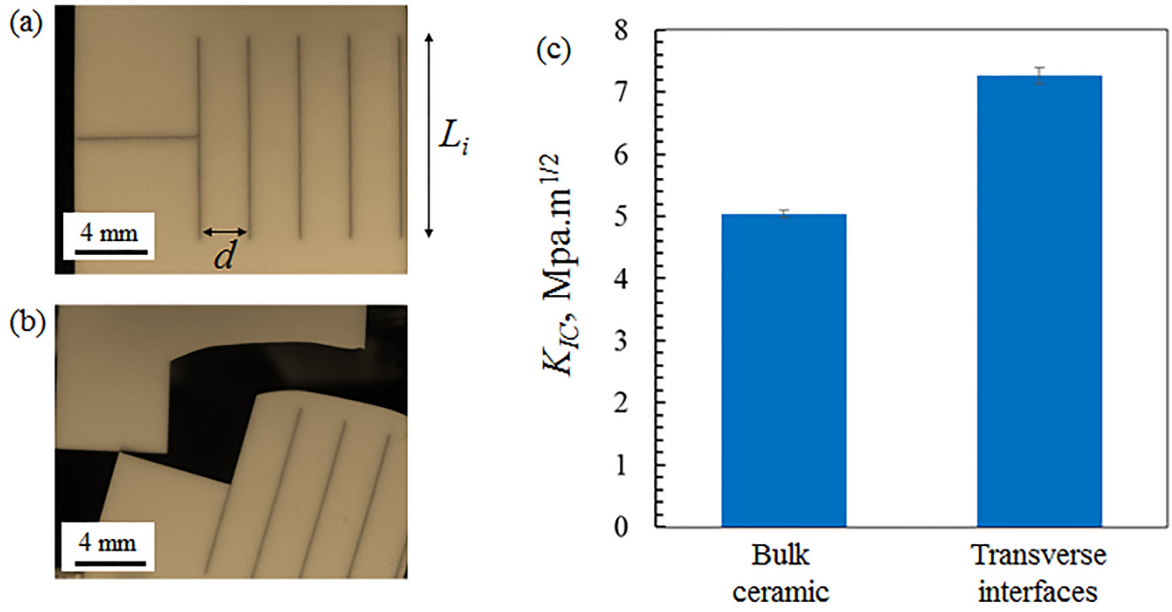

Figure 5.5: Samples showing transverse trenches (a) initial sample (b) sample after testing. (c) Fracture toughness for bulk ceramic and ceramic with transverse interfaces. Data for the transverse interface is independent of d and L_i.

5.4.4. Wavy interfaces

The laser engraving method enables a large variety of patterns which are not necessarily based on straight lines. For example, recent models and experiments have shown that bond lines with a wavy profile can increase toughness [34, 35]. In this study, we investigated sinusoidal interfaces in an all-ceramic system. A trench with a sinusoidal pattern of amplitude A and wavelength λ was engraved ahead of the notch, following the equation [35]:

$$y(x) = A\left(1+\sin\left[2\pi\left(\frac{x}{\lambda}-\frac{1}{4}\right)\right]\right) \qquad (5.1)$$

where x is the distance from the crack tip along the axis of the notch. Figure 5.6a shows the geometry of the sinusoidal interface and its orientation with respect to the notch. The tip of the notch was positioned so the overall width of the suture (defined by the position of amplitude peaks) was centered on the line of the notch. This configuration was tested using a compact tension configuration, with a relative trench depth of s/t =0.75. We examined the effect of A/λ by keeping λ at a constant value (λ =4mm) and by varying A (A=0.5, 1, 2, 4, 8 and 12 mm). The engraved interface was weak enough to guide crack propagation along its

entire length for all the values of A/λ that we tested here. The fracture was brittle, with no evidence of stable crack propagation or even short sequences of stable crack growth as previously reported for sinusoidal bond lines [36]. However, the fracture toughness of the sinusoidal trench increased with increasing amplitude, as shown in figure 5.6c. For $A/\lambda > 1$ the toughness of the interface became even greater than that of the bulk ceramic. When A/λ was increased further the data appeared to converge toward $K_{IC} / K_{IC}^{(b)} \approx 1.45$, which matches the improvement of toughness for transverse interfaces reported in the previous section (figure 5.5c). When $A/\lambda \rightarrow +\infty$, the section of the pattern encountered first by the propagating crack becomes close to a transverse line. As for the transverse interfaces, the mechanism of toughening for the sinusoidal line is also probably governed by crack blunting at the tip. Only the initial angle of the engraved line probably affected the initial fracture toughness measured experimentally. There was no evidence that the sinusoidal interface improved the stability of the crack, the force increasing linearly to a maximum value and then sharply dropping to zero upon crack propagation. Previous studies showed that a small amount of stable crack propagation is possible along wavy interfaces [34, 35]. However crack stability is, in general, function of both the material and the loading configuration (which includes sample geometry). It is likely that the configurations used in these previous studies (larger models, double cantilever beams) were more favorable to crack stability.

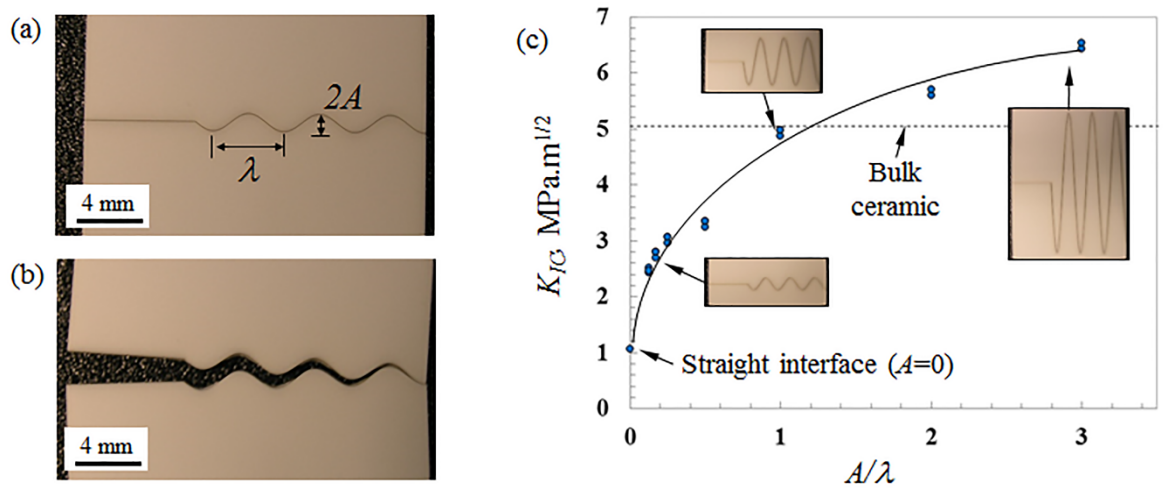

Figure 5.6: Sinusoidal trench: (a) initial geometry showing amplitude and wavelength; (b) fractured sample; (c) Apparent fracture toughness of the interface as a function of the normalized amplitude of the pattern.

5.4.5. Jigsaw-like interlocking features

While the transverse and sinusoidal trenches could improve the fracture toughness of the bulk ceramic to some extent, crack stability was not improved. Here we explore the effect of re-entrant features on the trench line, designed to add stability and to dissipate frictional energy upon pullout (figure 5.7a). This geometry, reminiscent from natural sutures in biological organisms [12], was previously implemented in thin glass slides where interlocking and frictional pullout significantly increased toughness [15]. The geometry was constructed based on arcs of circles with radius R , joined to form a jigsaw-like feature with a locking angle θ_0 (figure 5.7b). Rounded features were used for the geometry in order to minimize stress concentrations in the ceramic. The radius was kept a constant value R = 0.5 mm, and different values of the locking angle were explored. Here we engraved jigsaw-like trenches of relative depth s/t =0.75, and we then sonicated the engraved line in order to ensure that the pullout mechanisms prevailed over fracture of the ceramic. Figure 5.7c show typical pictures of the engraved samples before and after testing. Opening the crack was a progressive and stable process which involved the pullout of the jigsaw-like tabs, with associated interlocking stresses and frictional dissipation. With the proper range of interlocking angles the pullout

mechanism was successful, the system was stable and the force progressively decreased with crack opening. Figure 5.7d shows representative force-displacement curves from the experiments. For angles θ_0 = 8.5° and θ_0 = 9°, the force-deflection curves had a bell shape which is characteristic of tough, energy dissipating materials with stable crack growth. However, for θ_0 = 9.5° and higher, a large number of jigsaw-like tabs broke during the pullout process, and failure was more sudden and brittle-like.

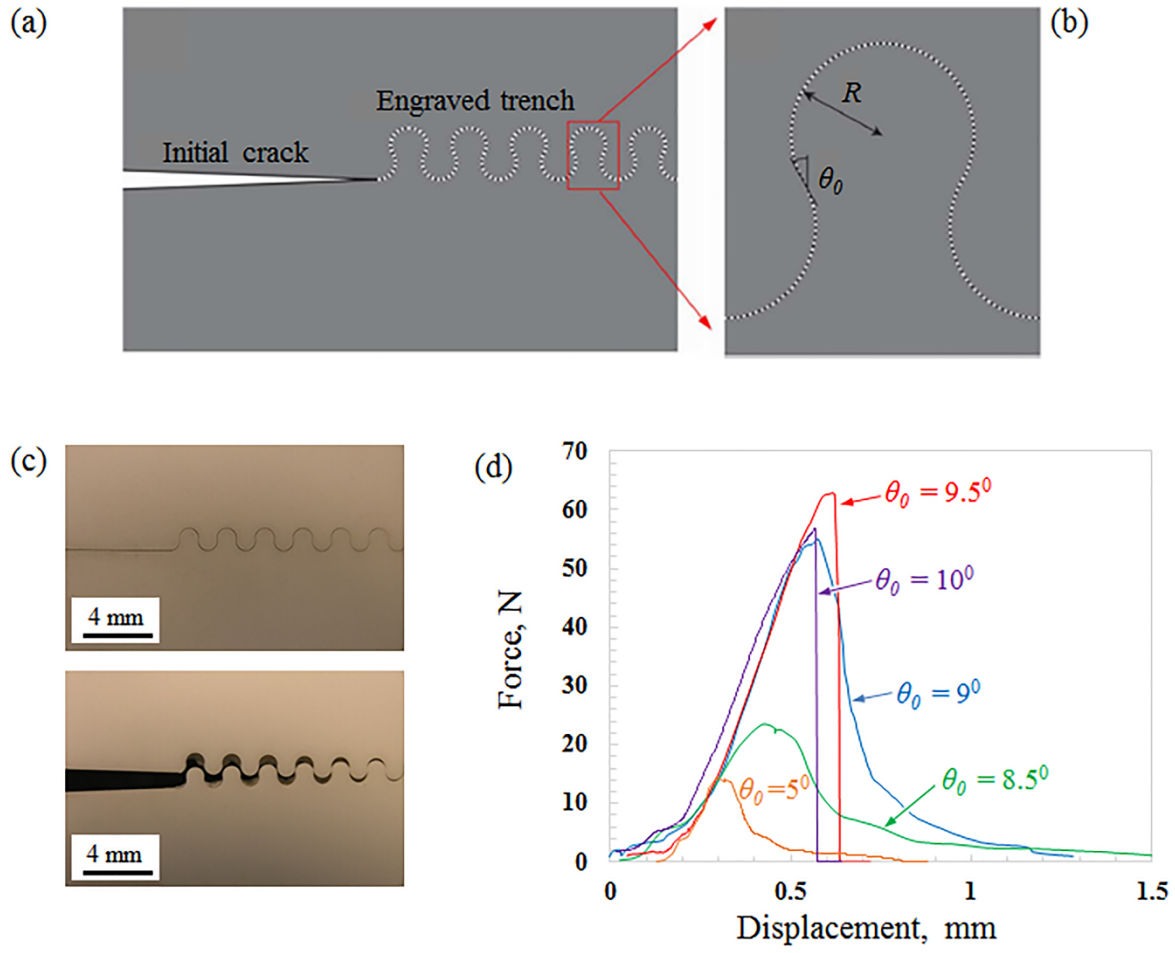

Figure 5.7: Jigsaw-like trench: (a) configuration of the trench with respect to the initial crack; (b) individual jigsaw feature with geometrical parameters; (c) initial and fractured sample; (d) representative force-displacement curves for four locking angles.

The force-displacement curves were analyzed using two approaches. In the first approach, the maximum force was used to compute an apparent fracture toughness K_{IC}, using the same

approach as in the previous sections. For the second approach, we computed J_{IC} as the area under the curve divided by the area of the fracture surface (obtained by multiplying the length of the ligament by the thickness of the sample). This second method is valid only when failure is progressive so that the energy given by the areas under the force-deflection curve corresponds to energy dissipated by the fracture process only. In the cases where failure was brittle, the area under the force-displacement curve includes dynamic effects which do not reflect the toughness of the material [37]. Figure 5.8 gives an overview of the results obtained for different locking angles. For small locking angle $\theta_0 \leq 9.0^0$ the samples failed entirely by the pullout of the tabs, and no damage of the tabs was observed (Figure 5.8a,b). At higher locking angles some of the tabs broke in a brittle fashion, and in increasing numbers as the locking angle increased from 9.5^0 to higher values (Figure 5.8a,b). Figure 5.8c shows the fracture toughness K_{IC} and toughness J_{IC} as function of locking angle. K_{IC} was computed from the maximum force as described above. J_{IC} was computed from the area under the force-deflection curve when the failure progressive. For the brittle cases, we used the standard relation $J_{IC} = K_{IC}^2 / E$ where K_{IC} is the fracture toughness computed from the maximum force on the compact tension specimen and E is the Young's modulus for aluminum oxide (E = 355 GPa measured from experiments). With a Poisson's ratio of ν = 0.2 typical of ceramics, the plane stress and plane strain version of this relation gave estimates for J_{IC} which were only a few percents apart. As the locking angle was increased, the fracture toughness increased to a maximum of K_{IC}=5.18±0.08 MPa.m$^{1/2}$ at a locking angle $\theta_0 = 9.5^0$. At larger locking angles the toughness decreased, probably due to excessive damage in the tabs. Compared to the fracture toughness of the bulk ceramic ($K_{IC}^{(b)}$= 5.04±0.06 MPa.m$^{1/2}$), the gain in fracture toughness from the jigsaw-like pattern is therefore minimal. On the other hand, the gain in toughness in energy terms was significant. J_{IC} progressively increased with

locking angle up to $\theta_0 = 9^0$, at which J_{IC}=3.18 kJ/m^2 which is about 45 times higher than the toughness of the bulk ceramic ($J_{IC}^{(b)}$=0.071 kJ/m^2, computed from $K_{IC}^{(b)}$ and E). Samples with $\theta_0 = 9.5^0$ and higher failed catastrophically, with a sharp decrease in J_{IC} (Figure 5.8). The improvement in toughness generated by the jigsaw-like interfaces is the result of a fine tuning of the locking angle, as shown in figure 5.8. For small locking angles, the interlocking is minimal, frictional resistance is low, and as a result strength and toughness are also low. As the locking angle was increased interlocking increased, which translated in higher cohesive strength and higher toughness. However when the interlocking angle was too high the pullout process was prematurely interrupted by the fracture of the tabs, which resulted in decreased toughness. The optimum mechanical performance of the interface must therefore be finely tuned with the morphology of the suture, which is only possible with a fabrication method with very high spatial fidelity such as laser engraving.

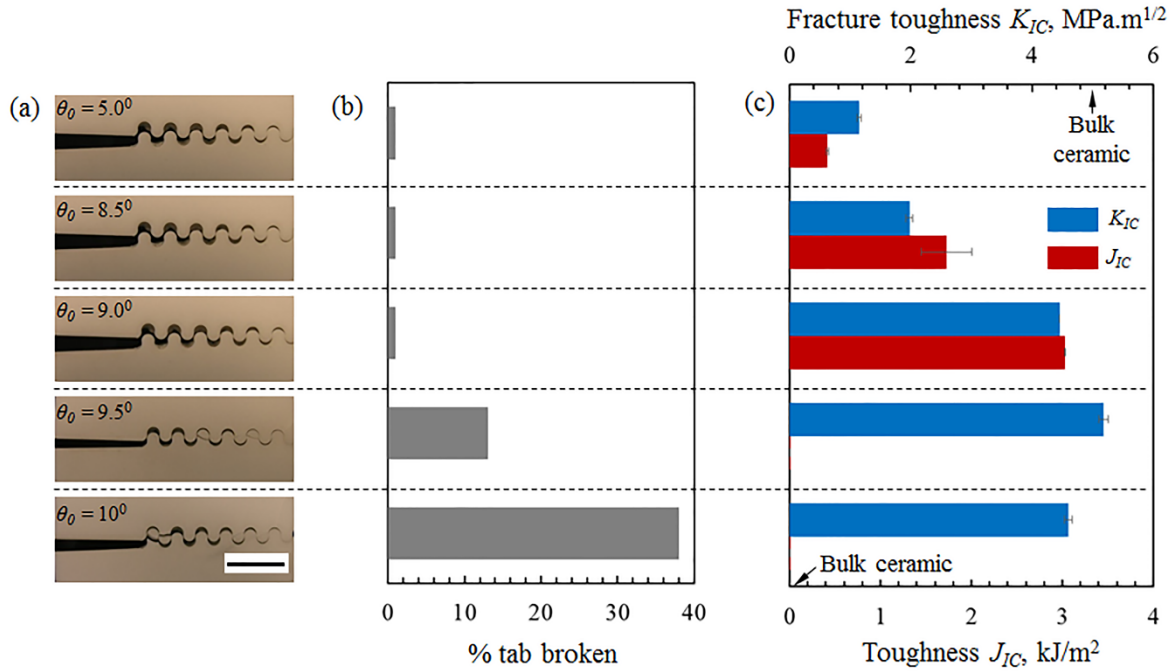

Figure 5.8: (a) Pictures of fractured samples with increasing locking angle θ_0 (scale bar: 4mm), (b) fraction of tabs broken during the test (c) maximum traction and toughness. For the cases θ_0=9.5° and θ_0=10° the fracture of the tab was extensive and J_{IC} was extremely small.

We also evaluated the response of this material under uniaxial tensile loading. Tensile test samples were prepared in a similar fashion as those of the fracture samples, but with three jigsaw-like interfaces (R = 0.5mm, $\theta_0 = 5^0$) spaced by a distance of 3 mm. Figure 5.9b shows the corresponding tensile stress-strain curves. The curves show a low initial modulus characteristic of contact. The system then stiffens, and then progressively soften again as the jigsaw tabs completely pull apart. Remarkably, the geometric hardening associated with progressive interlocking is strong enough to spread non-linear deformations in all three engraved interfaces, although in some instances the edge of the sample broke off because of flexural stress from the pullout mechanism (Figure 5.9a). The tabs of one of the three interfaces eventually completely pulled out and the sample fractured, which was marked by a sharp drop in the force. The strain at failure was in the order of 0.05, which is larger than the strain at failure of the monolithic ceramic by several orders of magnitude. Figure 5.9b also shows that the stiffness and strength of the material increase as the locking angle is increased. Figure 5.9c and 5.9d shows a summary of how these properties vary with locking angle. The modulus increase with locking angle in the range $\theta_0 = 5^0$-9.5^0. The tensile strength increased up to about 40 MPa for $\theta_0 = 9.0^0$, and then decreased for $\theta_0 = 9.5^0$ because of extensive damage to the tabs (Figure 5.9c) resulting in prematurely interrupted pullout. Interestingly the variation of tensile strength measured across the samples we tested (N=3 samples for each angle) was smaller than what is expected from a monolithic ceramic. This observation suggests that because of the failure mode of the architectured ceramic is very different from monolithic ceramics, their strength may not follow the traditional Weibull statistics. The engraving imparted the ceramic with completely different properties. It modulus was in the 2 GPa range (150 times less than the bulk ceramic), it strength in the 20-40 MPa range (depending on locking angle), which is about 10 times lower than the bulk ceramic. However its strain at failure was about 0.05, which is 50 times the strain at failure of bulk ceramic. The

energy stored or absorbed in the material up to failure is also about four times higher in the architectured ceramic compared to the bulk ceramic.

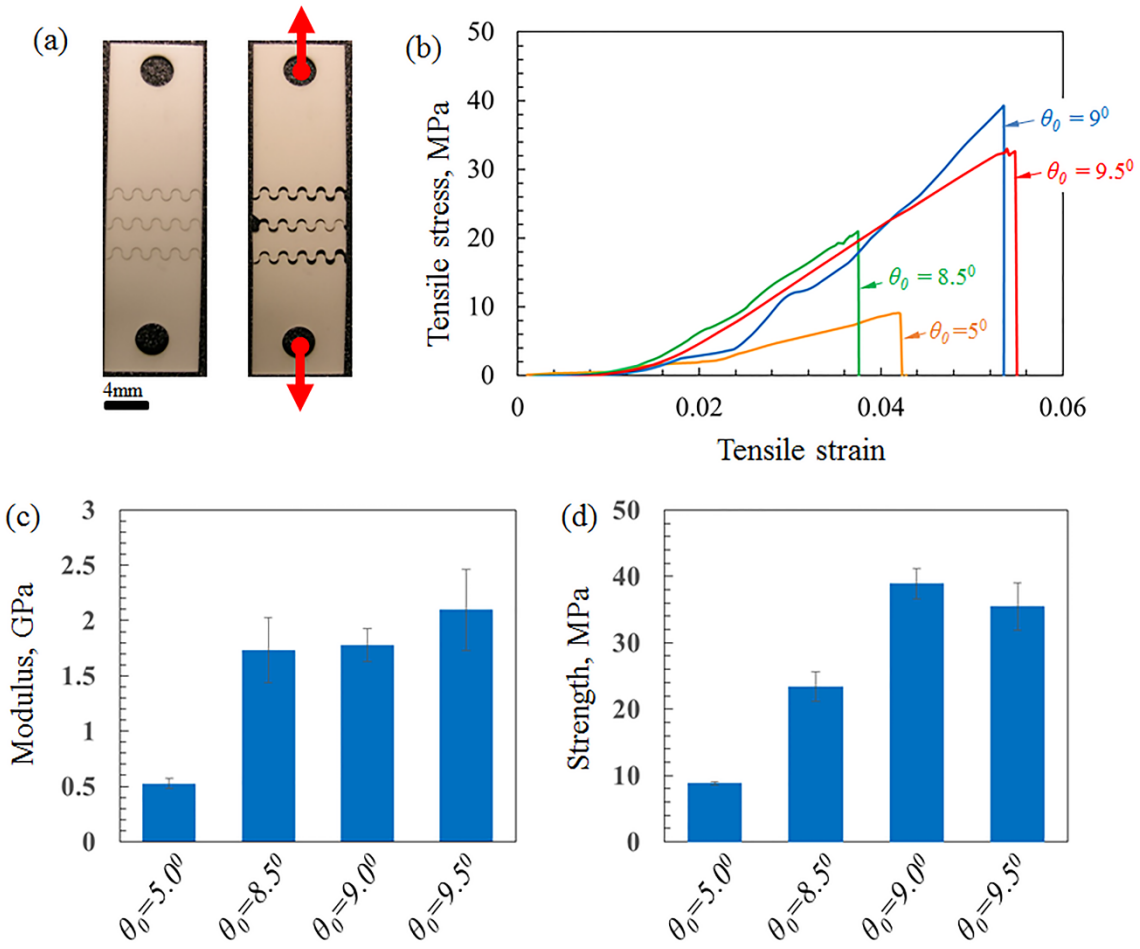

Figure 5.9: (a) samples of tensile sample, before and during the test (b) stress-strain curve from the force-displacement curve of the tensile sample. Bar charts showing the (c) the maximum strength and (d) modulus of the engraved material with respect to the locking angle.

5.5. Summary

High-performance biological materials such as bone, teeth or mollusk shells draw their high stiffness and hardness from high mineral content, and their toughness from their architecture [4, 9]. In particular, these materials contain weak interfaces with specific properties and arrangements which can deflect cracks and channel them into powerful toughening configurations [3-5]. Here we implemented these concepts in thin aluminum oxide plates. We engraved narrow trenches on thin plates of aluminum oxide, in order to guide cracks and to

transform the way the material deforms and fracture. Our experiments show that crack deflection along transverse or sinusoidal interfaces can improve fracture toughness, but without any apparent added crack stability. A more potent geometry was a jigsaw-like suture with interlocking features, which can be adjusted through an interlocking angle. By finely tuning this angle we could make ceramics with high energy absorption capability and large deformability, but at the expense of modulus and strength. Figure 5.10 shows a summary figure of the fracture toughness K_{IC} and toughness J_{IC} normalized by the properties of the bulk ceramic. The materials with the highest fracture toughness K_{IC} are not necessarily the materials with the highest toughness J_{IC}, and vice-versa. K_{IC} and J_{IC} are two measures of resistance to crack propagation that have different meanings. K_{IC} characterizes the resistance to crack propagation in terms of applied force, while J_{IC} characterizes the resistance to crack propagation in energy terms. In terms of applications and design, a material with a high K_{IC} will be able to resist crack propagation under a static load, while a material with a high J_{IC} will be able to resist crack propagation when subject to high amount of mechanical energy, as in the case of impact.

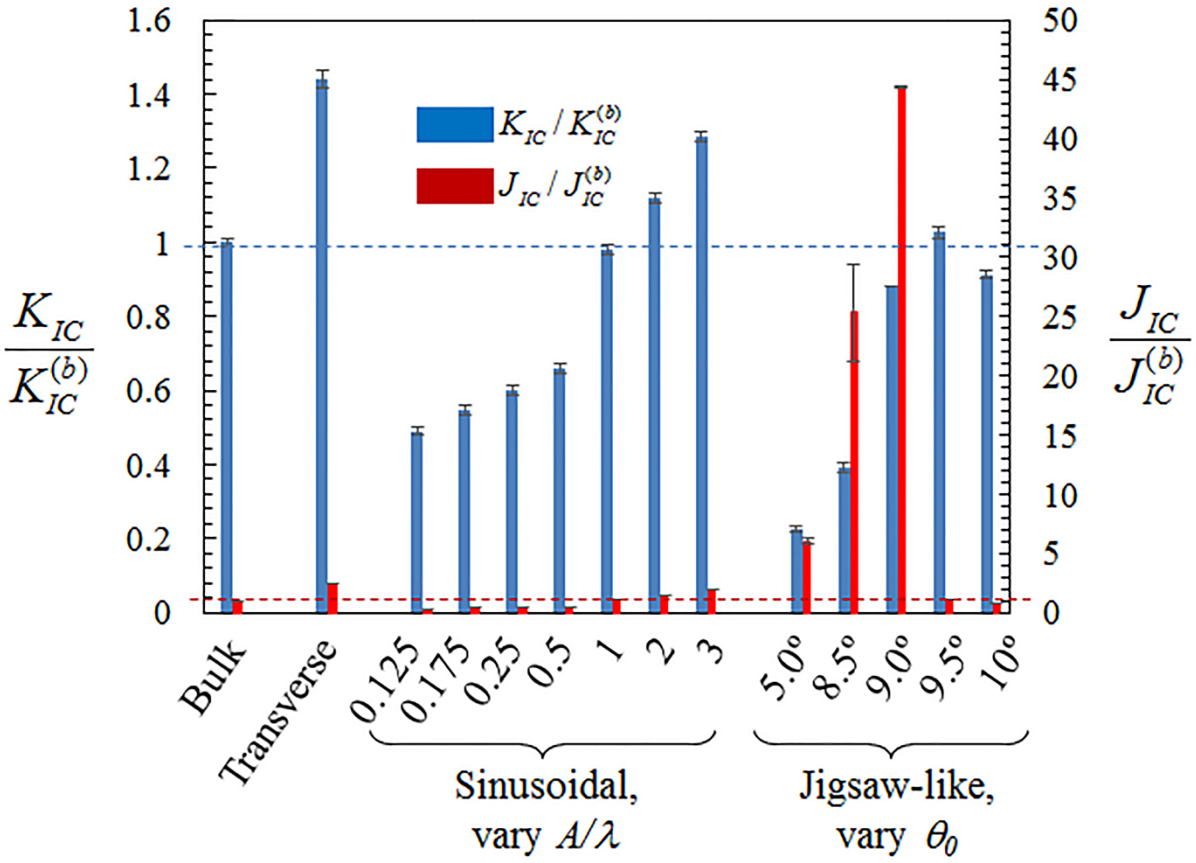

Figure 5.10: Summary of the fracture toughness K_{IC} and toughness J_{IC} normalized by the properties of the bulk ceramic for transverse interfaces, sinusoidal interfaces and jigsaw-like interfaces.

This work demonstrates that carefully introduced trenches can completely transform the mechanics and properties of thin ceramic plates. To maximize these properties and mechanisms a tight control over the morphology of the trenches is required, and we show that engraving with a focused laser beam is an ideal tool for this purpose. As opposed to glass where the focused laser is used to carve interfaces within the bulk of the materials [15, 24], the ceramic we present here is opaque so only the surface was engraved. This approach is therefore the most effective on thin ceramic components, which could still have interesting and useful application in coatings for example. It is likely that the laser engraving process has little impact on the hardness, wear resistance and resistance to high temperatures of the base ceramic material we used (although we have not measured these properties in this work). Therefore potential applications include wear resistant or thermal barrier coatings, where

some in-plane deformability of the hard coating could delay debonding from property mismatch with the substrate. In thicker ceramic, components failure often starts from the surface, because of the state of stress (bending, contact) and/or because of surface flaws. A possible extension of the method could examine the effect of engraving trenches on the surface of thick components such as flexural beams on their mechanical properties. The materials we present here show remarkable improvements in toughness, but at the expense of significant decreases in strength. Through further optimization and tuning it may however be possible to achieve higher strength. For example, the interactions between the tabs rely on frictional contact, which generate high stresses locally. The addition of a softer phase at the interface can redistribute stresses across the interfaces in order to prevent the fracture of the solid parts of the material. In turn, this improvement can open access to more extreme designs (for example, higher locking angles), which will translate into more favorable combinations of strength and toughness. Interfaces in hard biological materials are filled with proteins and/or polysaccharides, and some of these soft materials display unique and attractive molecular mechanisms of deformation with translate into added performance at the macroscale [5]. Filling the engraved trench of our ceramics with a second type of softer material could therefore provide additional dissipative mechanisms.

5.6. Acknowledgements

This work was supported by a Discovery Grant from the Natural Sciences and Engineering Research Council of Canada (NSERC). IAM was supported by a Scholarship from the Nigerian Government through the Nigerian Universities commission.

5.7. References

1. Ritchie, R.O., *The conflicts between strength and toughness.* Nat Mater, 2011. **10**(11): p. 817-822.
2. Fratzl, P., I. Burgert, and H.S. Gupta, *On the role of interface polymers for the mechanics of natural polymeric composites.* Physical Chemistry Chemical Physics, 2004. **6**(24): p. 5575-5579.
3. Dunlop, J.W.C., R. Weinkamer, and P. Fratzl, *Artful interfaces within biological materials.* Materials Today, 2011. **14**(3): p. 70-78.
4. Barthelat, F., *Architectured materials in engineering and biology: fabrication, structure, mechanics and performance.* International Materials Reviews, 2015. **60**(8): p. 413-430.
5. Barthelat, F., Z. Yin, and M.J. Buehler, *Structure and mechanics of interfaces in biological materials.* Nature Reviews Materials, 2016. **to appear**.
6. Koester, K.J., J.W. Ager, III, and R.O. Ritchie, *The true toughness of human cortical bone measured with realistically short cracks.* Nature Materials, 2008. **7**(8): p. 672-677.
7. Currey, J.D., *Bones : structure and mechanics*. 2002, Princeton, NJ: Princeton University Press.
8. Bajaj, D., et al., *Fracture Processes and Mechanisms of Crack Growth Resistance in Human Enamel.* Jom, 2010. **62**(7): p. 76-82.
9. Barthelat, F. and R. Rabiei, *Toughness amplification in natural composites.* Journal of the Mechanics and Physics of Solids, 2011. **59**(4): p. 829-840.
10. Barthelat, F., et al., *On the mechanics of mother-of-pearl: A key feature in the material hierarchical structure.* Journal of the Mechanics and Physics of Solids, 2007. **55**(2): p. 225-444.
11. Cohn, M.B., C.J. Kim, and A.P. Pisano. *Self-assembling electrical networks: an application of micromachining technology*. in *Solid-State Sensors and Actuators, 1991. Digest of Technical Papers, TRANSDUCERS '91., 1991 International Conference on*. 1991.
12. Li, Y., C. Ortiz, and M.C. Boyce, *Stiffness and strength of suture joints in nature.* Physical Review E, 2011. **84**(6): p. 062904.
13. Chen, I.H., W. Yang, and M.A. Meyers, *Leatherback sea turtle shell: A tough and flexible biological design.* Acta Biomaterialia, 2015. **28**: p. 2-12.
14. Lin, E., et al., *Tunability and enhancement of mechanical behavior with additively manufactured bio-inspired hierarchical suture interfaces.* Journal of Materials Research, 2014. **29**(17): p. 1867-1875.
15. Mirkhalaf, M., A.K. Dastjerdi, and F. Barthelat, *Overcoming the brittleness of glass through bio-inspiration and micro-architecture.* Nat Commun, 2014. **5**.
16. Dyskin, A.V., et al., *A new concept in design of materials and structures: Assemblies of interlocked tetrahedron-shaped elements.* Scripta Materialia, 2001. **44**(12): p. 2689-2694.
17. Brechet, Y. and J.D. Embury, *Architectured materials: Expanding materials space.* Scripta Materialia, 2013. **68**(1): p. 1-3.
18. Tang, H., F. Barthelat, and H.D. Espinosa, *An Elasto-Viscoplastic Interface Model for Investigating the Constitutive Behavior of Nacre.* Journal of the Mechanics and Physics of Solids, 2007. **in press (available online January 2007)**.
19. Chintapalli, R.K., et al., *Strain rate hardening: A hidden but critical mechanism for biological composites?* Acta Biomaterialia, 2014. **10**(12): p. 5064-5073.

20. Cook, J., et al., *A mechanism for the control of crack propagation in all-brittle systems.* Proceedings of the Royal Society of London A, 1964. **282**(1391): p. 508-520.
21. He, M.Y. and J.W. Hutchinson, *CRACK DEFLECTION AT AN INTERFACE BETWEEN DISSIMILAR ELASTIC-MATERIALS.* International Journal of Solids and Structures, 1989. **25**(9): p. 1053-1067.
22. Parmigiani, J.P. and M.D. Thouless, *The roles of toughness and cohesive strength on crack deflection at interfaces.* Journal of the Mechanics and Physics of Solids, 2006. **54**(2): p. 266-287.
23. Yahyazadehfar, M., et al., *On the mechanics of fatigue and fracture in teeth.* Applied Mechanics Reviews, 2014. **66**(3): p. 1-19.
24. Mirkhalaf, M., J. Tanguay, and F. Barthelat, *Carving 3D architectures within glass: Exploring new strategies to transform the mechanics and performance of materials.* Extreme Mechanics Letters, 2016. **7**: p. 104-113.
25. Evans, A.G., *The mechanical performance of fiber-reinforced ceramic matrix composites.* Materials Science and Engineering A, 1989. **107**(C): p. 227-239.
26. Clegg, W.J., et al., *A simple way to make tough ceramics.* Nature, 1990. **347**(6292): p. 455-457.
27. Kovar, D., M.D. Thouless, and J.W. Halloran, *Crack deflection and propagation in layered silicon nitride boron nitride ceramics.* Journal of the American Ceramic Society, 1998. **81**(4): p. 1004-1012.
28. Livanov, K., et al., *Tough Alumina/Polymer Layered Composites with High Ceramic Content.* Journal of the American Ceramic Society, 2015. **98**(4): p. 1285-1291.
29. Tsai, C.-H. and H.-W. Chen, *Laser cutting of thick ceramic substrates by controlled fracture technique.* Journal of Materials Processing Technology, 2003. **136**(1–3): p. 166-173.
30. Yan, Y., et al., *CO2 laser high-speed crack-free cutting of thick-section alumina based on close-piercing lapping technique.* The International Journal of Advanced Manufacturing Technology, 2013. **64**(9-12): p. 1611-1624.
31. Mayer, H., *Fatigue crack growth and threshold measurements at very high frequencies.* International Materials Reviews, 1999. **44**(1): p. 1-34.
32. ASTM, *standard E399-05: "Standard Test Method for Linear-Elastic Plane-Strain Fracture Toughness KIc of Metallic Materials".* 2005.
33. Lawn, B.R., *Fracture of Brittle Solids*. 2nd Edition ed. Cambridge Solid State Science Series. 1993, New York: Cambridge University Press.
34. Cordisco, F., et al., *On the mechanics of sinusoidal interfaces between dissimilar elastic–plastic solids subject to dominant mode I.* Engineering Fracture Mechanics, 2014. **131**: p. 38-57.
35. Zavattieri, P.D., L.G. Hector Jr, and A.F. Bower, *Cohesive zone simulations of crack growth along a rough interface between two elastic–plastic solids.* Engineering Fracture Mechanics, 2008. **75**(15): p. 4309-4332.
36. Zavattieri, P.D., L.G. Hector, Jr., and A.F. Bower, *Cohesive zone simulations of crack growth along a rough interface between two elastic-plastic solids.* Engineering Fracture Mechanics, 2008. **75**(15): p. 4309-4332.
37. Barinov, S.M., *Work-of-fracture determination for brittle materials.* Journal of Materials Science Letters, 1993. **12**(9): p. 674-676.

Chapter 6

Conclusions

Chapter 6: Conclusions

6.1 Summary of accomplishments

Hard structural biological materials such as mollusk shells, teeth, and bone possess remarkable properties such as high strength and stiffness as well as toughness, drawn from sophisticated interplay of architectures and weak interfaces comprising of soft organic layers. Suture lines found in cephalopods, human skull or turtle shells provide specific examples of how deformable interfaces can generate toughness and damping in otherwise all brittle systems. In these systems the interplay between interface geometry, interface properties and bulk material stiffness and strength is not fully understood. The results reported in this thesis provide some insight into structure-property relationships in sutured materials. The specific contributions of this thesis are listed below:

- In this work we developed, for the first time, a model that captures the complete pullout of jigsaw-like features over long distances, with progressive interlocking and frictional interactions at the interfaces. The model also provides the maximum tensile stress in the solid parts of the tabs, which can be used to predict and prevent the brittle fracture of the tabs. The pullout resistance increases as the interlocking angle and the friction coefficient increase. The maximum tensile stress also increases with interlocking angle and they are generated by frictional tractions at the contact between the tabs, and occur at the edge of the contact area. These stresses are always significantly larger than the tensile stresses occurring in the smallest cross section of the tabs.
- The exploration of different designs revealed that the frictional stresses near the contact area are the most likely to fracture the solid tabs of the suture. To minimize these stresses the friction coefficient should be reduced. This leads to an unexpected

and useful guideline: to maximize the strength and energy absorption of the suture, its coefficient of friction should be kept to a minimum.

- The pullout models were validated using 3D printed Acrylonitrile Butadiene Styrene (ABS), and miniaturized mechanical testing. We found good agreements between the predicted curves and experimental pullout curves for different interlocking angles. The models also predicted the failure of tabs with good accuracy, in terms of both the interlocking angle at which the tabs start to break and the location of the failure (trailing edge of the contact). In other to validate the effect of low friction and high interlocking angle as predicted by the models, we lubricating the interfaces which reduced the friction coefficient and then increased interlocking angles, which led to higher overall properties. These models and optimization results therefore provide a robust platform for the design and optimization of jigsaw-like sutures, which can be exploited in compliant interfaces, in morphologically enhanced bond lines, and in damping and shock absorbing applications.
- Sutures in nature are more complicated than a single locking site suture. In this work we used a morphometric method to capture the contour of sutures by using the cumulative angular function $\phi(s)$ as a function of curvilinear position s. This method can capture simple and relatively complex profiles using only a few geometrical parameters. The method was used to capture single jigsaw-like sutures and later enriched with additional geometrical features to capture more complex geometries like dovetail, double and multiple locking sites geometries. For each case, closed form solutions are developed to capture the full nonlinear pullout response and to predict the maximum stress (and potential fracture) in the solid material, which are in close agreement with the finite element models.

- The pullout force and the maximum stress have positive correlation with the geometrical parameters which could be detrimental to the suture tabs, therefore an exhaustive search optimization was carried out on each type of design, where every combination of geometrical parameters is examined. We could then identify the optimum parameters for pullout strength and/or energy absorption. The best geometry proved to be the multi-locking tab with N=5 (using a limit strength for the solid of $\frac{\sigma_S}{E} = \frac{1}{100}$, which is typical of engineering materials). Overall the limiting factor for optimization is the maximum frictional stress, and the results show that it is very advantageous to add more contact points to decrease that stress. For the same reason, it is also preferable to use very low coefficients of friction. These models can serve as guidelines to design and optimization of non-adhesive sutures with arbitrary shapes from multilinear signatures.
- We demonstrated that sutures can be fabricated in thin aluminum oxide plates using a laser engraving technique. We engraved narrow trenches on thin plates of aluminum oxide with controlled patterns and depth, which we show can guide cracks and transform the way the material deforms and fracture. The experiments were performed for three different geometry of interfaces and the results show that crack deflection along transverse or sinusoidal interfaces can improve fracture toughness, but with no added crack stability.
- A better geometry was the jigsaw-like suture with interlocking features, which can be adjusted through the interlocking angle. High energy absorption and large deformability can be gotten by finely tuning this interlocking angle but at the expense of modulus and strength. We engraved sutures of different interlocking angle and they were all tested and the results were compared to a bulk ceramic with trench. The gain in toughness in energy terms was significant. To maximize these properties and

mechanisms a tight control over the morphology of the trenches is required, and we show that engraving with a focused laser beam is an ideal tool for this purpose. Interfaces in hard biological materials are filled with proteins and/or polysaccharides, and some of these soft materials display unique and attractive molecular mechanisms of deformation with translate into added performance at the macroscale. As a result, filling the engraved trench of our ceramics with a second type of softer material could therefore provide additional dissipative mechanisms.

6.2 Thesis contribution

The following list summarizes the main findings achieved in this study:

- Using a morphometric method to capture the shape of suture based on some defined shape descriptors like cumulative angular function ϕ_0, plateau length d/R_0, and radii ratio R_0/R_1.
- Analytical models based on simple kinematics, elasticity, and contact mechanics were developed to accurately predict the entire pullout response and the stresses of the sutured materials.
- Finite element models were also developed to validate the necessary assumptions made in the analytical models. A good agreement was found between the analytical and finite element models for all the suture studied.
- Brute force optimization was used to explore the mechanical performance of single locking, dovetail geometries, double and multiple site geometries.
- Sutured materials from brittle materials like Alumina ceramics and Acrylonitrile butadiene styrene (ABS) were fabricated using laser engraving and 3D printing and the materials were mechanically tested to show the pullout response of sutured materials.

6.3 Future work

During the course of this study, the main structural features of sutured materials were identified, explored and implemented into ceramics and ABS, through laser engraving and 3D printing. Analytical and finite element models were developed which accurately predict the pullout response and stress in the sutured materials. The analytical solution was then used to exhaustively search for optimum geometries and interfacial properties in order to optimized the mechanical response. The search produced useful combinations of mechanical properties and therefore the need for fabrication of actual sutured materials to validate the accuracy of the models. These methods provide guidelines to properly explore the optimization of sutured materials through combined experimental, analytical, and numerical studies. The following guidelines are therefore proposed as a continuation to this work:

- The morphometric method described in this study, we only focused on multilinear cumulative angular function and produced sutures which are made up of arcs of circles and lines. This technique can be extended to include different types of signatures, for example curvilinear using shape descriptor approach such as descriptors based on spectral analysis.
- The analytical and finite element models can be extended to include the effect of soft adhesive layers in order to fully mimic some types of sutures in nature, also it can be extended for viscoelastic applications.
- Since suture interfaces in nature can have varying thicknesses, exploring the effect of fine tuning the geometry of a three-dimensional suture material on the mechanical behavior might open way to an interesting result.
- The fabrication methods described here possess high level of geometrical fidelity, therefore these fabrication methods can be used to fabricate thicker ceramic, and the effect of thickness on the mechanical response of sutured materials can be examined.

- Potential application would include wear resistant or thermal barrier coatings where in-plane deformability of hard coatings could delay debonding from property mismatch with the substrate, touch screen applications, and in material that needs tailored mechanical response like strength and energy absorption through geometric effect.

6.4 Publications

6.4.1 Refereed journals

- **Malik, I.A.** and F. Barthelat, *Bioinspired sutured materials for strength and toughness: Pullout mechanisms and geometric enrichments.* Submitted for publication to the International Journal of Solids and Structures, 2017.
- **Malik, I.A.**, M. Mirkhalaf, and F. Barthelat, *Bio-inspired "jigsaw"-like interlocking sutures: Modeling, optimization, 3D printing and testing.* Journal of the Mechanics and Physics of Solids, 2017. **102**: p. 224-238.
- **Malik, I.A.** and F. Barthelat, *Toughening of thin ceramic plates using bioinspired surface patterns.* International Journal of Solids and Structures, 2016.

6.4.2 Conference presentation

- **Malik, I.A.** and F.Barthelat, *Design, optimization and fabrication of bio-inspired sutures,* 2nd Annual Mechanical Engineering graduate research showcase 2017, McGill University, Canada.